Preparation, manipulation and detection of single atoms on a chip

Guilhem Dubois

▶ **To cite this version:**

Guilhem Dubois. Preparation, manipulation and detection of single atoms on a chip. Atomic Physics [physics.atom-ph]. Université Pierre et Marie Curie - Paris VI, 2009. English. NNT : . tel-00593875

HAL Id: tel-00593875

https://theses.hal.science/tel-00593875

Submitted on 17 May 2011

HAL is a multi-disciplinary open access archive for the deposit and dissemination of scientific research documents, whether they are published or not. The documents may come from teaching and research institutions in France or abroad, or from public or private research centers.

L'archive ouverte pluridisciplinaire **HAL**, est destinée au dépôt et à la diffusion de documents scientifiques de niveau recherche, publiés ou non, émanant des établissements d'enseignement et de recherche français ou étrangers, des laboratoires publics ou privés.

Préparation, manipulation et détection d'atomes uniques sur une puce à atomes

Guilhem Dubois

Résumé

Les techniques de refroidissement laser ont réalisé des progrès immenses depuis le début des années 80. Affranchis de toutes les incertitudes inhérentes au mouvement thermique, les physiciens sont désormais en mesure de réaliser des dispositifs de mesure toujours plus précis, tels des horloges ou des gravimètres, en s'appuyant sur l'interaction parfaitement contrôlée entre le champ électromagnétique et de simples nuages d'atomes. De plus en plus, l'utilisation d'atomes ou d'ions comme ultime porteurs d'information apparait comme une solution plausible à la réalisation d'ordinateurs quantiques. Dans cette optique, de nombreux efforts sont consentis afin de miniaturiser, de simplifier, et de rendre possible la production en masse de cette technologie permettant de manipuler les atomes avec tant de précision. L'introduction des puces à atomes a permis de réaliser un grand pas dans cette direction, réduisant drastiquement l'encombrement et le coût des expériences de refroidissement d'atomes. Désormais, la réalisation de dispositifs sur puce permettant d'étendre les possibilités de manipulation des atomes piégés est devenue un objectif majeur.

Dans ce travail de thèse, nous avons réalisé le premier détecteur d'atomes uniques piégés sur une puce à atomes, basé sur l'interaction avec un mode de cavité optique dans le régime de couplage fort. La cavité optique est directement intégrée à la puce à atomes. Fonctionnant dans le régime de détection dite "non-destructive", le dispositif de détection permet de préparer de manière déterministe un atome unique piégé dans un piège dipolaire, avec une précision en position submicrométrique, et dans un état interne spécifique. La détection en tant que telle permet de mesurer l'état hyperfin de l'atome, en perturbant son état externe nettement moins qu'un système de détection fonctionnant en espace libre.

Ce nouveau dispositif de préparation et de mesure est utilisé dans une expérience d'effet Zénon quantique, la première à être effectuée avec des atomes neutres individuels. Sous l'effet de la mesure, l'oscillation de Rabi entre les deux sous-niveaux hyperfins $|F = 1\rangle$ et $|F = 2\rangle$ du niveau fondamental de

l'atome de Rubidium 87 est stoppée. L'expérience, effectuée à la fois dans le régime continu et le régime pulsé, permet de montrer l'adéquation entre le flux d'information extraite du système et le flux de photons traversant la cavité optique de détection.

Abstract

In the three last decades, laser cooling techniques made a huge progress, enabling the realization of high precision devices, such as atomic clocks and gravimeters, based on a perfect control of the interaction between light and matter. Single ions or atoms, in a well-controlled motional state, appear as the ultimate carrier of information for a quantum computer. The road to the quantum computer makes necessary the integration and miniaturisation of the technology which allows to manipulate the atoms with such a high precision. The atomchips represent a big step towards this goal, providing a dramatic reduction to the requirements in terms of volume and cost of laser cooling experiments. Current developments of atomchips technology are largely focused on the realization of integrated devices which extend capabilities in terms of atomic manipulation.

In this thesis, we demonstrate the first detector for trapped single atoms, integrated to an atomchip. The detection device is a high finesse Fabry-Perot optical cavity, in the strong coupling regime of cavity QED. The cavity allows to perform a quantum-non-destructive measurement of the atomic hyperfine number, and perturbs the atomic motional state much less than a free space optical detector. We use this measurement device also to prepare a single atom in a well-defined internal state.

Relying on the preparation and measurement of the atomic state with the cavity, we carry out the first Quantum Zeno Effect experiment performed with single, neutral atoms. Under continuous measurement, we show that Rabi oscillations between hyperfine ground states are slowed down and eventually frozen. This experiment clearly proves that the decoherence induced by a cavity-based detector is totally dominated by the leakage of cavity photons, and not the atomic spontaneous emission.

Remerciements

Toute thèse est un travail d'équipe et je tiens ici à remercier toutes les personnes qui y ont contribué.

C'est grace à mon directeur de thèse Jakob Reichel que j'ai eu la chance de faire une thèse en physique quantique. Faire fonctionner une expérience d'atomes froids nécessite une rigueur et un souci constant du détail expérimental, et c'est grace à lui que j'ai pu progressivement maitriser les différents "building blocks" de l'expérience: électronique, systèmes de vide, radiofréquences, lasers, et au final me forger la culture scientifique et technique nécessaire au fonctionnement et à l'amélioration de l'expérience. Malgré son implication dans un grand nombre de projets, il a toujours été présent au laboratoire à se soucier de l'avancement de l'expérience et à suggérer de bonnes idées.

Tilo Steinmetz, Yves Colombe et Felix Linke ont construit la majeure partie de l'expérience en un temps record. J'ai beaucoup appris auprès d'eux, du fonctionnement d'une diode laser stabilisée en fréquence à celui d'une machine à café à percolation stabilisée en température.

Mes collègues Roger Gehr (ca joue?) et Juergen Volz (boulangerie moderne?) ont travaillé en même temps que moi sur l'expérience, et ca a été un grand plaisir pour moi de les connaitre, à un point où on prenait tous nos repas ensemble pendant que l'expérience tournait. Je leur souhaite personnellement beaucoup de succès dans le futur, que cela soit dans la science ou ailleurs.

Je remercie également les services techniques et administratifs du laboratoire, ainsi que les directeurs Franck Laloe et Paul Indelicato.

Et surtout, ma famille et mes amis à Paris et à Marseille qui m'ont permis de garder la tête hors de l'eau et de conserver une vie en dehors du labo!

Notations

Notation	Description
$\mathcal{P}, p$	a simple probability
$\mathcal{P}(n)$	a discrete probability distribution
$\mathcal{P}_{\text{Poiss}}(n;\overline{n})$	the Poisson distribution with mean value $\overline{n}$
$d\mathcal{P}(x)$	a density probability distribution
$\text{Vect}(\|a\rangle, \|b\rangle, \dots)$	the subspace spanned by quantum states $\|a\rangle, \|b\rangle, \dots$
$\mathbb{P}_E$	the orthogonal projector on the subspace E
ω, Ω	(angular) frequency
f	ordinary frequency
Δ_{12}	frequency detuning $\omega_2 - \omega_1$
ω_{ge}	frequency of the $\|g\rangle \to \|e\rangle$ transition
g	atom-cavity coupling rate = half the vacuum-Rabi-splitting
κ	cavity field decay rate
γ	atomic dipole decay rate = half the spontaneous emission rate
η	cavity pumping rate
$n_0 = \eta^2/\kappa^2$	steady-state cavity photon number for resonant pumping

Contents

Introduction

A single atom interacting with a single mode of the light field is arguably one of the simplest quantum systems one can imagine. The light field itself is a quantum object, however it can be accurately described by a classical wave as long as it does not interact with matter. On the counterpart, the atom also possesses a quantum structure of levels, but only the interaction with other systems, like the modes of the light field, can reveal it. The interaction of the atom with each mode of the light field consists of elementary processes of absorption and emission. These processes are coherent, in the sense that if the atom is initially promoted to an excited state, the available energy will oscillate between the atom to the light field, back and forth. If the atom interacts with several light modes at the same time, the coherence is blurred and the atom eventually loses all its energy to the light field. A possible solution to overcome this problem is to place the atom in a cavity (or optical resonator), which changes locally the structure of the light field. This resonator defines a confined mode of the light field, which interacts much stronger with the atom. This single atom-single mode interaction is described in the framework of cavity quantum electrodynamics (cavity QED). If the resonator quality is not very high, the first consequence is that the atomic decay rate is enhanced by the interaction with the short-lived cavity mode : this is the so called Purcell effect, discovered in 1946 by E.M. Purcell [1]. The observation of the coherent interaction between the atom and the field is only possible with a sufficiently large resonator quality factor, obtained with high reflectivity mirrors. This defines the regime of strong coupling, where the coherent energy exchange takes place at a rate faster than any decay rate of the system. This regime was first obtained in the 80's with single Rydberg atoms interacting with a microwave cavity [2, 3, 4], before it was observed in the optical domain [5]. This conceptually simple system turned out to be an experimental challenge.

From the optical point of view, the presence of a strongly coupled atom changes the transmission spectrum of the weakly probed cavity, splitting the resonance peak in two separate peaks. This effect is called Vacuum

Rabi Splitting, since it is due to the interaction of a single photon. In the optical domain, it was first observed with atomic beams [5, 6]. The cavity transmission can be used as a detection signal for single atoms, or to measure their internal state. In the strong coupling regime, the transmission almost drops to zero at resonance when a resonant atom is in the cavity mode, while a non-resonant atom has no effect on the transmission. Therefore, it is possible with a cavity to obtain a detection signal, without inducing a large backaction on the atomic motional and internal states.

Current research in cavity QED is largely devoted to applications to quantum information. Used with or without a cavity, the single atom is a good carrier of information. The quantum bit (qubit) can be stored in the hyperfine state, with a long coherence time. The cavity can be used as a coherent coupler of the atomic state to the external field [7], which allows to carry the information over long distances. A typical application is the generation of single photons, by promoting the atom to the excited state using a so-called π-pulse, and then waiting for the photon to escape from the cavity mode [8, 9]. With some refinements, one can generate polarisation-entangled pairs of photons [10]. Some proposals exist to couple two qubits in the cavity, using the cavity field to create a switchable interaction, and realize two-qubits gates [11, 12, 13]. The ingredients required for these applications are generally always the same: a strong *and* well-defined coupling between the atom(s) and the cavity. Experimentally, it is difficult to have both : a strong coupling requires a small cavity mode, which increases the requirement on the atomic localisation to obtain a well-defined coupling. Therefore, modern cavity QED experiments rely on the controlled insertion of single atoms into the cavity mode, using e.g. optical conveyor belts [14] or magnetic traps [15]. The control over the quantum state of the atom is then determined by the average kinetic energy of the atom in the trap. A perfect control would therefore be obtained by preparing the atom in the vibrational ground state of the trap. Two strategies are possible at that point: either loading the atom directly in the ground state, or load a hot atom and then cool it down to the ground state, using cooling mechanisms such as cavity cooling [16] or Raman sideband cooling [17]. Until now, only the second strategy was pursued, and lead to important breakthroughs but could not reach the 3D ground state yet. In this work, we will investigate the first strategy, and rely on the cavity detection which induces a minimum perturbation to prepare single atoms in a low energy state.

An intracavity dipole trap is generally used to provide a confinement of the atom in the region of the strongest coupling. This trap defines a lattice

of possible trapping sites, distant by half a wavelength of the dipole trap light. Each site has a slightly different coupling to the resonant cavity mode. Ultimately, the accuracy of a coupling strength is therefore limited by the uncertainty concerning in which site the single atom is loaded. Starting with a magnetic trap with a strong confinement, it is possible to load a specific site of the dipole trap to ensure a well-defined coupling to the mode [15]. This strong magnetic confinement is provided by the technology of atom-chips, which has also made the manipulation of cold atoms much simpler. Atomchips can be used for Bose-Einstein condensation [18, 19], atomic interferometers [20, 21] and clocks [22], coupling to nanoresonators [23]. In the present work, we extend this already broad range of capabilities to the preparation, manipulation and detection of single atoms, paving the way for quantum information experiments with atomchips. Using an optical cavity directly integrated to the atomchip, we demonstrate the first single atom detector for atomchip experiments. This detector is able to perform a non-destructive detection of the single atom hyperfine state, and can be used to prepare it in a well-defined internal state.

Outline of the thesis

The first chapter will be devoted to the theory of cavity QED. After a review of the basic Jaynes and Cummings model, we will analyse the cavity as a detection device and investigate the limitations of the minimum-perturbation measurement picture. The second chapter is a description of the experimental apparatus. The third chapter presents an experiment of detection of waveguided atoms and demonstrates a first signal of single atom detection, but also shows the limitations of waveguided atoms for cavity QED. In the fourth chapter, we turn to fully trapped atoms, and show that we can prepare trapped single atoms and measure their internal state accurately with a minimal perturbation of the motional state. In the fifth chapter, we apply our preparation and detection schemes to measure a Quantum Zeno Effect with a single atom.

Chapter 1

Theory

This chapter is devoted to a theoretical description of the atom-cavity system. After a short introduction to the basic models of cavity QED (sections 1 and 2), we will focus on how a cavity QED setup can be used to detect single atoms (section 3). We will always keep in mind that we want to achieve an efficient detection of single atoms, while perturbing their internal and motional state as little as possible. Therefore, and always considering our experimental situation, we will estimate the effects of a continuous cavity detection on the atomic motional state, characterized by a heating rate (section 4) and on the internal state, characterized by a set of depumping rates (section 5).

1.1 Cavity QED: a strongly coupled quantum system

1.1.1 Enhancing light-matter interaction with a cavity

The interaction between light and neutral matter is generally dominated by the coupling of the electric dipole with the electric field. The interaction energy is then given by the scalar product $-\mathbf{d}\cdot\mathbf{E}$. For atoms, the electric dipole vanishes in the absence of electric fields. When an external electric field is applied, it grows linearly with the field amplitude: $\mathbf{d} = \alpha\mathbf{E}$. The polarisability constant α is characteristic of the atomic species, and accounts for basic optical phenomena such as refraction, absorption, etc. For dilute, homogenous atomic gases, the polarisability is found to be strongly dependent on light frequency ω. In particular, dilute gases are particularly efficient for absorbing light for a discrete set of frequencies (or *lines*), but they are quasi-transparent to other frequencies. Lorentz developed a phenomeno-

logical model which treats the atom as a damped harmonic oscillator, and accounts for the sharp, Lorentz-shaped resonances that we can observe today with high precision laser spectroscopy experiments. However, the major breakthrough came from quantum mechanics theory, which attributes these resonances to transitions between different levels of the discrete energy structure of atoms. This theory is far more satisfactory as it predicts not only the discreteness of the spectrum, but also the position of the lines. The classical atomic dipole has to be replaced by a quantum operator

$$\hat{\mathbf{d}} = \sum_{a,b} \mathbf{d}_{ab} |a\rangle\langle b| \tag{1.1}$$

which connects the different discrete levels $|a\rangle$, $|b\rangle$, etc. The transition from state $|a\rangle$ to state $|b\rangle$, with $E_b > E_a$ comes with the absorption of a photon of frequency $\omega_{ab} = (E_b - E_a)/\hbar$ from the electromagnetic field, while the inverse process corresponds to the emission of such a photon. A theory of quantum electrodynamics (QED) is then required to account for light graininess, and complete the transformation of the classical interaction $-\mathbf{d}.\mathbf{E}$ into a fully quantised Hamiltonian. The process of electromagnetic field quantisation is described in large details in quantum mechanics textbooks, so we just remind here that the electric field has to be decomposed into solutions of Maxwell equations in the form $\mathbf{E}_0^{(l)}(\mathbf{r}) \exp(-i\omega t)$ before being quantised as

$$\hat{\mathbf{E}}(\mathbf{r}) = \sum_l \mathbf{E}_0^{(l)}(\mathbf{r}) \hat{a}_l + \text{ h.c.}. \tag{1.2}$$

By enforcing the electromagnetic energy to be $\hat{H} = \frac{1}{2}\varepsilon_0 \int \mathbf{E}^2 + c^2\mathbf{B}^2 d^3\mathbf{r} = \sum_l \hbar\omega_l \hat{a_l}^\dagger \hat{a}_l$, together with the bosonic commutation relations $[\hat{a_k}, \hat{a_l}^\dagger] = \delta_{kl}$, we find the normalisation condition:

$$\int \mathbf{E}_0^{*(k)}(\mathbf{r}).\mathbf{E}_0^{(l)}(\mathbf{r})\, d^3\mathbf{r} = \frac{\hbar\omega_l}{2\varepsilon_0}\delta_{kl}. \tag{1.3}$$

If we define the mode volume V_m by the equation $\int |\mathbf{E}_0^{(l)}(\mathbf{r})|^2\, d^3\mathbf{r} = V_m |\mathbf{E}_0^{(l)}|^2_{max}$, the maximum field amplitude caused by a single photon in the mode l is given by

$$\mathbf{E}_0^{(l)} = |\mathbf{E}_0^{(l)}|_{max} = \sqrt{\frac{\hbar\omega_l}{2\varepsilon_0 V_m}}. \tag{1.4}$$

The electric field of a single photon in a given mode has therefore a larger amplitude when the mode volume is small. For a stationary mode, this requires to confine the light in a cavity, formed by mirrors which prevent the light from getting out of a well-defined region of space. The cavity has a second effect: it changes the continuous mode distribution into a discrete set of

modes imposed by the boundary conditions. For example, in a Fabry-Perot cavity formed with two concave mirrors, these are the Gaussian modes denoted $\mathrm{TEM}_{n,l,m,p}$, where the triplet $(n,l,m) \in \mathbb{N}^* \times \mathbb{N} \times \mathbb{N}$, and $p = 1, 2$ stands for the polarisation of the light field. The corresponding eigenfrequencies are denoted by $\omega_{n,l,m,p}$. The quantised electromagnetic field can be decomposed as $\hat{\mathbf{E}} = \hat{\mathbf{E}}_{ext} + \hat{\mathbf{E}}_{cav}$, where $\mathbf{E}_{ext}$ include the contributions of free space modes, and $\mathbf{E}_{cav}$ those of cavity modes. The Hamiltonian therefore splits in two components:

$$\hat{H}_{cav} = -\hat{\mathbf{d}}.\hat{\mathbf{E}}_{cav}, \tag{1.5}$$

$$\hat{H}_{ext} = -\hat{\mathbf{d}}.\hat{\mathbf{E}}_{ext}. \tag{1.6}$$

1.1.2 Jaynes-Cummings model

For the moment, we consider only the cavity contribution, and make an additional assumption: there is only one pair of atomic levels $|g\rangle$ and $|e\rangle$, and one cavity mode $c = (n,l,m,p)$ for which $\omega_a \equiv \omega_{ge} \simeq \omega_c$. This corresponds to the frequent experimental setting where the cavity is tuned near the atomic transition $|g\rangle \rightarrow |e\rangle$.

This allows to drop the contributions of the non-resonant cavity modes and reduces the Hamiltonian to:

$$\hat{H} = -\mathbf{d}_{ge}\mathbf{E}_0^{(c)}(\mathbf{r})(\hat{\sigma}_{ge} + \hat{\sigma}_{eg})(\hat{a}_c + \hat{a}_c^\dagger), \tag{1.7}$$

where $\hat{\sigma}_{ge} = |g\rangle\langle e| \equiv \hat{\sigma}$ is the "lowering" operator. The final step of the treatment consists in removing the non-resonant terms $\hat{\sigma}\hat{a}$ and $\hat{\sigma}^\dagger\hat{a}^\dagger$ (RWA approximation) to finally obtain the Jaynes-Cummings Hamiltonian [24]:

$$\hat{H}_{JC} = \hbar g(\mathbf{r})(\hat{\sigma}\hat{a}^\dagger + \hat{\sigma}^\dagger\hat{a}), \tag{1.8}$$

which also defines the atom-cavity coupling frequency

$$g(\mathbf{r}) = -\mathbf{d}_{ge}.\mathbf{E}_0^{(c)}(\mathbf{r})/\hbar. \tag{1.9}$$

Simple as it is, the Jaynes-Cummings Hamiltonian is the workhorse of the cavity QED community since it describes the essential feature of matter-light interaction in the quantum regime: coherent energy exchange between light and matter, with light absorption processes ($\hat{\sigma}^\dagger\hat{a}$) and emission ($\hat{\sigma}\hat{a}^\dagger$). The Hamiltonian therefore couples the bare states of the atom-cavity system by pairs $(|e,n-1\rangle, |g,n\rangle)$ with a frequency $g\sqrt{n}$ (for $n \geq 1$), where $|n\rangle$ denotes a cavity Fock state with n photons. The full Hamiltonian $\hat{H} =$

$\hbar\omega_a\hat{\sigma}^\dagger\hat{\sigma} + \hbar\omega_c\hat{a}^\dagger\hat{a} + \hat{H}_{JC}$ can then be exactly diagonalised. The eigenstates $|n,\pm\rangle$ are called the dressed states since they are entangled states of the atom-cavity system. As a function of the atom-cavity detuning $\Delta_{ca} = \omega_a - \omega_c$, they have the following expressions:

$$|n,+\rangle = \cos\theta_n|e,n-1\rangle + \sin\theta_n|g,n\rangle, \tag{1.10}$$

$$|n,-\rangle = \sin\theta_n|e,n-1\rangle - \cos\theta_n|g,n\rangle, \tag{1.11}$$

where the angle θ_n is defined by

$$\begin{pmatrix} \Delta_{ca}/2 \\ g\sqrt{n} \end{pmatrix} = \sqrt{\Delta_{ca}/4 + g^2 n} \begin{pmatrix} \cos(2\theta_n) \\ \sin(2\theta_n) \end{pmatrix} \tag{1.12}$$

and the eigenfrequencies are

$$\omega_{n,\pm} = n\omega_c + \frac{1}{2}\left(\Delta_{ca} \pm \sqrt{\Delta_{ca}^2 + 4g^2 n}\right). \tag{1.13}$$

The spectrum is represented on Fig 1.1. Two striking features stand out when the atom-cavity system is quasi-resonant, i.e. for $\Delta_{ca} \lesssim g$. First, the degeneracy of the uncoupled atom-cavity system at $\Delta_{ca} = 0$ is lifted by an amount $2g\sqrt{n}$: this effect is called vacuum-Rabi-splitting. Second, the cavity becomes anharmonic when it is coupled to a single atom, which is essentially an anharmonic system. By applying a monochromatic radiation at a given frequency, one cannot climb the state ladder to large n values. In [25], the authors used this effect to demonstrate field quantisation in the cavity. This anharmonicity has also consequences on the statistics of transmitted light: by exciting state $|1,-\rangle$, Birnbaum et al. showed that the output photon flux is antibunched, since $n = 2$ states cannot be excited simultaneously [26]. Conversely, Kubanek et al. were able to excite directly the state $|2,-\rangle$ via a two-photon transition, and proved that the output flux was in that case bunched [27]. At larger detunings, the dressed states approach the eigenstates of the uncoupled system, although their energy is shifted by a an amount depending on the photon number. This energy shift can be thought as a means of measuring non-destructively the cavity photon number [28].

1.1.3 Master equation

A complete description of the atom-cavity system requires to take into account other processes than coherent interaction with the cavity field. The main incoherent processes are the atomic decay (or spontaneous emission) and the cavity decay. Besides, we need to include in our description the probe field which injects photons in the cavity mode. The decay processes

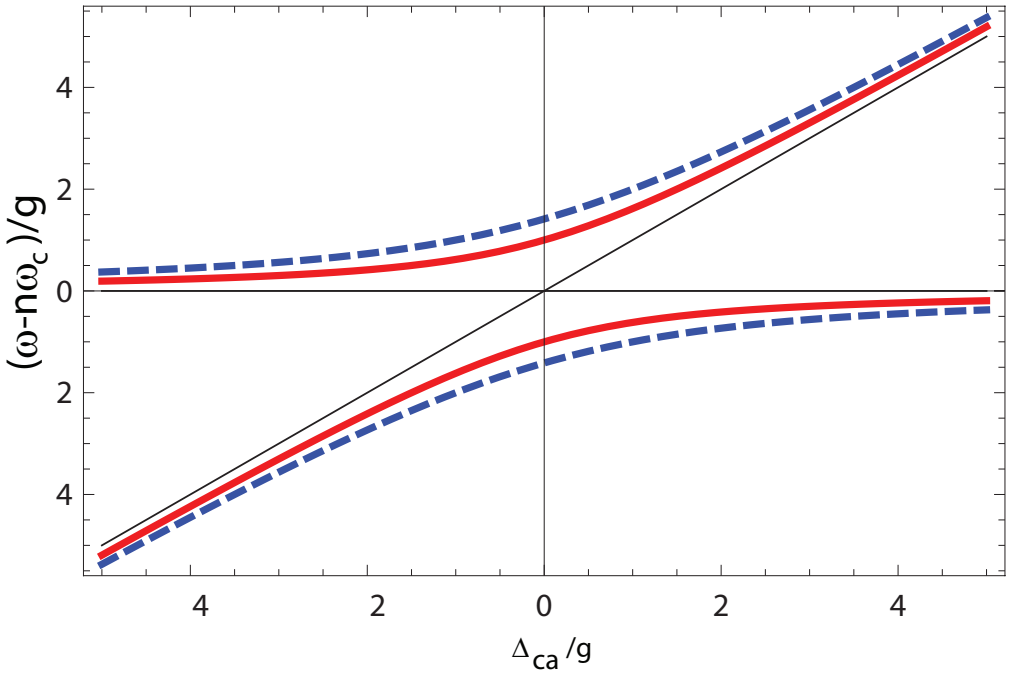

Figure 1.1: Spectrum of Jaynes-Cummings Hamiltonian. The eigenfrequencies $\omega_{n,\pm}$ are depicted as a function of the atom-cavity detuning Δ_{ca}, for different degrees of excitation: $n = 1$ (full red line) and $n = 2$ (dashed blue line). The bare spectrum is represented by black lines $\omega - n\omega_c = 0$ and $\omega - n\omega_c = \Delta_{ca}$.

are incoherent, and have to be treated in the framework of the master equation for the density matrix ρ. The master equation takes the general linear form

$$\frac{d\rho}{dt} = \mathcal{L}\rho = -\frac{i}{\hbar}[H, \rho] + \mathcal{L}_{dec}\rho, \tag{1.14}$$

The linear operator $\mathcal{L}$ is called the Liouvillian. The brackets $[\cdot, \cdot]$ denote the matrix commutator. The term $\mathcal{L}_{dec}\rho$ includes decay terms that cannot be cast into a commutator with a hermitian operator.

Spontaneous emission

Spontaneous emission originates from the interaction of the atom with the external electromagnetic field. An atom excited to state $|e\rangle$ can emit a photon of energy ω_{ge}, and decay to the ground state $|g\rangle$. By tracing over external electromagnetic modes[1], the evolution of the atom-cavity density matrix reads:

$$\mathcal{L}_{sp}\rho = \gamma' \left(2\hat{\sigma}\rho\hat{\sigma}^\dagger - \{\rho, \hat{\sigma}^\dagger\hat{\sigma}\}\right), \tag{1.15}$$

where the brackets $\{\cdot, \cdot\}$ denote the anticommutator. The spontaneous emission rate $2\gamma'$ differs from the free space one $2\gamma = \frac{\omega_{eg}^3 \mathbf{d}_{eg}^2}{3\pi\varepsilon_0\hbar c^3}$ if the external field mode structure is modified strongly by the presence of the cavity. This is the case for example with a fully enclosed cavity with prevents the external modes propagation to the cavity location. However, for an open axial cavity which supports only quasi-planar modes propagating along the cavity axis, as it is the case for our experimental setup, the spontaneous emission rate is nearly unchanged and we will assume $\gamma' = \gamma$ in what follows.

Cavity pumping and decay

The cavity mirrors can be pretty good, with a finesse up to a few millions in the optical domain, however they always transmit some light and couple the cavity modes to at least one external mode of the electromagnetic field. In some sense it is good news, because otherwise we would not be able to send light in the cavity. The cavity pumping and decay require then to be treated simultaneously. The cavity decay is an incoherent process which causes the loss of cavity photons to the outside world. It can be reprensented by the Liouvillian

$$\mathcal{L}_{cav}\rho = \kappa \left(2\hat{a}\rho\hat{a}^\dagger - \{\rho, \hat{a}^\dagger\hat{a}\}\right), \tag{1.16}$$

defining the cavity decay rate 2κ. The average lifetime of a single photon in the cavity mode is then $1/2\kappa$.

[1] A complete derivation is given in [29, p.25].

The pump term is a bit more problematical. The phenomenological so-called Gardiner-Collett Hamiltonian [30]

$$\hat{H}_p = -i\hbar\eta \exp(i\omega t)\hat{a} + \text{ h.c.} \tag{1.17}$$

accounts for a coupling with an external coherent field with a frequency ω. However this choice, although having a nice and short expression, is far from being obvious. In particular the value of the parameter η is pretty hard to derive directly from the incident field amplitude. Such a derivation is done in [31], and in [32, p. 255] with a greater level of detail. It also explains the linear form $E_{ext}.E_{cav}$ for the coupling. The main idea is the following: the decomposition into eigenmodes of the electromagnetic field has to be done taking into account cavity losses, and *before* field quantisation. The cavity mode is then only part of a global mode of the field, and the linear coupling of Eqn. 1.17 comes from the superposition of the external contribution and the cavity contribution at the position of the mirrors. The evolution of a pumped cavity (with no atom inside) can be exactly solved, changing to the rotating frame with frequency ω. The cavity state evolves at a rate κ towards a coherent steady state $|\alpha\rangle$ with $\alpha = \eta/(i\Delta_c - \kappa)$, where we defined $\Delta_c = \omega - \omega_c$. This result is consistent with the classical theory of Fabry-Perot cavities, as it is expected for any quantum harmonic oscillator. The intracavity field has a well-defined phase with respect to the pumping field, and the photon number $n = |\alpha|^2$ has a Lorentzian profile peaked at resonance $\Delta_c = 0$, with a FWHM equal to 2κ. The photon number on resonance $n_0 = \eta^2/\kappa^2$ is a convenient alternative to η to describe the input probe power.

To conclude, the dynamics of the atom-cavity system is given by the Liouvillian

$$\mathcal{L}\rho = -i[\hat{H}, \rho] + \mathcal{L}_{sp}\rho + \mathcal{L}_{cav}\rho, \tag{1.18}$$

where the Hamiltonian $\hat{H}$ is defined in the rotating frame by

$$\hat{H} = -\Delta_a \hat{\sigma}^\dagger\hat{\sigma} - \Delta_c \hat{a}^\dagger\hat{a} + g(\mathbf{r})(\hat{a}^\dagger\hat{\sigma} + \hat{a}\hat{\sigma}^\dagger) - i\eta(\hat{a} - \hat{a}^\dagger), \tag{1.19}$$

with the detunings $\Delta_a = \omega - \omega_a$, $\Delta_c = \omega - \omega_c$.

1.2 Optical response of the atom-cavity system

In this section we investigate the steady state of the system, in terms of cavity field amplitude and atomic state. For this purpose we assume the atom remains at a fixed position $\mathbf{r}_0$.

First we will give an analytical solution to the problem, valid in the limit of weak excitation. Then, we will discuss the exact validity of the approximations we made.

1.2.1 Analytical solution to the master equation

In the limit of weak excitation, only three possible states of the system can be populated: $|g,0\rangle$, $|g,1\rangle$ and $|e,0\rangle$. The Hamiltonian and all other operators can therefore be truncated to this subspace of dimension 3. The master equation is reduced to a linear problem $d\rho/dt = \mathcal{L}\rho$, where $\mathcal{L}$ is a 9×9 matrix. The steady state of the system is the solution to the equation $\mathcal{L}\rho_{ss} = 0$. This problem can be exactly solved. In [33], the authors used Ehrenfest equations to rewrite it in terms of evolution of the average values of the operators $\hat{a}$, $\hat{\sigma}$, and products, allowing to calculate all the properties of the steady state such as the mean cavity photon number $\langle\hat{a}^\dagger\hat{a}\rangle$ and the atomic excitation probability $\langle\sigma^\dagger\sigma\rangle$.

With the definitions

$$\tilde{\Delta}_a = \Delta_a + i\gamma \tag{1.20}$$
$$\tilde{\Delta}_c = \Delta_c + i\kappa \tag{1.21}$$
$$A = g^2 - \tilde{\Delta}_a\tilde{\Delta}_c, \tag{1.22}$$

the steady state solution is given by:

$$\begin{aligned}
\langle\hat{a}\rangle_{ss} &= \frac{i\eta\tilde{\Delta}_a}{A} \\
\langle\hat{\sigma}\rangle_{ss} &= \frac{i\eta g}{A} \\
\langle\hat{a}^\dagger\hat{a}\rangle_{ss} &= \frac{\eta^2|\tilde{\Delta}_a|^2}{|A|^2} \\
\langle\hat{\sigma}^\dagger\hat{\sigma}\rangle_{ss} &= \frac{\eta^2 g^2}{|A|^2} \\
\langle\hat{\sigma}^\dagger\hat{a}\rangle_{ss} &= \frac{\eta^2 g\tilde{\Delta}_a}{|A|^2}
\end{aligned} \tag{1.23}$$

We observe than the mean values of operator products factorise. As a consequence, the solutions to these quantum equations are the same as the solutions to the semiclassical[2] problem derived by Lugiato in his study of optical bistability [34], although the assumptions we made here to derive them are

[2] In the semiclassical picture, only the field is treated classically.

different. We can expand the solution for the number of photons in the cavity mode $n_{\rm cav} = \langle \hat{a}^\dagger \hat{a} \rangle_{ss}$ as:

$$n_{\rm cav} = \frac{\eta^2/\kappa^2}{\left(1 + \frac{g^2}{\kappa\gamma}\frac{1}{1+\Delta_a^2/\gamma^2}\right)^2 + \left(\frac{\Delta_c}{\kappa} - \frac{g^2}{\kappa\gamma}\frac{\Delta_a/\gamma}{1+\Delta_a^2/\gamma^2}\right)^2}, \tag{1.24}$$

which is exactly the result of Lugiato if we set the dimensionless cooperativity factor to the value

$$C = \frac{g^2}{2\kappa\gamma} \tag{1.25}$$

1.2.2 Limitations to the analytical solution

The equations 1.23 are very convenient, however one needs to be careful when using them since the small parameter of the expansion is difficult to identify precisely. We might be tempted to do the following statement: if the populations in states $|g;1\rangle$ and $|e;0\rangle$ are small in the steady state, then there is no chance to populate states like $|e;1\rangle$ or $|g;2\rangle$. The small parameter of the system is therefore $\max(\langle \hat{a}^\dagger \hat{a} \rangle_{ss}, \langle \hat{\sigma}^\dagger \hat{\sigma} \rangle_{ss}) \sim \eta^2/g^2$. We will however show here that this picture fails.

For that purpose, we write the master equation taking into account states $|g;n\rangle$ and $|e;n\rangle$ for $n = 0 \ldots n_{max}$ in a matrix form[3] and compute numerically the steady state density matrix for different values of n_{max}. For that matter we only need to solve a linear equation like $\mathcal{L}\rho_{ss} = 0$. For n_{max} large enough, the solution does not change anymore and can be considered exact. From the calculated density matrix we can compute the expectation values for the cavity photon number $\hat{a}^\dagger \hat{a}$ and the atomic excitation $\hat{\sigma}^\dagger \hat{\sigma}$. On Fig.1.2, we compare the results with those of Eqns 1.23. In the strong coupling regime (large g), we find a large deviation for the cavity transmission, with a factor of up to 100 for $n_0 = \eta^2/\kappa^2 = 10^{-1}$. However, the value of η^2/g^2 is then $\sim 10^{-2}$ and indicates that the analytical solution should hold for this probe power. The value of n_0 in a typical experiment with a detected photon flux of 1 MCts/s is $n_0 = 2.5 \times 10^{-2}$, so we have to take into account this correction to the analytical solution to analyse our results. However, the estimation of the atomic excitation is in good agreement with numerical solutions. A conservative upper bound for the validity of the analytical solution is $n_0 \ll \gamma^2/g^2 \sim 10^{-4}$. In that case, the probe power is intrinsically too small to excite the atom, even when light is fully transmitted through the cavity.

[3] We used the Quantum Optics Toolbox developed by S.M. Tan available online http://www.qo.phy.auckland.ac.nz/qotoolbox.html.

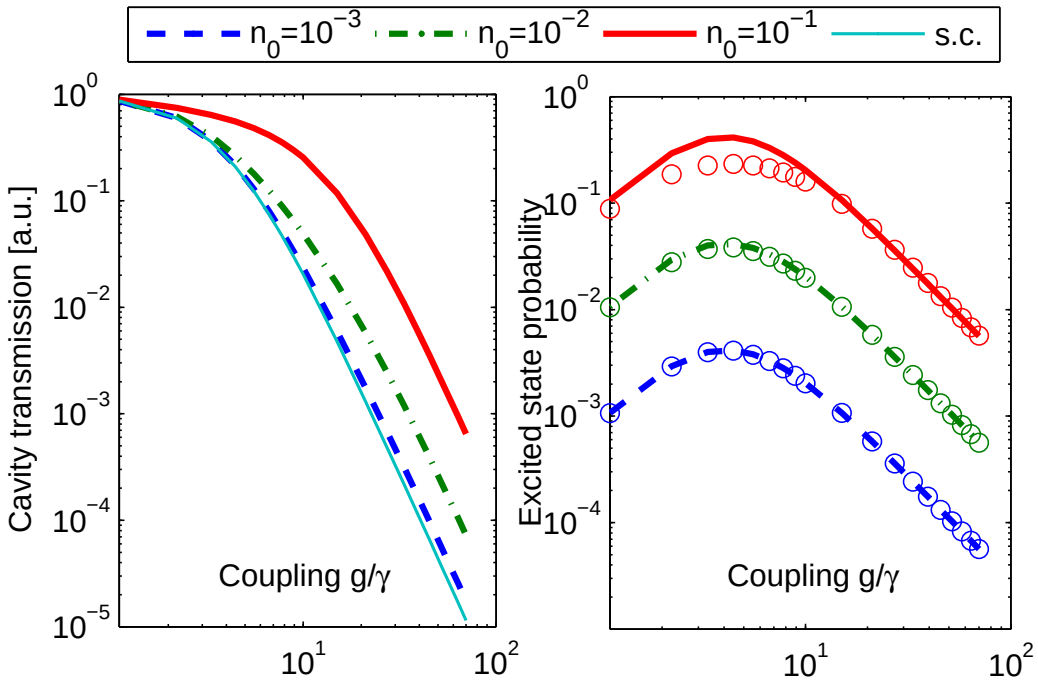

Figure 1.2: Comparison of numerical and analytical steady state solutions to the master equation, on resonance ($\Delta_a = \Delta_c = 0$) for different probe powers corresponding to $n_0 = \eta^2/\kappa^2 = 10^{-3}$ (blue) , 10^{-2} (green) , 10^{-1} (red) .
Left: cavity transmission n_{cav}/n_0 versus coupling g. Different probe powers correspond to the different curves, the analytical solution (light blue) corresponding to the low power limit.
Right: probability of atomic excitation $\langle \hat{\sigma}^\dagger \hat{\sigma} \rangle_{ss}$. We compare the numerical results (circles) with the analytical solution (lines).

This can be rewitten as $\eta^2/g^2 \ll 1/C^2$, a condition much more stringent than the initial $\eta^2/g^2 \ll 1$.

1.3 The cavity as a single atom detector

In this section we show that a cavity can be used as a single atom detector. We will compute the detection efficiency (or error probability) if the cavity is used as a qubit measurement device, and compare it to a free space detector. We will then show that the cavity may also be able to count small numbers of non-resonant atoms.

1.3.1 Detection of a resonant single atom

We now consider the situation of a single atom resonant with the cavity, $\Delta_{ca} = 0$.

When the single atom cooperativity factor is large, the transmission of the cavity is strongly modified compared to the empty cavity value. This is always the case in the *strong coupling regime* defined by $g \gg \kappa$ and $g \gg \gamma$. In that regime, the transmission peak of the empty cavity is splitted into two peaks corresponding to the frequencies of the dressed states, see Fig. 1.3 below.

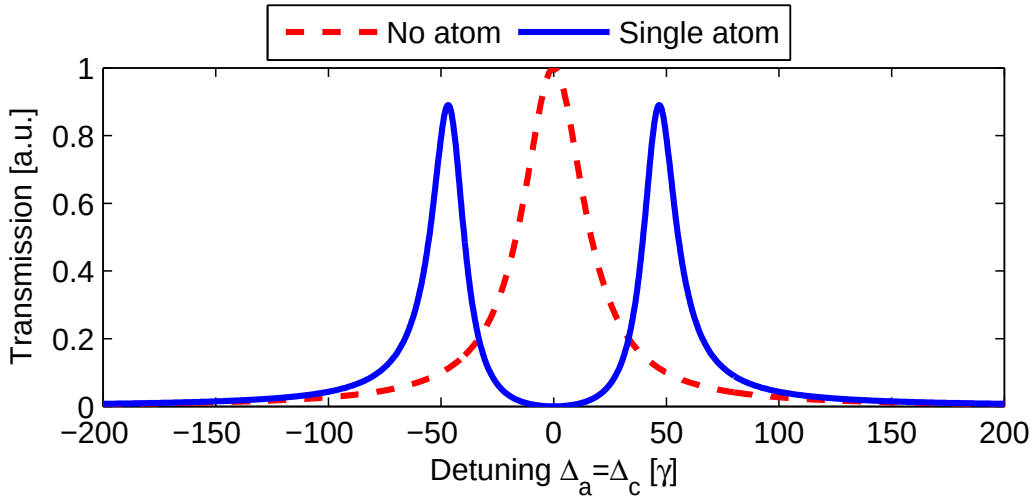

Figure 1.3: Numerical steady state solution to the master equation in the weak excitation regime, for a resonant atom cavity system $\Delta_{ca} = 0$. The cavity transmission is depicted as a function of the global detuning $\Delta_a = \Delta_c$, for an empty cavity (dashed red line) and a cavity with a single atom inside with a coupling $g = 2\pi \times 140$ MHz. The other parameters are the ones relevant to the experiment: $\kappa = 2\pi \times 50$ MHz, $\gamma = 2\pi \times 3$ MHz.

We particularly find that in the resonant configuration $\Delta_{ca} = 0$, the cavity transmission is reduced by a huge factor $(2C)^2 \sim 10^4$ at the resonance $\Delta_c = 0$, in the limit of weak excitation. Probing the cavity at resonance therefore provides an excellent detection signal for single atoms: the cavity transmission will be high if there is no atom inside, and low if there is (at least) one atom.

1.3.2 Detection of non-resonant atoms

We can also consider the situation where the atom is far off resonant to the cavity, precisely the limit $\Delta_c a \gg g^2/\kappa$. We will encounter this case in the experiment, when a single atom is in the $|F = 1\rangle$ hyperfine state, with the cavity tuned to the $|F = 2\rangle \rightarrow |F' = 3\rangle$ transition. The cavity is therefore detuned by an amount $\Delta_{ca} = \Delta_{HFS} = 2\pi \times 6.8$ GHz with respect to all possible atomic transitions starting from state $|F = 1\rangle$, see Fig. 1.4.

The field in the cavity is given in that case by

$$\alpha = \frac{i\eta}{\left(-\frac{g^2}{\Delta_{ca}} - \Delta_c\right) + i\kappa} \tag{1.26}$$

The effect of such a far detuned atom is then equivalent to a change of the cavity resonance frequency by an amount $\delta_c = \omega_c' - \omega_c = -g^2/\Delta_{ca}$. This effect can be seen as a change of the refractive index of the medium inside the cavity.

Compared to the resonant case, we have to consider the three possible transitions $|F = 1\rangle \rightarrow |F' = 0, 1, 2\rangle$ which all contribute to the cavity shift. However, since the relative detunings between these transitions (~ 100 MHz) is negligible compared to the ground state hyperfine splitting, the effect of the three transitions simply add up in the coupling constant g_1. The precise value of g_1 can be computed from sum rules [35] and yields the formula

$$g_1 = \sqrt{\frac{2}{3}} g_{22\rightarrow 33}^{\sigma^+} \tag{1.27}$$

which connects the coupling factors of $|F = 1\rangle$ and $|F = 2\rangle$ atoms. The cavity shift is then $\delta_c = -g_1^2/\Delta_{HFS}$. We can now compute numerically these shift for our experimental setup: we find that for optimally coupled atoms, the single atom shift is $2\pi \times 4.3$ MHz. Is therefore much smaller than the linewidth $\kappa = 2\pi \times 50$ MHz and only reduces the transmission by a small amount. For several atoms in the $|F = 1\rangle$ state, single atom shifts add up so that the global cavity shift is given by $\delta_c = -N_1 g_1^2/\Delta_{HFS}$, where N_1 is

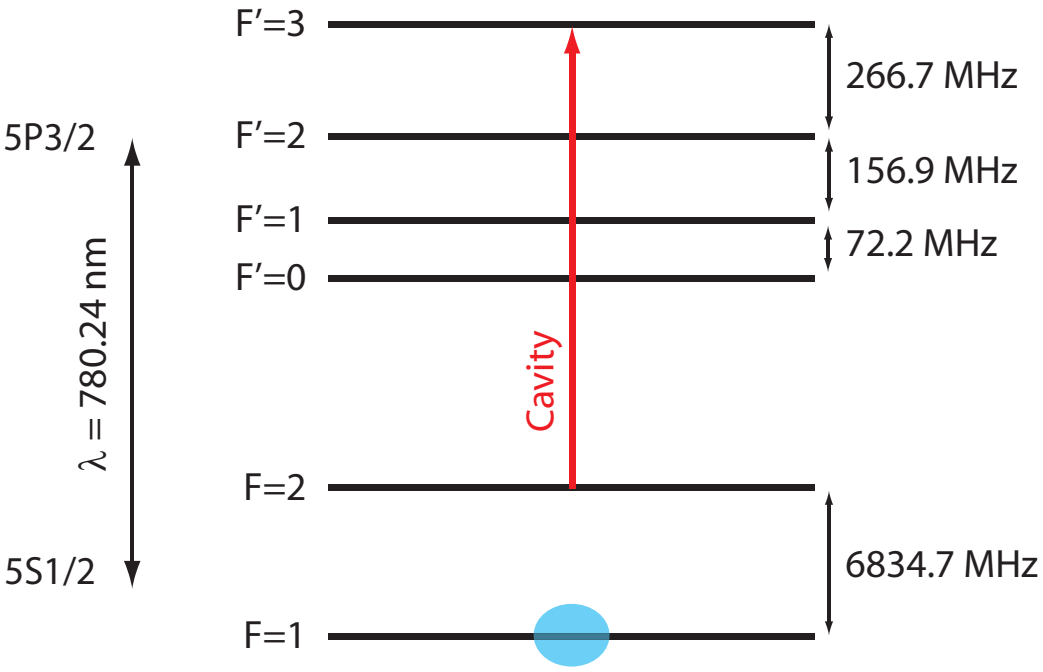

Figure 1.4: Level scheme for the detection of non-resonant $|F = 1\rangle$ atoms. The cavity is tuned to $|F = 2\rangle \rightarrow |F' = 3\rangle$ transition.

the number of atoms. The shift of the cavity is therefore comparable to the linewidth κ for $N_1 \sim 10$. We can therefore determine the number of atoms in the $|F = 1\rangle$ state by measuring the cavity transmission at resonance, and compute the corresponding shift (see Fig. 1.5). We should notice here that a phase measurement would be more appropriate in this regime if we wanted to measure small number of atoms. It is however not compatible with the experimental setup so we do not discuss it in detail.

1.3.3 Comparison between free space and cavity detection

We have seen previously that a cavity used in the resonant configuration can be used to detect a single atom with an excellent signal, the transmission of the cavity dropping almost to zero with an atom inside. We have also seen that a single non-resonant atom (e.g. in the $|F = 1\rangle$ state when the cavity is resonant to the $|F = 2\rangle \rightarrow |F' = 3\rangle$ transition) has almost no effect on the cavity transmission. The cavity can therefore be used as a measurement device of the F number of a single atom, for example for applications to

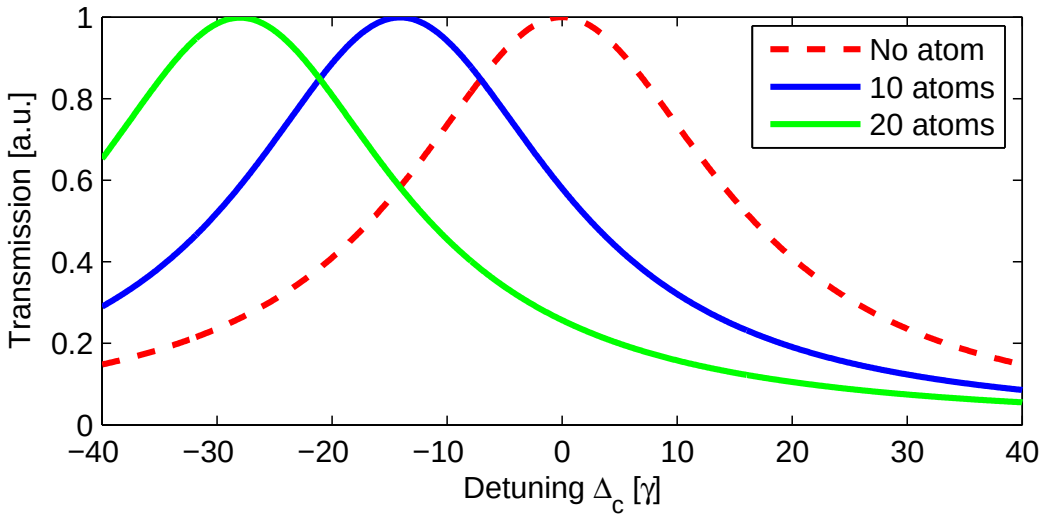

Figure 1.5: Steady state solution to the master equation in the weak excitation regime, for a non-resonant atom cavity system $\Delta_{ca} = \Delta_{HFS} = 2\pi \times 6.8$ GHz. The cavity transmission is depicted as a function of the cavity detuning detuning Δ_c, for different atom numbers. The single atom effective coupling is set to $g_1 = 2\pi \times 170$MHz, corresponding to perfect coupling in the experiment.

quantum information processing where the qubit is the atomic state. In this section, we quantify the efficiency of the cavity as a measurement device.

The performance of any measurement device is characterised by the probability that the state inferred from its output corresponds to the real state, called the fidelity F. We define the error probability as $\mathcal{P}_{err} = 1 - F$. We suppose that a single atom is trapped in the cavity mode, and can be in two possible states $|1\rangle = |F = 2\rangle$ and $|0\rangle = |F = 1\rangle$ with *equal* probability. This corresponds to the situation in quantum information processing where we have *a priori* no information about the state of the system before the measurement.

To determine in which state the system is, we switch on the detection light for a duration t_{int} and detect N photons with the APD. From this measurement, we have to make a guess of the state of the system:$|0\rangle$ or $|1\rangle$? If the atom was in the $|1\rangle$ state, the transmission of the cavity is very small and $N = 0$, if we suppose that the detection light pulse was brief. In the atom was in the $|1\rangle$ state, the cavity transmits and the number of detected photons is a Poissonian distribution with the mean value $N_{ref} = \eta^2 t_{int}/\kappa$. We therefore guess that the state is $|1\rangle$ when $N = 0$, and otherwise we guess

that it is $|0\rangle$. The error probability is then

$$\mathcal{P}_{err} = \frac{1}{2}\exp(-N_{ref}). \tag{1.28}$$

The most important feature of cavity detection is that the light is not scattered by the atom, but rather reflected by the cavity.

Using the analytical solution to compute the spontaneous emission rate,

$$\Gamma_{sp} = 2\gamma\langle\hat{\sigma}^\dagger\hat{\sigma}\rangle_{ss} = \frac{2\gamma\eta^2 g^2}{|A|^2} \simeq \frac{2\gamma\eta^2}{g^2}, \tag{1.29}$$

we find that the fraction of scattered power $P_{scatt}/P_{in} \simeq 1/C$ is much smaller than 1. The number of spontaneous emission events occurring during a single atom detection can therefore be made very small. The error probability can be rewritten as

$$\mathcal{P}_{err} = \frac{1}{2}\exp(-CN_{sp}), \tag{1.30}$$

where N_{sp} is the number of spontaneously emitted photons during the detection pulse, if the atom was present. This shows that we can achieve a very efficient measurement, while at the same time having on average much less than 1 spontaneous emission, when the cooperativity is much larger than 1. Including an optical loss factor $L < 1$ for the detection of the transmitted photons, the formula is changed to

$$\mathcal{P}_{err} = \frac{1}{2}\exp(-CN_{sp}L). \tag{1.31}$$

Let us now compare with a free space detection scheme. A very efficient free space scheme consists in exciting the atom, and then collecting the spontaneously emitted photons. Repeating this process n times, the number of collected photons is on average nL if the atom was resonant[4], and 0 otherwise, while the number of spontaneous emissions is $N_{sp} = n$. Therefore the error probability is

$$\mathcal{P}^{fs}_{err} = \frac{1}{2}\exp(-N_{sp}L). \tag{1.32}$$

This shows that a cavity detection setup outperforms a free space detector in terms of spontaneous emission by a factor C.

[4] We assumed here an equal loss factor L. This is true for the APD efficiency contribution to the loss factor, but certainly not for the collection efficiency which is much smaller in the case of fluorescence photons. We nevertheless assumed the same value to compare the cavity detection with an ideal free space detector.

However, it would be wrong to claim at this point that we can achieve a perturbation-free measurement with a cavity, just by considering spontaneous emission. The effect of intracavity light, as weak as it may be, can affect the motional state of the atom, and also its internal state. These processes will be described in Sect.1.4 and 1.5.

We can conclude from this section that the measurement of the cavity transmission on resonance ($\Delta_c = 0$) can be used detect a single resonant atom, or to measure small numbers of atoms in a non-resonant state. In the experiments, we will take advantage of these two configurations to detect atoms in $|F = 2\rangle$ state (usually resonant with the cavity) or in $|F = 1\rangle$ state (non-resonant). The detection of a single resonant atom in a cavity induces much less spontaneous emission as a free space detection with the same efficiency, making it a useful device for the preparation of single atoms in a low-energy state. The effect of the detection on motional and Zeeman quantum numbers will be discussed in more detail in the next two sections.

1.4 Atomic motion in the cavity

The coupling g between the atom and the cavity depends on the position of the atom in the cavity mode $\mathbf{r}$. To obtain a large coupling, we trap the atom at the position of the cavity field maximum using an intracavity dipole far off resonant dipole trap. The dipole trap has mainly two effects: it provides a conservative trapping potential, and shifts the atomic resonance by an amount called lightshift. Besides, the light sent to detect the atom also causes a light force. This force fluctuates, and manifests as a heating mechanism which tends to move the atom away from the dipole trap bottom, where the coupling to the detection light mode (called cavity mode until now) is also maximum. As a consequence, the coupling decreases and the detection gets less efficient.

In this section, we will describe first the intracavity dipole trap and estimate the light shift. Then we will compute the forces and heating rate acting on the atom. Finally we will estimate the consequences of this heating mechanism on the detection of the atom, by evaluating the cavity transmission for different atomic "temperatures".

1.4.1 Intracavity dipole trap and light shift

In the experiment, a dipole trap is generated by pumping a second cavity mode far off-resonant to atomic transitions. Since the dipole trap is not

resonant to a specific atomic transition, we have to write the interaction between the atom and the dipole trap field in the most general form and take into account all possible atomic states $|i\rangle$:

$$H_{dip} = -\hat{\mathbf{d}}.\hat{\mathbf{E}}_{dip}, \tag{1.33}$$

with $\hat{\mathbf{E}}_{dip} = \mathbf{E}_0^{(dip)}(\mathbf{r})\hat{b} +$ h.c.. This Hamiltonian couples non resonantly the bare states $|i;n\rangle$ with states $|j;n+1\rangle$ or $|j;n-1\rangle$. Applying second order perturbation theory, this generates a shift of the bare state energy $\mathcal{E}_i$ by an amount:

$$\Delta\mathcal{E}_i = \hbar\Delta_S^i = |E_0^{(dip)}(\mathbf{r})|^2 \sum_j \frac{(n+1)|d_{ij}|^2}{\mathcal{E}_i - \mathcal{E}_j - \hbar\omega_{dip}} + \frac{(n)|d_{ij}|^2}{\mathcal{E}_i - \mathcal{E}_j + \hbar\omega_{dip}}, \tag{1.34}$$

where $\mathbf{E}_0^{(dip)}(\mathbf{r}) = E_0^{(dip)}(\mathbf{r})\mathbf{e}_{dip}$ and $d_{ij} = \langle i|\mathbf{d}.\mathbf{e}_{dip}|j\rangle$. In the previous sum, only states $|j\rangle$ with frequencies $\mathcal{E}_j \sim \mathcal{E}_i \pm \hbar\omega_{dip}$ contribute significantly.

To be more specific, we now consider the states relevant to our experiment: a ground state $|g\rangle$ in the $5S_{1/2}$ multiplet and an excited state $|e\rangle$ in the $5P_{3/2}$ multiplet. We also set the dipole trap light wavelength to 830nm.

For the state $|g\rangle$, the dominant contributions come from transitions to $5P_{1/2}$ states (D1 line at 795nm) and $5P_{3/2}$ states (D2 line at 780nm). Due to symmetry properties, the sums $\sum_{j\in 5P_{1/2}} |d_{ij}|^2 = d_{D1}^2$ and $\sum_{j\in 5P_{3/2}} |d_{ij}|^2 = d_{D2}^2$ are independent of the particular state $|i\rangle$ when the light polarisation $\mathbf{e}_{dip}$ is *linear*. Their values can be related to the decay rate of the 5P levels $\Gamma = 2\gamma = 2\pi \times 6$ MHz and the $5S - 5P$ transition frequency ω_a by the relations [36]:

$$d_{D1}^2 = \frac{\hbar\pi\varepsilon_0 c^3\Gamma}{\omega_a^3} = 2.1 \times 10^{-58}\,\mathrm{C^2m^2} \tag{1.35}$$

$$d_{D2}^2 = \frac{2\hbar\pi\varepsilon_0 c^3\Gamma}{\omega_a^3} = 2d_{D1}^2 \tag{1.36}$$

The ground state energy is then shifted downwards by:

$$\Delta\mathcal{E}_i = \hbar\Delta_S^i = |E_0^{(dip)}(\mathbf{r})|^2 n_{dip} d_{D1}^2 \left(\frac{1}{\hbar\omega_{dip} - \hbar\omega_{D1}} + \frac{2}{\hbar\omega_{dip} - \hbar\omega_{D2}}\right), \tag{1.37}$$

where n_{dip} is the number of photons in the dipole trap cavity mode. The effect of dipole trap light is then to generate a trapping potential $U_{dip} = \hbar\Delta_S^i$ for ground state atoms. This potential scales like the light intensity $\sim |E_0^{(dip)}(\mathbf{r})|^2 n_{dip}$, and it has the same geometry as the mode. For a standing

wave mode as we have in the experiments, it generates a 1D array of equally spaced traps along the cavity axis. The potential has a minimum where $|E_0^{(dip)}(\mathbf{r})|$ is maximum, i.e. at the field antinodes.

For the excited state $|e\rangle$ in the $5P_{3/2}$ multiplet, the leading contribution is due to the coupling to the ground state, which yields a positive shift, with smaller contributions coming from several transitions to higher excited states [37, 38]. Contrary to the ground state levels, the exact value of the light shift depends on the specific Zeeman state considered and the dipole trap polarisation. We can nevertheless compute the sign and order of magnitude with the knowledge of the lifetimes of the excited states and the transition wavelengths:

Transition initial and final state	$5S_{1/2}$ $5P_{3/2}$	$5P_{3/2}$ $5D_{5/2}$	$5P_{3/2}$ $6S_{1/2}$	$5P_{3/2}$ $4D_{5/2}$	$5P_{3/2}$ $7S_{1/2}$
Wavelength [nm]	780	775	1360	1475	740
Relative light shift	+1	-0.1	+0.15	+0.3	-0.1

We can conclude from these figures that excited atoms excited feel a repulsive potential, which is of the same order of magnitude as ground state atoms, but with the opposite sign.

We can finally rewrite the atomic term in the Hamiltonian as

$$\hat{H}_{at} = -\Delta_a \hat{\sigma}^\dagger \hat{\sigma} + \Delta_S^e |e\rangle\langle e| + \Delta_S^g |g\rangle\langle g| = \Delta_S^g - \Delta_{a,eff} \hat{\sigma}^\dagger \hat{\sigma}, \tag{1.38}$$

which defines the (position-dependent) effective detuning

$$\Delta_{a,eff} = \Delta_a + \Delta_S^g - \Delta_S^e = \Delta_a - \Delta_{LS}. \tag{1.39}$$

In addition to the trapping potential for the ground state, the dipole trap also shifts the atomic transition frequency by the lightshift $\Delta_{LS} = \Delta_S^e - \Delta_S^g$.

1.4.2 Cavity force

In the previous section, we assumed that the atom remains at a fixed position $\mathbf{r}_0$ and took a constant atom-cavity coupling $g = g(\mathbf{r}_0)$ to compute the cavity transmission and the spontaneous emission rate. This approximation is valid as long as the atom-cavity coupling $g(\mathbf{r}(t))$ stays approximately constant for the time the cavity field and the atomic internal state need to reach their steady state value. This timescale is given here by $1/\kappa$. With an atom-cavity coupling of the form $g(\mathbf{r}) = g_0 \cos(ky) \exp(-\mathbf{r}_\perp^2/w^2)$, the coupling changes on a typical timescale $1/(kv)$. We can therefore separate the internal dynamics

of the atom (coupled to the cavity) from its external dynamics when $v \ll \kappa\lambda$. In the experiment, this condition will always be satisfied. We will also suppose that $v \ll \gamma\lambda$, which allows to neglect the Doppler effect. Also, we will neglect the quantisation of the atomic motion in the coupling with cavity light: this requires the atomic wavepacket to spread over a negligible fraction of the wavelength. In this *quasi-classical* picture[5], the operators $\hat{\mathbf{r}}$ and $\hat{\mathbf{p}}$ can be replaced by their classical values, with a stochastic evolution with a mean force field $\mathbf{F}$ and a momentum diffusion matrix D_{ij}. The derivation of the Fokker-Planck equation describing this stochastic evolution was done in [39] with a classical light field, and in [40] for a quantised light field. The small parameter enabling this quasi-classical treatment is $\hbar k_l^2/m\gamma$.

A huge amount of publications concern the calculations of these forces and momentum diffusion matrices, not to mention the cavity cooling force. In this section, we will briefly give the expressions for the forces and momentum diffusion which are relevant to our experiment, and point out the appropriate references we used.

At the zeroth order in $v\kappa/\lambda$, the force can be computed from the steady state density matrix as:

$$\mathbf{F} = \langle \hat{\mathbf{F}} \rangle = \langle -\nabla \hat{H} \rangle_{ss}. \tag{1.40}$$

The contribution of the atom-cavity coupling reads in the weak excitation regime [33]:

$$\mathbf{F}_{cav} = -\frac{2\hbar\eta^2 \Delta_a g \nabla g}{|A|^2}. \tag{1.41}$$

The probe light therefore attracts the atom to the region of strong coupling when $\Delta_a < 0$. The contribution of the dipole trap is given by:

$$\mathbf{F}_{dip} = \hbar \left(-\nabla \Delta_S^g - \nabla \Delta_{LS} \frac{\eta^2 g^2}{|A|^2} \right), \tag{1.42}$$

and is dominated by the first term since the atom spends most of its time in the ground state.

1.4.3 Momentum diffusion

The fluctuations of both the atomic state and the light fields induce a fluctuation of the force operator. In a fully classical picture, corresponding to our treatment of the atomic position and momentum, the force fluctuation

[5] The quasiclassical picture corresponds to the classical treatment of the atomic motion, but a quantised treatment of the internal state.

generates a momentum diffusion process on a timescale much longer than the force autocorrelation time. Here, the correlation time is of the order of $1/\kappa$. Following [41], we define the momentum diffusion constants D_{ij} for $i, j = x, y, z$ as

$$\frac{d}{dt}\overline{(p_i - \overline{p_i})(p_j - \overline{p_j})} = 2D_{ij}, \tag{1.43}$$

where $\overline{x}$ denotes here a classical ensemble average. If the atom is trapped, this can be seen as a heating process with a heating rate $dE/dt = \mathrm{Tr}D/m$. The momentum diffusion coefficients can be calculated from the general formula

$$D_{ij} = \int_0^\infty dt \left(\langle \hat{F}_i(0).\hat{F}_j(t) \rangle_{ss} - F_i F_j \right). \tag{1.44}$$

In the force operator $\hat{F}$, we have to consider the contribution of the coupling to the external modes (spontaneous emission term), and the coupling to the cavity modes (cavity term).

Contribution of spontaneous emission

The contribution of the spontaneous emission to the momentum diffusion matrix is a well-known calculation and the result reads [41]:

$$\mathbf{D}_{sp} = \mathbf{A}_{sp}(\hbar k)^2 \frac{1}{2}\Gamma_{sp} = \mathbf{A}_{sp}(\hbar k)^2 \frac{\gamma \eta^2 g^2}{|A|^2}, \tag{1.45}$$

where $\mathbf{A}_{sp}$ is the dipole emission pattern, a symmetric matrix with $\mathrm{Tr}(\mathbf{A}_{sp}) = 1$, and depends on the cavity field polarisation. This expression corresponds to the intuitive picture of a diffusion driven by random recoils of momentum $\hbar k$, occurring at a rate Γ_{sp}.

Contribution of cavity modes

The contribution of the cavity modes can be computed analytically with the help of the quantum regression theorem (see for example [29]) in the weak excitation limit. The diffusion is mainly concentrated along the cavity axis, and corresponds to random absorption and reemission of cavity photons in opposite directions. When the light shift is not negligible as it the case in our experiment ($\Delta_{LS} \sim g$) and depends on the position, the expression is somehow lengthy and can only be found in [38, App. B] to our knowledge.

We can add up the two contributions to estimate the global heating rate of the atom $\mathrm{Tr}(D_{sp} + D_{cav})/m$ for our experimental setting, averaged over a thermal position distribution. The result is plot on Fig. 1.6, for various

detunings Δ_a and temperatures T. The average heating rate is below 100 μK/ms for a probe light power corresponding to $n_0 = 2.5 \times 10^{-2}$ ($\Phi_{ref} = 1.2$ MCts/s), as long as the temperature is low enough. The average heating rate increases with the temperature, since the atom can then reach regions of weaker coupling. The dependence on the probe-atom detuning is quite weak, although the minimum heating rate corresponds also here to $\Delta_{a,eff} \simeq 0$. We can estimate the typical time needed to reach a temperature of 1 mK is of the order of 100 ms at this detection power. At 100 μK and $\Delta_{a,eff} = 0$, the heating rate is approximately 2.5 μK/ms along the cavity axis, and 0.8 μK/ms along each transverse axis, if we take an emission pattern $A_{sp} = [1/3; 1/3; 1/3]$.

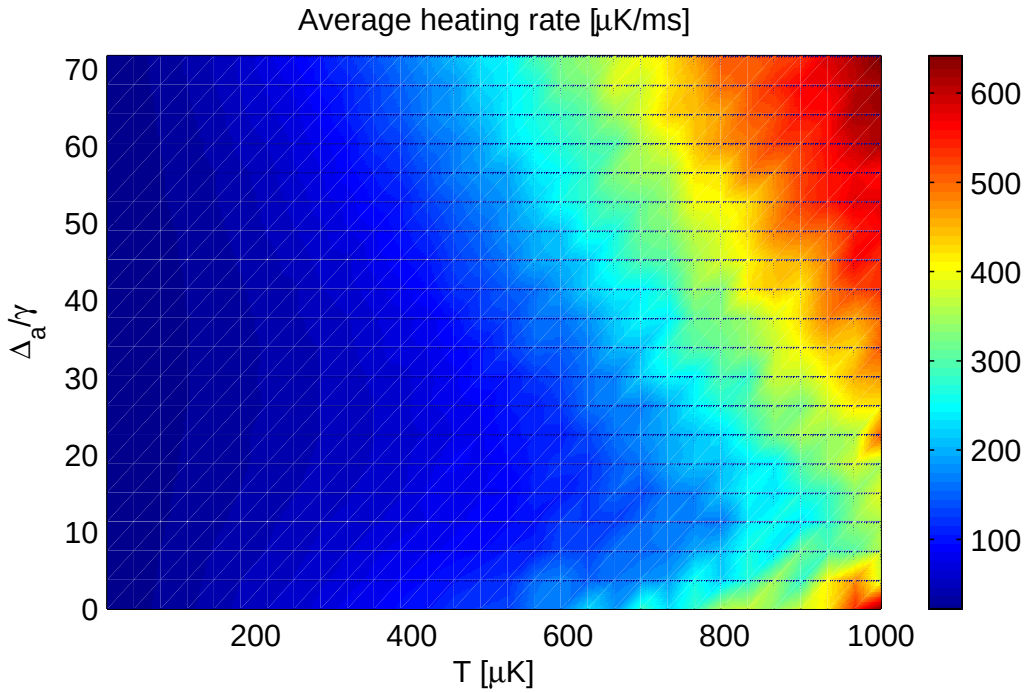

Figure 1.6: Average heating rate induced by detection light. Parameters are $n_0 = 2.5 \times 10^{-2}$, $g_0 = 2\pi \times 160$ MHz, $\Delta_c = 0$, $U_{dip} = k_b \times 2.6$ mK, $\Delta_{LS,0} = 2U_{dip}/\hbar = 2\pi \times 110$ MHz.

Heating rate of the dark dipole trap

Until now, we treated the intracavity dipole trap exactly as a position-dependent light shift. Although being far off resonant, the atom can absorb

and reemit light from the dipole trap beam. The scattering rate is proportional to dipole trap light intensity and the ratio depends on the detuning Δ: $\hbar\Gamma_{sp} = 2\gamma U_{dip}/\Delta$. With a detuning corresponding to approximately 50 nm, the scattering of dipole trap photons leads to heating with a typical time to reach the trap depth $\tau_{dip,fs} = m\Delta/(4\gamma\hbar k_d^2) \sim 40$ s at 830nm. However, for an intracavity dipole trap, the heating rate is enhanced by the cavity.

We can go one step backward in our description of the dipole trap, and treat the interaction between the atom and the dipole trap light in the Jaynes-Cummings picture (Eqn. 1.33). For that matter, we need to specify a two-level system. We suppose here that the dipole trap light does not resolve the hyperfine splitting between $5P_{1/2}$ and $5P_{3/2}$ states (15nm). Therefore, we can define a two-level system coupled by a dipole element $d_{eff} = \sqrt{d_{D1}^2 + d_{D2}^2} = d_{22\to 33}^{\sigma^+}$. The coupling g_d in the Jaynes-Cummings Hamiltonian is therefore equal to the coupling of an an atom in the state $|F = 2; m_F = 2\rangle$ with a circularly polarised cavity field, since the mode volume for 780nm and 830nm are approximately equal. We can the use the equations for momentum diffusion given in [33], and take the limit $\Delta_a \to \infty$:

$$D_{sp} = \frac{\hbar^2 k_d^2 \gamma \eta_{dip}^2 g_d^2}{\Delta_a^2 \kappa_d^2}, \tag{1.46}$$

$$D_{cav} = \frac{\hbar^2 (\nabla g_d)^2 \eta_{dip}^2 \gamma}{\Delta_a^2 \kappa_d^2} \left(1 + \frac{4g_d^2}{\gamma\kappa_d}\right). \tag{1.47}$$

The spontaneous emission term D_{sp} is therefore unchanged compared to a free space dipole trap of the same magnitude. The first term in D_{cav} is equivalent to the free space momentum diffusion associated with absorption of the light. On average, $g^2 \simeq (\nabla g/k)^2$ in a standing wave and this terms contributes equally as spontaneous emission. The second term in D_{cav} is specific to cavity heating, and turns out to be the largest contribution in the strong coupling regime. The ratio between the cavity-enhanced heating rate and the free space heating, for the same trap depth, is of the order of $2g_d^2/(\kappa_d\gamma) \sim 150$, taking here $g_d^2 = \frac{1}{2} g_d(\mathbf{r} = 0)^2$ and $\kappa_d = 2\pi \times 130$ MHz. However, this enhanced heating only takes place when the atom is not so well localised, since ∇g_d vanishes at the trap centre. Therefore, we have once more a position-dependent heating, which we can evaluate as a function of temperature, see Fig. 1.7. Starting at $T = 100\mu$K, the typical time to reach a temperature of 1 mK is of the order of 2s.

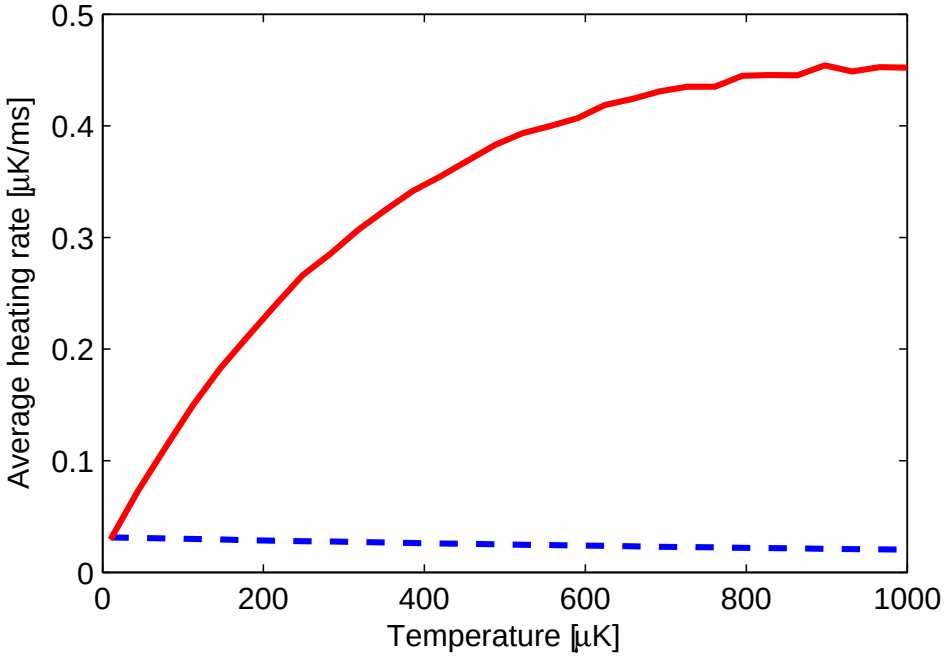

Figure 1.7: Average heating rate in the dark dipole trap, as a function of temperature (red line). The dashed blue line shows the heating rate of a corresponding free space dipole trap. We take $U_{dip} = 2.6$ mK.

1.4.4 Cavity transmission vs atom position

The optical response of the cavity depends on the position of the atom via both the coupling factor $g(\mathbf{r})$ and the position-dependent light-shift $\Delta_{LS}(\mathbf{r})$. With a TEM00 geometry for both the probe light mode and the dipole light mode, these functions can be written as:

$$g(\mathbf{r}) = g_0 \cos(k_p y) \exp(-\mathbf{r}_\perp^2/w^2), \quad (1.48)$$

$$\Delta_{LS}(\mathbf{r}) = \Delta_{LS,0} \cos(k_d y)^2 \exp(-2\mathbf{r}_\perp^2/w^2), \quad (1.49)$$

where the wavevectors k_p and k_d stand for probe light and dipole trap light, and we assumed that both modes have equal waists w, and the antinodes coincide at $y = 0$. Assuming a thermal distribution for the atomic position $\mathbf{r}$ centered at $\mathbf{r} = 0$, we can compute the average relative cavity transmission for different temperatures. The results are shown on Fig. 1.8, for typical experimental parameters. At very low temperature, the cavity transmission is minimum for $\Delta_a \simeq \Delta_{LS,0}$, corresponding to $\Delta_{a,eff} \simeq 0$. For larger temperatures, the optimum detection point moves towards smaller values of

Δ_a. We also see on this graph that the detection of relatively hot atoms ($T \sim T_{depth}/2$) is possible with the right choice of detuning. The main effect of the heating is then the possible loss of the atom, occurring when the temperature exceeds the trap depth.

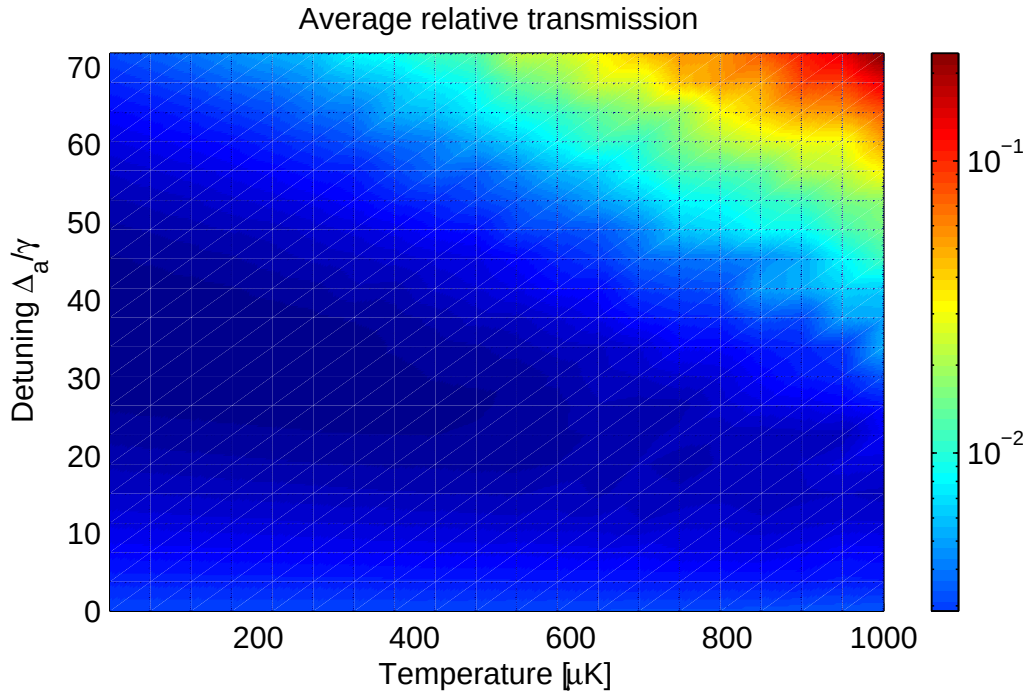

Figure 1.8: Average relative cavity transmission T versus temperature. Parameters are $n_0 = 2.5 \times 10^{-2}$, $g_0 = 2\pi \times 160$ MHz, $\Delta_c = 0$, $U_{dip} = k_b \times 2.6$ mK, $\Delta_{LS,0} = 2U_{dip}/\hbar = 2\pi \times 110$ MHz.

1.5 Multilevel structure and depumping effects

We shall investigate in this section the limits to the two-level treatment of the single atom in its interaction with the cavity mode. Basically, the two-level picture is completely rigorous when the two states considered form a stable subspace for the interaction with both the cavity light field and the external light field (spontaneous emission). If we consider the complete Zeeman substructure of the ^{87}Rb atom, we notice that this is only possible for the two pairs of states $|g\rangle = |F = 2; m_F = \pm 2\rangle$ and $|e\rangle = |F = 3; m_F = \pm 3\rangle$, when the cavity polarisation is $\sigma^{\pm}$. Unfortunately, we can cannot achieve this regime experimentally because the cavity eigenmodes are linearly polarised. We therefore need to consider a more complicated atomic structure than the simple two-level picture.

Cavity QED experiments with multilevel atoms have been performed previously, like for example the measurement of a Vacuum Rabi splitting with a single atom and a linear polarisation [42], and numerical simulations were performed to account for the differences to the two-level picture [43, Chap. 6].

In this section we will present a theory to describe the multilevel atom structure. We will insist on the similarities between the multilevel and the two-level picture, and see how a multilevel atom can be described using an effective coupling, in order to validate the predictions made in the previous section in terms of detection signal and heating rates. We will then apply the theory to the estimations of the depumping rates which are relevant to the experiments of Chap. 3 and 4. When the atom is magnetically trapped (Chap. 3), the observation time of a single atom is limited by the depumping to the magnetically untrapped Zeeman states. When there is a dipole trap instead (Chap. 4), the critical process is the depumping to the Hyperfine states which are non-resonant to the cavity mode.

We proceed in two steps. First, we limit the atomic structure to the $|F = 2\rangle$ and $|F' = 3\rangle$ states, including the Zeeman structure. We will show that in this picture, the atomic state diffuses in the Zeeman substructure. This diffusion process is characterised by a set of depumping rates which we will evaluate for the different polarisations. When the steady state is reached, the system is equivalent to a two-level atom coupled to the cavity with an effective coupling rate depending on the polarisation. Then, we will consider the depumping to other Hyperfine states which occurs on longer timescales.

1.5.1 Zeeman diffusion and effective coupling

Let us first consider the atomic structure restricted to $|F=2\rangle$ and $F'=3$ levels. If an atom is excited to the $F'=3$ levels, it can only fall back to the $|F=2\rangle$ levels. In a first approximation, we can therefore consider that that the atomic state stays in the $|F=2\rangle$ and $F'=3$ multiplets. We shall now study this dynamics restricted to this closed subspace.

We denote a generic atom cavity state by a product state $|i;m_F;n\rangle$, where $|i\rangle$ is either $|g\rangle=|F=2\rangle$ or $|e\rangle=|F=3\rangle$. The coupling to the cavity mode of polarisation $\mathbf{e}=(e_-;e_0;e_+)$ can be written in terms of the transition strengths $c^2_{m_F\to m'_F}$ as

$$\hat{H}_{int}=g_m\sum_{m_F}\sum_{q=-1,0,1}c_{m_F\to m_F+q}e_q\hat{\sigma}\hat{a}^\dagger|m_F\rangle\langle m_F+q|+\text{ h.c.} \tag{1.50}$$

The maximum coupling g_m corresponds to the cycling transition for which $c=1$. The transition strengths for the other transitions are displayed on Fig. 1.9. The spontaneous emission is modelised by the Liouvillian

$$\mathcal{L}\rho=\sum_q C_q\,\rho\,C_q^\dagger-\frac{1}{2}\{\rho,C_q^\dagger C_q\}, \tag{1.51}$$

with the three collapse operators

$$C_q=\sum_{m'_F}\sqrt{2\gamma_{m'_F\to m'_F-q}}\hat{\sigma}|m'_F-q\rangle\langle m'_F|, \tag{1.52}$$

corresponding to the emission of a free space photon of polarisation $q=-1,0,1$ with a rate $2\gamma_{m'_F\to m'_F-q}$. This rate is related to the transition strengths by $\gamma_{m'_F\to m'_F-q}=\gamma c^2_{m'_F-q\to m'_F}$. The normalisation of the transition strengths was chosen such that $\sum_{m_F}c^2_{m_F\to m'_F}=1$ independently of m'_F, and the total decay rate of an excited atom is always 2γ.

The case of π-polarised light

We investigate first the case of π-polarised light, i.e. when the cavity field polarisation is parallel to the external magnetic field.

If we consider for example the state $|g\rangle=|F=2;m_F=0\rangle$ and π-polarised cavity light, it is coupled vertically via the cavity mode to the excited state $|e\rangle=|F'=3;m_F=0\rangle$. When a spontaneous photon is emitted, the atom falls back in one of the three possible states $|F=2;m_F=-1,0,1\rangle$.

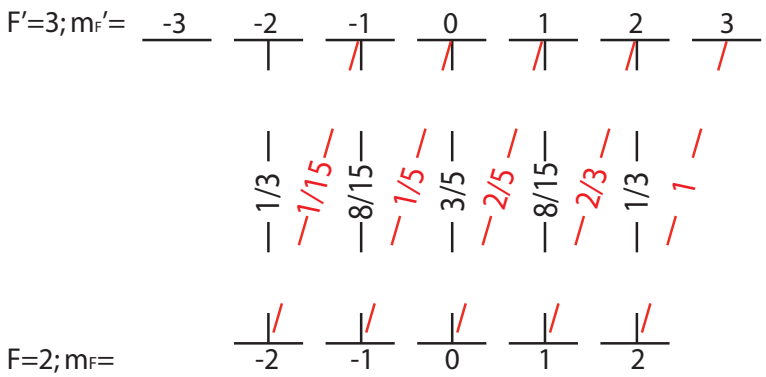

Figure 1.9: Transition strengths $c^2_{m_F \to m'_F}$ for π transitions (black lines) and σ^+ (red lines) between $|F = 2\rangle$ and $|F' = 3\rangle$ states of Rubidium 87. From [35].

The spontaneous emission process is incoherent, and the polarisation of the spontaneous photon indicates in which state the atom is. The coherences between general atom-cavity states with different m_F values therefore vanish. We can then write the density matrix of the system as a sum:

$$\rho = \sum_{m_F} \rho^{m_F} |m_F\rangle\langle m_F|. \tag{1.53}$$

In the following, we will derive a master equation for the reduced density matrices ρ^{m_F}. We will then be able to compute the steady state properties of the system, and connect them with the two-level picture. Finally, we will compute the depumping rates to the different Zeeman and hyperfine states which are relevant for the perturbation-free detection we want to achieve with the cavity.

Master equation for the reduced density matrices

In the first place, we take advantage from the "vertical" coupling to write the Hamiltonian as $\hat{H} = \sum_{m_F} |m_F\rangle\langle m_F|\hat{H}_{m_F}$ with

$$\hat{H}_{m_F} = -\Delta_a^{m_F}\hat{\sigma}^\dagger\hat{\sigma} - \Delta_c\hat{a}^\dagger\hat{a} + g_m c_{m_F\to m_F}(\hat{a}^\dagger\hat{\sigma} + \hat{a}\hat{\sigma}^\dagger) - i\eta(\hat{a} - \hat{a}^\dagger). \tag{1.54}$$

After some algebra, the master equations for the reduced density matrices read:

$$\frac{d\rho^{m_F}}{dt} = \tilde{\mathcal{L}}_{m_F}\rho^{m_F} + S^{m_F}, \tag{1.55}$$

where $\tilde{\mathcal{L}}_{m_F}$ is the Liouvillian for a two-level atom-cavity system, with a coupling g_{m_F}, an atomic decay rate γ and a cavity decay rate κ:

$$\tilde{\mathcal{L}}_{m_F}\rho = -i[\hat{H}_{m_F}, \rho] + \kappa\left(2\hat{a}\rho\hat{a}^\dagger - \{\hat{a}^\dagger\hat{a}, \rho\}\right) + \gamma\left(2\hat{\sigma}\rho\hat{\sigma}^\dagger - \{\hat{\sigma}^\dagger\hat{\sigma}, \rho\}\right). \quad (1.56)$$

and the source terms S^{m_F} arise from depumping induced by spontaneous emission from the other m_F states:

$$S^{m_F} = -2\gamma|g\rangle\langle g|\langle e|\rho^{m_F}|e\rangle + \sum_{m'_F} 2\gamma_{m'_F\to m_F}|g\rangle\langle g|\langle e|\rho^{m'_F}|e\rangle. \quad (1.57)$$

Approximate rate equations

In the set of master equations, the evolution due to the sources terms is slow compared to the evolution induced by the diagonal terms $\tilde{\mathcal{L}}_{m_F}$. We denote by $\tilde{\rho}_{ss}^{m_F}$ the steady state of this evolution: $\tilde{\mathcal{L}}_{m_F}\tilde{\rho}_{ss}^{m_F} = 0$, with $\mathrm{Tr}\tilde{\rho}_{ss}^{m_F} = 1$.

We can therefore apply a first-order perturbation theory, treating the source term as a perturbation. To the first order in γ/κ we have $\rho^{m_F} = \mathcal{P}^{m_F}\tilde{\rho}_{ss}^{m_F}$, where the $\mathcal{P}^{m_F}$ obey the rate equations (see App. A):

$$\frac{d\mathcal{P}^{m_F}}{dt} = \sum_{m'_F} \Gamma_{m'_F\to m_F}\mathcal{P}^{m'_F} - \Gamma_{m_F\to m'_F}\mathcal{P}^{m_F} \quad (1.58)$$

with the rates

$$\Gamma_{m'_F\to m_F} = 2\gamma_{m'_F\to m_F}\mathrm{Tr}\left(\tilde{\rho}_{ss}^{m_F}|g\rangle\langle g|\langle e|\tilde{\rho}_{ss}^{m'_F}|e\rangle\right) \quad (1.59)$$

$$\simeq 2\gamma_{m'_F\to m_F}\mathrm{Tr}\left(\langle e|\tilde{\rho}_{ss}^{m'_F}|e\rangle\right). \quad (1.60)$$

Steady state and effective coupling

The stationary populations in the different subspaces $\mathcal{P}_{ss}^{m_F}$ satisfy the normalisation condition $\sum_{m_F}\mathcal{P}_{ss}^{m_F} = 1$ and the equilibrium condition

$$\sum_{m'_F}\Gamma_{m_F\to m'_F}\mathcal{P}_{ss}^{m_F} = \sum_{m'_F}\Gamma_{m'_F\to m_F}\mathcal{P}_{ss}^{m'_F}. \quad (1.61)$$

The steady state is perfectly characterised by the knowledge of each density matrix $\tilde{\rho}_{ss}^{m_F}$, which can be computed either numerically, or using the weak excitation analytical expression. This allows then to compute the

depump rates $\Gamma_{m_F \to m'_F}$, and finally we solve the linear rates equations. For $g_m = 2\pi \times 210$ MHz, we find the steady state populations $\mathcal{P}_{ss}^0 = 51\%$, $\mathcal{P}_{ss}^{\pm 1} = 23\%$, $\mathcal{P}_{ss}^{\pm 2} = 1.5\%$. Neglecting the contribution of $m_F = \pm 2$ states, we furthermore observe that the transition strengths for π-transitions are very similar for $m_F = 0$ (0.77^2) and $m_F = \pm 1$ (0.73^2), leading to a maximum coupling of $g_0 \simeq 2\pi \times 160$ MHz. Therefore, all the properties of the system can then be computed directly in the two-level picture with this value of the coupling rate, for example the heating rate and the average cavity transmission. We have performed numerical simulations of the cavity transmission to verify this assertion.

Depumping dynamics

We now consider the following experimental situation: the single atom is initially in the $|F = 2; m_F = 0\rangle$ state and we switch on detection light. How long does it take to depump it to the other Zeeman levels? Can we detect the atom before this depumping occurs?

The dynamics of the system is characterised by the rate equations Eqn. 1.58, which we solve for typical experimental parameters on Fig. 1.10. The initial depumping rate is defined by

$$\Gamma_{depump}^{Z} = \frac{-d\mathcal{P}(m_F = 0)}{dt}. \tag{1.62}$$

For a reference power $n_0 = 2.5 \times 10^{-3}$, we obtain $\Gamma_{depump}^{Z} = 3.5$ kHz for the optimum detection parameters $\Delta_a = \Delta_c = 0$, assuming a perfectly localised atom at the position of maximum coupling.

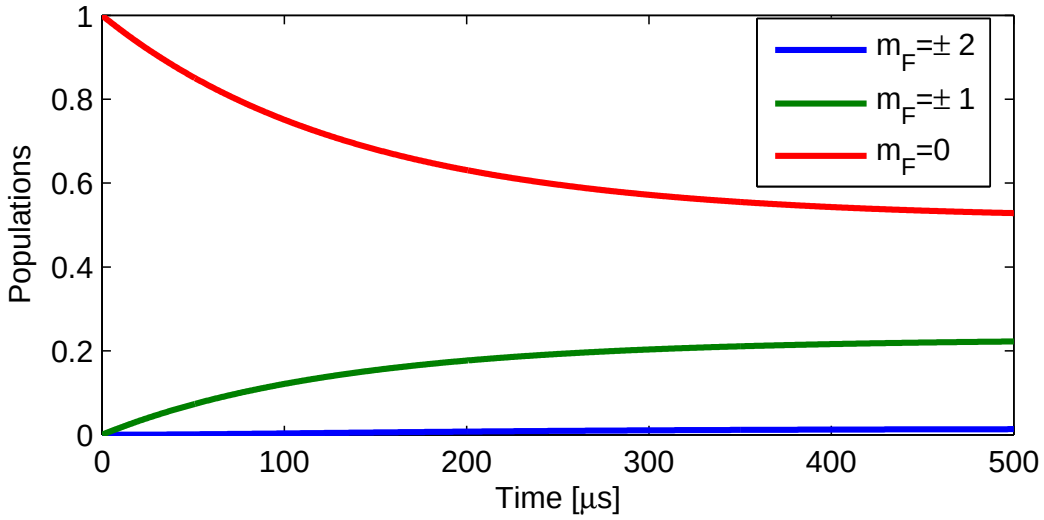

Figure 1.10: Solution to the rate equations for an atom initially prepared in $|F = 2; m_F = 0\rangle$. Parameters are: $n_0 = 2.5 \times 10^{-3}$, $g_m = 2\pi \times 210$ MHz, $\Delta_a = \Delta_c = 0$.

Other polarisations

The picture presented above only holds when the cavity polarisation is aligned with the magnetic field. Otherwise, we have to solve the atom-cavity problem taking into account the coupling to all possible states at the same time. As this cannot be done analytically, we turn to numerical simulations for the global density matrix ρ, which we can perform for arbitrary cavity field polarisation and magnetic field. We write the Liouvillian in the basis $|F;m_F\rangle$ for the atomic states, with a quantisation axis parallel to the magnetic field. Taking into account all atomic states $|F=2;m_F\rangle$ and $|F'=3;m_F\rangle$, and restricting the photon number to 0 and 1, the Liouvillian is a $24^2\times 24^2$ sparse matrix, with approximately 3600 nonvanishing terms. We did not consider the effect of the dipole trap light which mixes up all the m'_F states when the polarisation is not π. The steady state of the system can be computed, and we can extract the populations $\mathcal{P}^{m_F}$ of the different $|F=2;m_F\rangle$ states (see Fig. 1.11 Top), for different angles θ between cavity polarisation and magnetic field.

To estimate the depumping rate, we need to calculate the time evolution of the density matrix, which is computationally intensive. We therefore restrict ourselves to short evolutions. The depumping rate is found to depend quite strongly on the polarisation, and is minimum for $\theta=0$ (see Fig. 1.11 Bottom). The computed value at $\theta=0$ is in perfect agreement with the "analytical" solution presented in the previous section (3.5 kHz). The depumping rate is maximum at $\theta=\pi/2$, which corresponds also to the situation where the steady state population in $m_F=0$ is minimum. The depumping rate is then estimated at 15 kHz, for a magnetic field of 4G.

The steady state density matrix has very small coherence terms between different m_F ground states. We can therefore attempt to find an effective coupling g_{eff} to match the properties of the system with those of a two-level system. A natural candidate is chosen by analogy with the π-polarisation case:

$$g_{eff}=g_m\left(\sum_{m_F,q}\mathcal{P}_{ss}^{m_F}c^2_{m_F\rightarrow m'_F=q+m_F}e_q^2\right)^{1/2}, \tag{1.63}$$

where e_q is the component of the cavity polarisation in the $(\sigma^-;\pi;\sigma^+)$ basis. For $\theta=\pi/2$, we find $g_{eff}=0.7g_m$ and the system properties are globally in good agreement with the two-level picture in terms of cavity transmission and atomic excitation (thus spontaneous emission), see Fig. 1.12. The two-level approximation fails when the cavity and the probe are tuned close to the $|F=2;m_F=0\rangle\rightarrow|F'=3;m_F=0\rangle$ transition, as the probe field is now able to

selectively excite multiple, non-degenerate Zeeman states. The discrepancy is the largest at the exact resonance where the cavity transmission has a local maximum, whereas the two-level approximation predicts a minimum.

1.5.2 Depumping to other Hyperfine states

In the last section we have seen that in the multilevel picture reduces in many cases to a two-level picture, for the specific $|F = 2\rangle \rightarrow |F' = 3\rangle$ transition. We have seen that the Zeeman state of the atom changes very rapidly, with a timescale given by the spontaneous emission rate. However, all the possible states $|F = 2; m_F\rangle$ are coupled with the cavity (no dark states), and since the coupling g is always large compared to Zeeman splittings, the cavity transmission remains low as long as the atom is inside. The depumping to the Zeeman states is therefore not a limit to the observation of a single atom when it is trapped independently of its m_F state. This is the case in a dipole trap, but not in a pure magnetic trap where only states with $m_F > 0$ are trapped. In a dipole trap, the limitation to the observation time (besides the heating rate) is due by the depumping the other hyperfine state $|F = 1\rangle$. This process involves necessary a transition via the non-resonant state $|F' = 2\rangle$, followed by a spontaneous emission since the cavity is too far off resonance with respect to the $|F = 1\rangle \rightarrow |F' = 2\rangle$ transition. Furthermore, the symmetry of the dipole operator implies that an atom in the $|F' = 2; m'_F\rangle$ states decays with *equal* probability to the $|F = 1\rangle$ and to the $|F = 2\rangle$ states [35]. As a consequence, the depumping rate to the $|F = 1\rangle$ state is simply given by

$$\Gamma^{HF}_{depump} = \gamma \mathrm{Tr}(\rho |F' = 2\rangle\langle F' = 2|). \tag{1.64}$$

The density matrix ρ has to be computed with an atomic structure including states $|F = 2; m_F\rangle$, $|F' = 2; m'_F\rangle$ and $|F' = 3; m'_F\rangle$. The dynamics in this subspace is very fast compared to the depumping rate Γ^{HF}_{depump}, so we just need to know the steady state ρ_{ss}. The calculation is done in a similar fashion as in Sect. 1.5.1. The depumping rate is displayed on Fig. 1.13 for various values of the detuning Δ_a and coupling g_m, with $n_0 = 2.5\times10^{-2}$ and π-polarisation[6]. We find that the depumping rate is the largest on the red detuning side, since we get more resonant to the transition $|F = 2\rangle \rightarrow |F' = 2\rangle$ which depumps efficiently to $|F = 1\rangle$. With a blue detuning, the depumping rate is in the kHz range, and gets smaller as the coupling increase. The depumping rate is minimum near resonance, with a value of the order of 0.1 kHz.

[6] Compared to depumping in the Zeeman states described previously, we choose a larger value for n_0 since hyperfine depumping process is much slower. This also corresponds better to the experimental settings of Sect. 4.4.2.

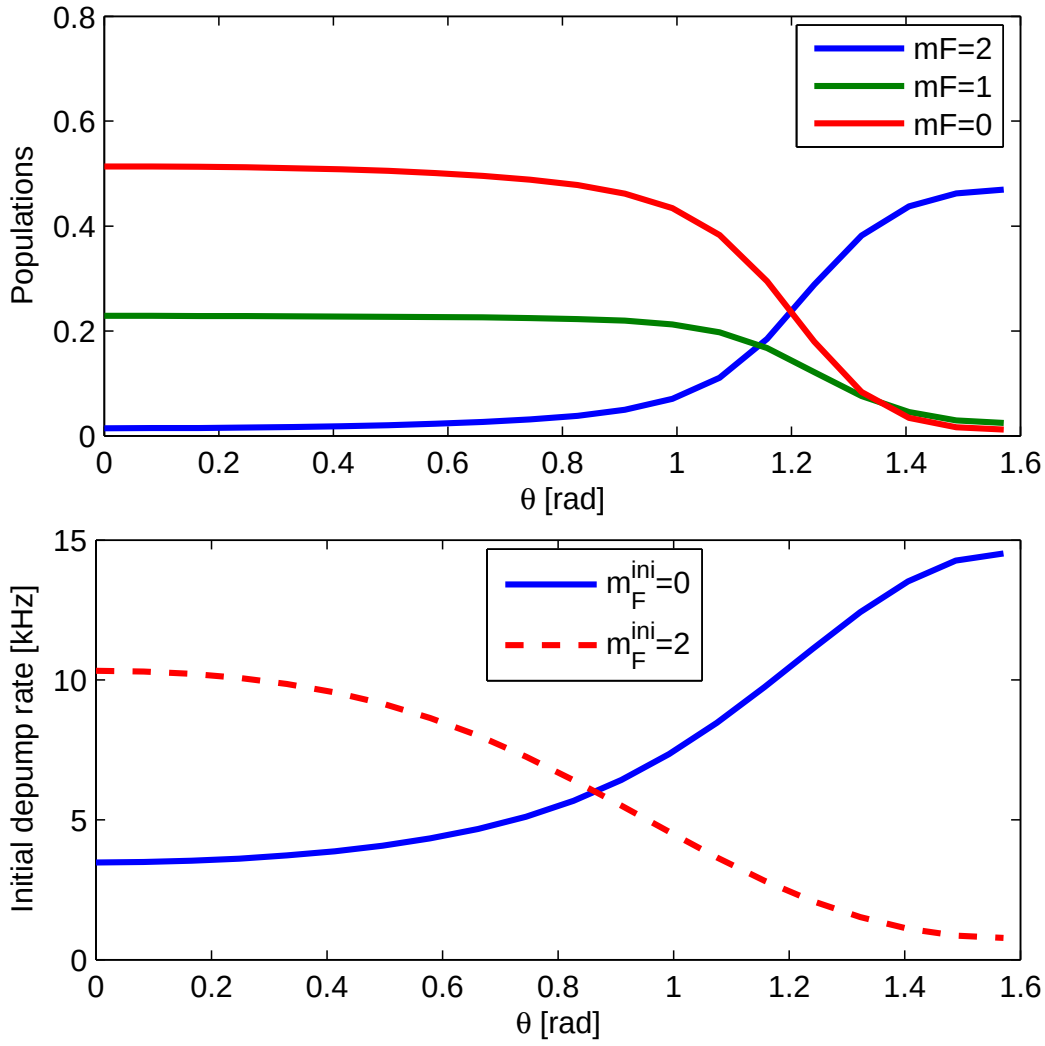

Figure 1.11: Numerical simulations of atom-cavity system with arbitrary polarisation. Common parameters are $n_0 = 2.5 \times 10^{-3}$, $|B| = 4G$, $g_m = 2\pi \times 210$ MHz.
Top: Population in the different levels $|F = 2; m_F\rangle$ at steady state, versus the angle θ between polarisation and magnetic field. The quantisation axis is the magnetic field direction.
Bottom: Initial depumping rate from the $|F = 2; m_F = 0\rangle$ state (blue) and from the $|F = 2; m_F = 2\rangle$ state (red, dashed).

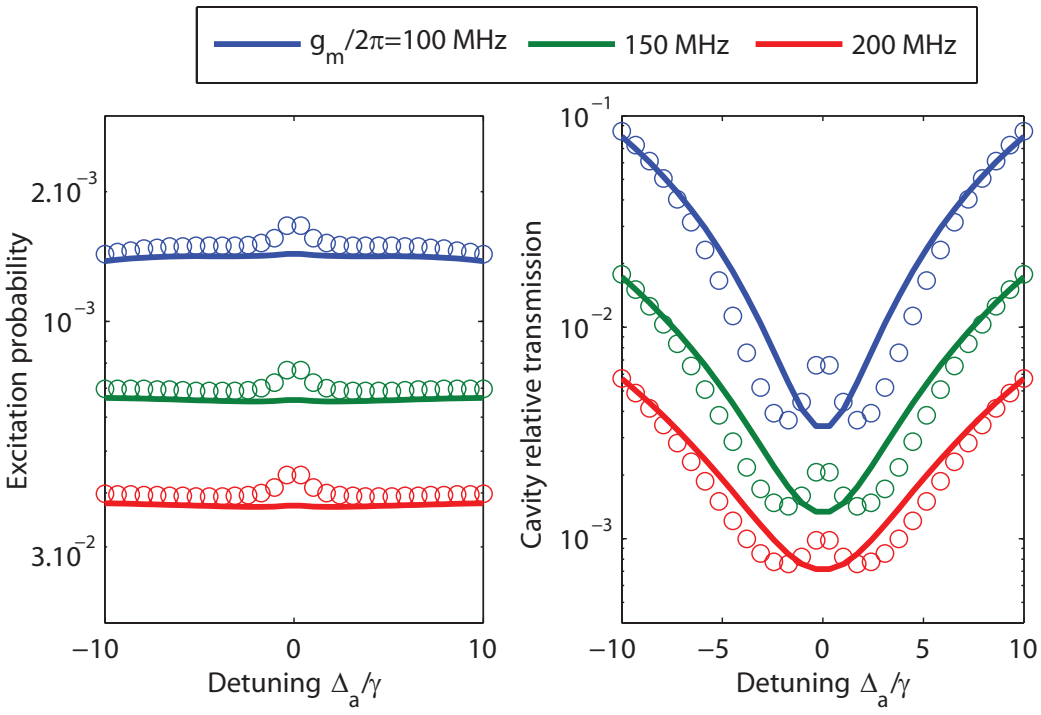

Figure 1.12: Accuracy of the effective coupling picture. We computed the atomic excitation (Left) and the cavity transmission (Right) for different couplings g_m (colours), using the steady state solution to the master equation (circles) or the effective two-level picture (lines). We took $\theta = \pi/2, |B| = 4G$, $n_0 = 2.5 \times 10^{-3}$ and $g_{eff} = 0.7 g_m$.

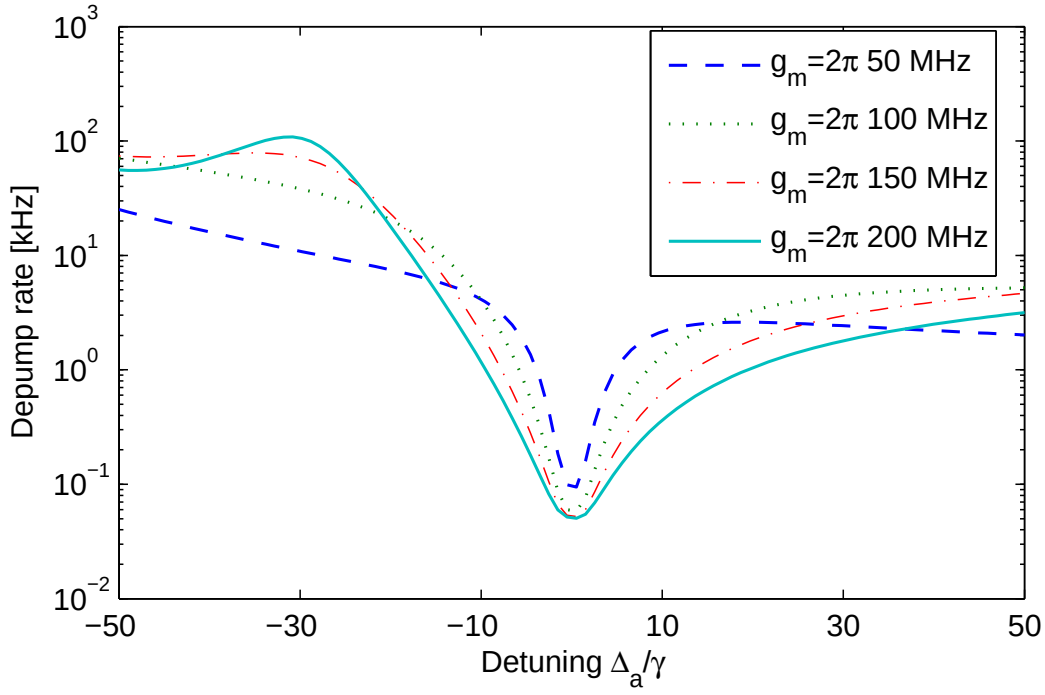

Figure 1.13: Depumping rate to the Hyperfine $F = 1$ level, for different values of the coupling g_m and the probe-atom detuning Δ_a. The cavity is pumped on resonance ($\Delta_c = 0$), with a reference number of intracavity photons $n_0 = 2.5 \times 10^{-2}$. The cavity polarisation is π.

1.6 Conclusion

Let us summarise the results obtained in this chapter. We have shown that a resonant cavity can be used as a detector of single atoms, or to measure a single atom hyperfine number F. Compared to a free space detection, the cavity detection scheme induces much less spontaneous emission, thereby allowing a better detection efficiency before the atom is lost. We have characterised the three possible processes which limit the measurement time of a single atom in the experiment: heating due to light forces fluctuations, depumping to the Zeeman states, and depumping to the Hyperfine states. The Zeeman depumping is the fastest process, but does not limit the observation of atoms that are trapped in a dipole trap, since the system can be accurately described by an effective coupling rate including Zeeman depumping. The measurement time of trapped single atoms is ultimately limited by the Hyperfine depumping since heating effect can be made irrelevant by using a deep trap.

Chapter 2

Experimental setup

The present chapter is devoted to the description of the experimental apparatus, used to perform all the experiments described in this thesis.

The core of the apparatus is the atomchip, used for the manipulation of cold atoms with magnetic fields. On top on the atomchip is mounted a Fabry-Perot cavity used for single atom detection. The cavity is made from two optical fibres facing each other, with their tips processed for high reflectivity and large curvatures to form a stable, high-finesse optical cavity, together with a small mode volume. The chip and the cavity are located in a ultra-high-vacuum chamber. Optical systems provide the various light beams required for laser cooling, and also to inject the cavity and stabilise its length. The transmission of the cavity is measured with an avalanche photodiode (APD). Constant bias fields are generated by coils located around the glass cell, and radiofrequency and microwave fields are coupled to the atoms via antennas. DC currents running in the coils and in the chip wires are provided by low noise current sources, while the rf and mw have specific sources. Of course, almost all this equipment is controlled by a computer interface.

Most of this experimental apparatus was built during the thesis of my predecessor Tilo Steinmetz, and is fully described in his thesis [44]. It has been now running continuously was about 4 years, and has suffered no apparent ageing. In particular, the finesse of the cavity did not drop, the quality of the vacuum remained good enough for BEC. The intrinsic capabilities of the system turned out to be large enough to require no major changes of the setup during the last 4 years. In this chapter, we will give anyway a complete picture of the system, but focus only on the changes we have performed during my thesis. They include a new design for the cavity stabilisation and dipole trap, an addition of a microwave system to drive hyperfine transitions of single atoms, and a microcontroller-based interface to enable real-time control of the experiment in the critical phase of single atom preparation.

The chapter is split in different sections corresponding to the building blocks of the experiment. The first section will be devoted to the cold atoms setup. The second section concerns the high-finesse cavity, and we shall insist here on the stabilisation system and the characterisation of the intracavity dipole trap. The microwave source and its characterisation is the object of the third section. Finally, we will describe the experimental interface in the fourth section.

2.1 Setup for cold atoms

We describe in this section a typical atomchip setup to obtain a Bose-Einstein condensate. It includes the descriptions of the vacuum system, of the optical system for laser cooling and of the atomchip used for magnetic trapping. We will conclude it by explaining a typical sequence to obtain a BEC.

2.1.1 Vacuum cell and external coils

The vacuum chamber ($p < 10^{-9}$ mbar) is terminated by a glass cell in its upper part, while the pump system is located in the bottom of the chamber. The atomchip is in fact the ceiling of the cell. The schematic of the vacuum cell, along with the connection to the vacuum chamber, is depicted on Fig. 2.1.

The vacuum cell[1] has a cubic shape (inner dimension: 30 mm, outer 35 mm). It is closed at the top by the atom chip, and connected at the bottom to a glass/metal transition[2] via a circular hole of diameter 27 mm. The vacuum seal is ensured at both locations by vacuum and high temperature compatible epoxy glue[3]. The vacuum chamber is pumped by a Ion-getter pump[4], while a Ti-sublimation pump is also present but not used since the vacuum is good enough with the ion pump alone. At the bottom of the chamber ($\sim$ 30 cm below the cell) are located two Rubidium dispensers[5], one of which we operate continuously at approximately $I = 3.3A$ when the experiment is running, the other one being here for redundancy. The quality of the vacuum is characterised by the lifetime in the magnetic trap ($\sim$ 1.4s). A compromise has to be reached between the number of atoms is the MOT (increases with the ^{87}Rb pressure as p_{Rb}) and the lifetime in magnetic trap

[1] Hellma 704.001-OG, with externally AR coated windows.
[2] Caburn DN40CF
[3] Epotek 353ND.
[4] Meca2000 25L/s.
[5] SAES RB-NF-3.4-12FT10+10

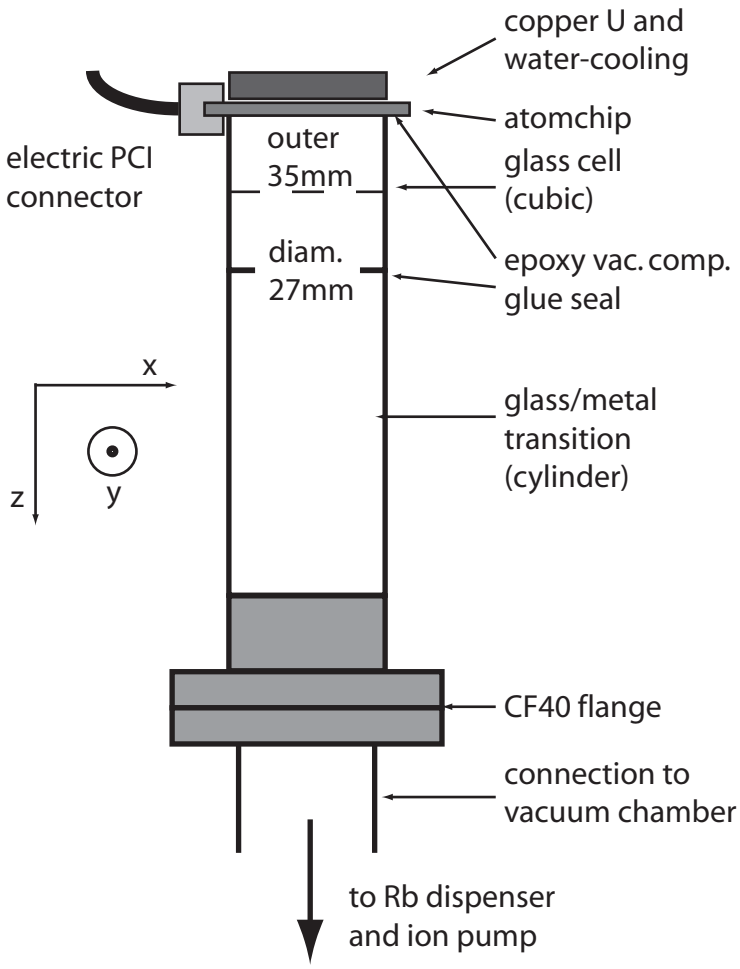

Figure 2.1: Schematic of the vacuum cell. Electric connections to the chip on the right side is not depicted. The z-axis is along gravity.

(decreases as $1/(p_{Rb}+p_{other})$). The figure of merit is typically the number of atoms we can get in the BEC at the final trap location.

The vacuum cell is enclosed by 4 sets of coils pairs. The coils are rectangular and of typical dimensions of 6 to 10 cm. Three pairs - one for each axis x,y,z - are in Helmholtz configuration to generate uniform magnetic bias fields up to 60G. One pair is in anti-Helmholtz configuration to generate a magnetic field gradient in the x-direction. Above the atomchip is glued a thick (2mm) U-shaped piece of copper to generate a quadrupole magnetic field for the MOT phase. The heat generated during the MOT phase, along with the heat generated by the atomchip during the rest of the experiment,

is collected by a copper block of approximately 1 cm thickness, in which a water-cooling circuit runs constantly. The heat flow between the chip and the U, on the one side, and the water-cooled piece of copper on the other side, is controlled by a Peltier element placed in between to suppress the long term drift of the chip temperature. Temperature regulation is crucial for the experiment as the cavity length drifts due to the thermal expansion of the mount.

2.1.2 Optical system for cold atoms

We shall describe here our optical setup for the production of cold atoms. The glass cell provides optical access for several light beams used for laser cooling, optical pumping and absorption imaging. These light beams are derived from a laser system consisting in several laser-diodes at 780nm. The basic requirements are the same for all ^{87}Rb experiments which operate the laser cooling on the D2 transition ($\lambda = 780nm$). The level structure imposes the use of several laser beams: MOT beams (or cooling beams), repumper beam, pump beam and imaging beam (see Fig. 2.2).

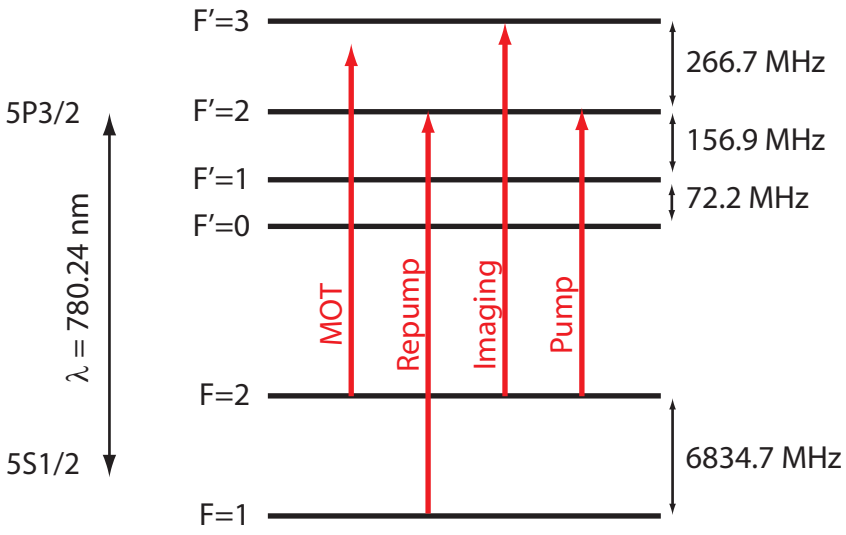

Figure 2.2: Hyperfine level structure of ^{87}Rb and position of the various beams

The laser cooling procedure requires six beams (MOT beams) propagating in all directions of space and crossing at the position of the zero of the magnetic field during the MOT phase. For the molasses phase, in which the magnetic field in zeroed, the polarisations of the 6 beams have to be circular

and the same[6] (here σ^-) for the Sisyphus cooling to operate. The cooling light is slightly red detuned to the cyclic transition $F = 2 \rightarrow F' = 3$, by 5γ in the early MOT phase to 30 γ in the molasses phase. During the MOT, the atoms might get depumped to the $|F = 1\rangle$ "dark" state, so we use a repumper beam on the $F = 1 \rightarrow F' = 2$ transition to pump them back to $|F = 2\rangle$. After the molasses, and before the transfer to the magnetic trap, the atoms are pumped to the extreme state $|F = 2; m_F = 2\rangle$ by a pump beam for which $|F = 2; m_F = 2\rangle$ is a dark state: therefore this beam has to be σ^+ polarised[7], and tuned to the $|F = 2\rangle \rightarrow |F' = 2\rangle$ transition. Finally, we will detect the atoms on the cycling transition $|F = 2; m_F = 2\rangle \rightarrow |F' = 3; m'_F = 3\rangle$, which requires one more σ^+ beam. This one has to be tuned exactly on the Zeeman-shifted transition to ensure the absorption is maximum and to remove dispersion effects which lead to image aberrations.

Laser system for cold atoms production

We describe here the laser system developed to obtain all these beams. The workhorse of the laser system is a customary diode-laser operating at 780 nm, mounted an an external cavity configuration to decrease the natural linewidth. The external cavity is formed by the endfacet of the laser diode[8] and a grating with reflects the -1 order back to the diode (Littrow configuration). The angle of the grating is actuated by a piezo with allows precise wavelength tuning. We use two copies of this system, plus one without the external cavity. The first one ("master laser") is locked to the crossover between the $|F = 2\rangle \rightarrow |F' = 2\rangle$ and $|F = 2\rangle \rightarrow |F' = 3\rangle$ transitions. The lock is obtained by means of saturated absorption spectroscopy, with a RF-modulation of the laser diode current, and the correction signal is fed to the piezo controlling the grating angle. From this laser we derive two lines: one line is frequency-shifted with an acousto-optic modulator (AOM) used in double-pass "cat's eye" configuration, to obtain the pump beam. The second line is frequency-shifted by another cat's eye AOM, before injecting a second laser. The second laser (which has no external cavity) is again split in two lines, from which we obtain the MOT beams, and the imaging beam, using here again two AOMs to frequency-shift the lines and provide short switching times. A third laser is locked on the crossover between $|F = 1\rangle \rightarrow |F' = 1\rangle$

[6] From the optical point of view. From the atomic point of view, the polarisations of a given pair of counterpropagating beams are σ^+ and σ^- if the quantisation axis is taken along the propagation axis of one of the two beams.

[7] Here from the point of view of the atoms, which requires the magnetic field to be parallel and in the same direction as the propagation of the pump beam.

[8] Sharp GH781JA2C (discontinued).

and $|F = 1\rangle \rightarrow |F' = 2\rangle$ transitions, then frequency-shifted with an AOM to obtain the repumper beam. All these different beams can be switched on and off by way of home-built mechanical shutters made from high power mechanical electric switches and pieces of still-camera diaphragms.

Optics around the cell

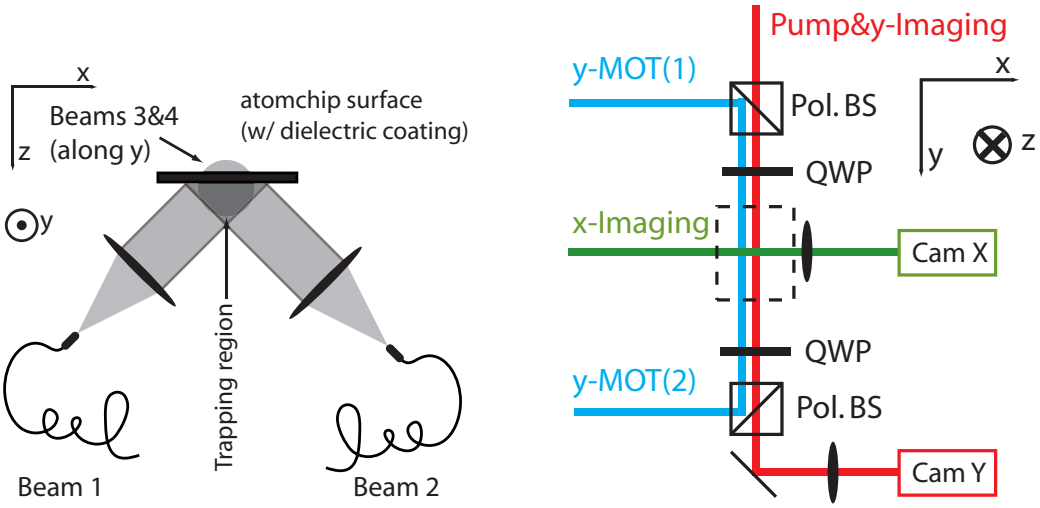

Figure 2.3: Schematic of the various beams around the cell.
Left: Side view of the MOT beams. The darkest zone corresponds to the crossing zone of the 6 effective beams, thus to the cooling zone.
Right: Top view of the other beams. The chip position is marked with dashed lines. The beams are separated for clarity. QWP= quarter-wave-plate, Pol. BS= polarising beam-splitter.

Light produced as explained above is brought near the vacuum cell by means of polarisation maintaining single mode fibres, then expanded with lenses. Using waveplates, we can then achieve the desired polarisation for each beam. Let's start with the MOT beams. A MOT requires usually 6 beams, one for each direction of space. Due to the presence of the chip, it is however not possible to send light along the vertical axis. The mirror-MOT technique was developed in the early chip experiment to circumvent the problem. It relies on the reflection on the chip surface to obtain 6 effective beams from only 4 (see Fig. 2.3 Left). The reflected beams are tilted by 45°, and are slightly more powerful than the non-reflected ones. One of the two 45° beams share its fibre with the repumper beam. The other beams lie in

the horizontal plane (see Fig. 2.3 Right). We use two imaging beams, along with two cameras[9] for imaging in the x and y direction. The x beam is tilted by approximately 30 ° to avoid the electric connectors located on both sides of the chip. Details about the lenses system can be found in [44, p. 50].

2.1.3 Chip and magnetic traps

In an inhomogeneous magnetic field, atoms feel a potential $U = -\mu B$ where μ is the magnetic moment. For atoms in the low-field seeking states ($\mu < 0$), the atoms can be trapped at a minimum of the magnetic field. The trapping frequency will be proportional to the curvature of the magnetic field at its minimum. For ^{87}Rb atoms in the 5S1/2 multiplet, the trappable states are $|F = 2; m_F = 1, 2\rangle$ and $|F = 1; m_F = -1\rangle$. Magnetic potentials may be generated by coils, but advanced manipulations typically require several tunable traps and as many coils. Furthermore, the further the coil is away from the atom, the weaker the confinement it can provide. The technology of atom chips was developed to overcome this limitations, and greatly simplify cold atoms setups. The requirement on the quality of the vacuum decrease as the manipulation time decreases, and with a stronger confinement, one can typically obtain a Bose-Einstein condensate in less than 10 seconds. The principle of the atomchip is a bidimensional structure of wires, in which one can run currents to create magnetic potentials. If the chip is close to the trapping zone, the confinement obtained is stronger. Typically, the chip is put directly in the vacuum chamber, or is part of it as it is the case in our experiment. The distance between the trap centre and the chip surface can be made as small as 10 μm or so. The chip technology was extended to realize more general potentials, like rf potentials [20] or mw potentials [45].

The atomchip used in this experiment consists in a bidimensional structure of gold wires deposited on a insulating substrate of Al-N. It was fabricated at the LMU in Munich, using microlithography techniques. Details about the chip fabrication process can be found in [46], where they used the same recipe for chip fabrication. With current microlithography techniques, micrometre-thick wires can be realized, and hundreds of them can be combined on the same chip, using multiple layers if necessary. There is almost no limitation to the variety of traps one can obtain by combining currents in the different wires, see for example [47, 48] for an overview. The trap parameters can be computed by solving the Biot-Savard equations. We shall however give here the physical insight which guides the user to design a trap. Consider a single wire (orientated along x) in which we drive a current I_x. The magnetic

[9] JAI-CV-M50-IR.

field is given by $\mathbf{B} = \mu_0 I/(2\pi r)\mathbf{e}_\theta$, in the cylindrical coordinates of axis x. If we add an external uniform bias field $\mathbf{B}^{ext} = B_x^{ext}\mathbf{e}_x + \mathbf{B}_\perp^{ext}$, the perpendicular component compensates the wire field along one line, parallel to the x-axis, at a distance $r_0 = \mu_0 I/(2\pi B_\perp^{ext})$, where the resulting magnetic field magnitude is minimum. A single wire combined to a magnetic bias field therefore realizes already a 2D trap or "waveguide". The trap curvature is the same in both transverse directions, and is given by $B''_\perp = (B_\perp^{ext})^2/(|B_x^{ext}|r_0^2)$. Most traps are variations to this waveguide trap, done by adding a confinement (generally weaker) in the third direction.

The chip used here has 48 independent connectors, and features wires with a width down to 50μm. It is made with two layers, the bottom layer being used only for a single phase of the experiment, the upper layer has the smallest wires and is depicted on Fig. 2.4. The connectors to the current sources are located on the left and the right side of the lower layer. The connection between the layers is provided by small bonding wires.

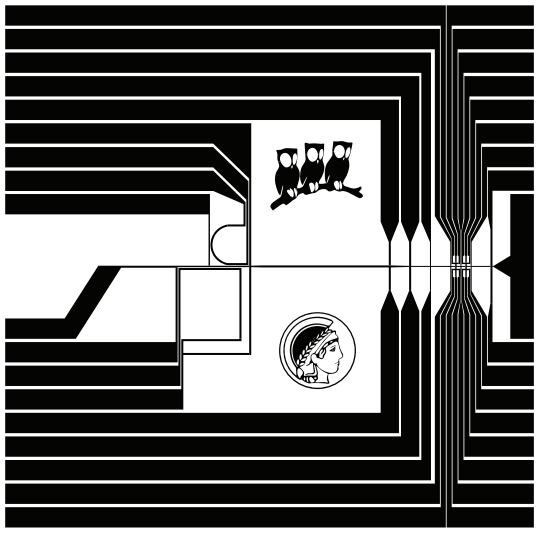

Figure 2.4: Bottom view of the chip upper layer. The dimensions are 25×28 mm.

As an example of a trap we realize during the experiment, other than the waveguide, we consider the trap generated by the P-shape structure Fig. 2.5. If the external magnetic field is directed along x, it compensates the P field at the position marked in blue on the left figure, where the wire is directed towards $-y$. Therefore, the P wire is locally equivalent to a straight wire

directed along y, and the confinement is strong in the x and z directions. If we rotate the magnetic field, the position of the trap also rotates, which allows us to bring the atoms near the waveguide line depicted in green on the right figure.

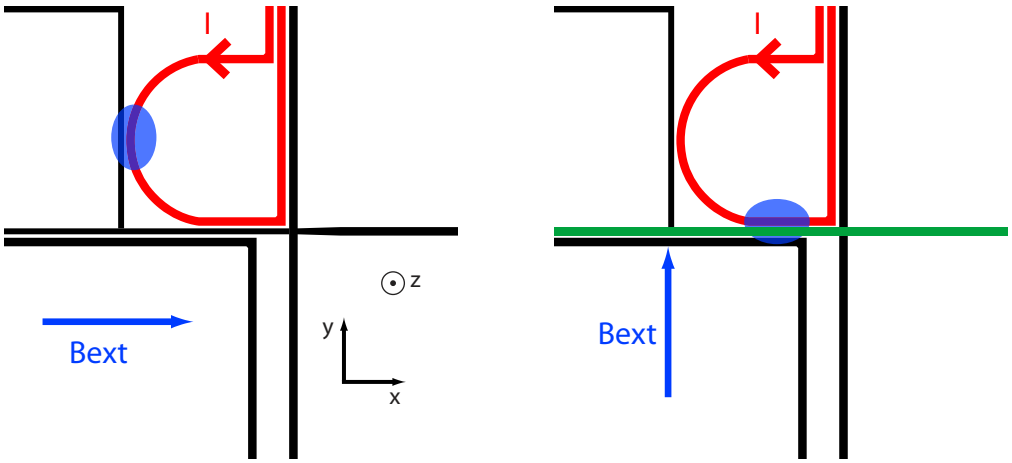

Figure 2.5: Geometry of the rotatable P-Trap. The position of the cloud is depicted in blue.

2.1.4 From the MOT to the BEC

A typical experimental sequence for cold atoms starts with a MOT, obtained by switching on the current in the quadrupole U and applying cooling light and repumper light during approximately 5 seconds. Then comes the molasses phase: the quadrupole field is switched off and cooling light is applied for a brief period (typ. 3 ms). The mechanism of Sisyphus cooling allows here to obtain an ultracold atomic cloud, with a typical atom number of 40×10^6 and a temperature of 14μK. At this point, we apply a short pulse of pump light to optically pump the atoms to the magnetically trappable state $|F = 2; m_F = 2\rangle$. We are then able to transfer the cloud to a first magnetic trap generated by the P-structure as explained above. The atoms are then transferred to a series of different magnetic traps, to reach to position where we want to manipulate them. For each transfer to a different trap, the currents in the chip wires and the magnetic bias field are ramped from an initial to a final value. Bose-Einstein condensation is only performed at the final trap, because the BEC is sensitive to heating and survives for approximately 100 ms. To reach BEC, we apply a radiofrequency ramp on a

typical timescale of 1s or less, depending on the final trap frequencies. The larger the confinement, the shorter the ramp. We routinely obtain quasi-pure BEC with approximately 1,000 atoms. This is the starting point for our experiments.

2.2 High finesse Fabry-Perot cavity

The Fabry-Perot cavity used in this work for single atom detection is made from two optical fibres facing each other[10]. The endfacets of the fibres are processed for high reflectivity, which yields a large finesse of 36,000.

Used in combination with atom chips, these fibre-based Fabry-Perot (FFP) cavity have strong advantages over standard, macroscopic high-finesse Fabry-Perot cavities:

- The cavity length, of the order of 40 μm is small, which allows to use strongly-curved mirrors while staying in the stability range of the cavity. Therefore the mode-waist ($\sim 4\mu$m here) is small, and the strong coupling regime can be reached without requiring a very large finesse. As a result, the condition for cavity stabilisation are less stringent compared to longer cavities.

- The cavity mode is very close to the surface of the chip ($\sim 150\mu$m here), which allows a stronger confinement with magnetic traps, and good control of the atomic position. For instance, it is possible to load atoms in a single antinode of the cavity mode [15].

- The system is scalable. In the experiment we have two cavities (we only use one for the moment), but it is in principle possible to use as many as desired with the same atom chip.

And compared to other kind of resonators such as photonic crystal cavities, or microspheres and microtoroids, it is still easier to bring the atoms in the cavity mode, although these designs have certainly a strong advantage in terms of scalability and integration to a chip.

The fabrication process consists in two steps. In the first step, the fibre tips are shaped to form a concave surface by means of CO2 laser ablation. This process is described in [49, 50]. This allows to reach radii of curvature in the 100-500μm range, while enabling a smooth surface on the fibre tips. In our experiment the radii of curvature are $R_1 = 450\mu$m, $R_2 = 150\mu$m. Then, the fibre tips are coated with a HR coating[11]. The coatings have a specified transmission $T = 31$ ppm and loss $L = 56$ ppm at 780 nm. Each fibre is glued

[10]The input fibre is a single-mode fiber with mode field diameter matching the cavity mode diameter at the mirror position. The output fibre is a multimode fibre in order to loosen the alignment constraints for efficient output light collection. More details about alignment procedure can be found in [44].

[11]LZH Hannover: the fibres are directly coated there, there is no transfer process.

in a V-groove holder, mounted on a shear piezo[12], which allows to tune the cavity length by approximately 1μm. It is therefore always possible to find a TEM00 resonance within the actuation range. The piezos are mounted on a ceramic bridge. The alignment of the cavity is done on the ceramic bridge, before it is glued on the atomchip (see Fig. 2.6). The input fibre of the cavity is a single mode, non-polarisation maintaining fibre, while the output fibre is a multimode one. With a multimode fibre at the output, the requirements for the alignment procedure are weaker. There is no further adjustment to do later on, excepted the cavity length. The thickness of the bridge is chosen to have a minimum distance between the chip surface the cavity mode axis, 150μm in our experiment.

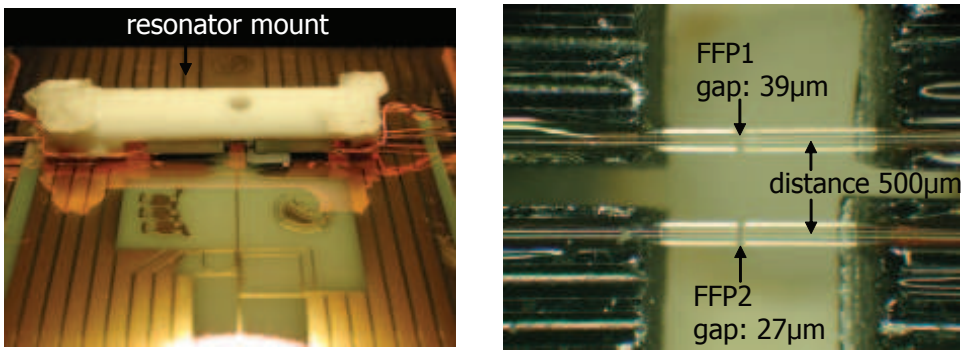

Figure 2.6: Photographs of the integrated atom-cavity setup. The right picture is a zoom of the two fibre-cavities.

2.2.1 Length stabilisation

In this section we describe the stabilisation scheme of the cavity length.

Principle

The cavity stabilisation is realized with the help of a second resonance line at 830 nm. The double resonance condition at 780 nm and 830 nm for the

[12]PI-Ceramic shear plate, dimension 5 mm(active)×5 mm×1 mm.

TEM00 mode can be written in the equivalents forms:

$$\left\{ \begin{array}{rcl} \omega_{780} & = & n_{780} 2\pi c/L_{780} \\ \omega_{830} & = & n_{830} 2\pi c/L_{830} \end{array} \right. \text{ or } \left\{ \begin{array}{rcl} \lambda_{780} & = & L_{780}/n_{780} \\ \lambda_{830} & = & L_{830}/n_{830} \end{array} \right. , \tag{2.1}$$

where $L_{780,830} \simeq 2d$ are the cavity "effective" lengths at 780nm and 830nm, including mirror phase shifts, and which we assume to be almost the same. An approximate value for the effective lengths comes from the measurement of the FSR which gives $L \simeq 78\mu$m. The mode number for a wavelength of 780 nm is then $n_{780} \simeq 100$. From the equations Eqn. 2.1 we extract the mode number for light at 830 nm: $n_{830} - n_{780} \simeq L(1/\lambda_{830} - 1/\lambda_{780}) \simeq -6.02$, but from the integerness of n, we can conclude that

$$n_{830} = n_{780} - 6. \tag{2.2}$$

The two modes having the same parity, they coincide in the centre of the cavity, in agreement with the observations [15]. For a cavity locked to a spectroscopy-stabilised laser at $\lambda = 780.24$ nm, the measurement of the 830nm wavelength with a 6-digit wavelength-metre[13] yields $\lambda_{830} = 830.10$ nm. Using the exact equation $n_{830} - n_{780} = -6$, we compute the cavity effective lengths L_{780} and L_{830} for different guesses of n_{780} around 100. The difference $|L_{780} - L_{830}|$ has a clear minimum for $n_{780} = 100$, a strong indication for this value of the mode number[14]. We finally extract the cavity effective lengths at 780 nm and 830 nm: $L_{780} = 78.024\mu$m and $L_{830} = 78.029\mu$m. The difference of 5 nm can be explained by the properties of the coatings which are optimised for 780 nm.

This preliminary work done, we now proceed to the locking scheme. The goal is to fix the position of the 780 nm resonance at a desired value $\omega_{c,780} = \omega_a + \Delta$, without sending light at this frequency. Instead, we want to use 830 nm to lock the cavity, but the precise value of the wavelength cannot be controlled with a high precision, because there are no spectroscopic references at 830.10 nm.

For that matter, we derive two other beams at 780 nm (the 780' beam) and 830 nm (the 830' beam) which are frequency-shifted from the 830 nm of the FFP cavity (830 beam) and a spectroscopy-stabilised reference laser at 780 nm (which we assume here for simplicity being exactly at the atomic resonance ω_a): $\omega'_{780} = \omega_a + \Delta_{aux}$, $\omega'_{830} = \omega_{830} + \Delta_{830}$. Then, we use a second Fabry-Perot cavity of length L' (transfer cavity) to transfer the frequency accuracy of the spectroscopy-stabilised 780 nm light to the 830 nm light. We

[13] High-Finesse WS6, courtesy of F. Gerbier team.

[14] This value differs from [44].

inject both the 780' and the 830' beams in this transfer cavity. We now write the double resonance condition for the transfer cavity with a free spectral range denoted by $\mathrm{FSR}' = 2\pi c/L'$:

$$\begin{cases} \omega'_{780} &= n'_{780}\mathrm{FSR}' \\ \omega'_{830} &= n'_{830}\mathrm{FSR}' \end{cases} \tag{2.3}$$

Enforcing now the lock condition $\omega_{830} = n_{830}\mathrm{FSR}$, we now find the position of the 780 nm resonance for the FFP cavity

$$\omega_c = \frac{n_{780}n'_{830}}{n_{830}n'_{780}}\omega_a - \frac{\lambda_{830}}{\lambda_{780}}\Delta_{830} + \Delta_{aux} = \omega_a + \Delta_0 + \Delta_{aux} \tag{2.4}$$

where the coefficient "1" in front of Δ_{aux} is precise to 10^{-6} when we limit the detunings Δ to <1 GHz. We can therefore scan the cavity resonance, by scanning the value of Δ_{aux}, while keeping Δ_{830} constant and the resonance condition enforced. The value of the initial detuning depends on the mode numbers $n'_{780,830}$ and has to be calibrated by looking at the cavity transmission. It changed from one double resonance $(n'_{780}; n'_{830})$ to the next $(n'_{780}+1; n'_{830}+1)$ by an amount $\delta(\Delta_0) = \mathrm{FSR}'(\frac{n_{780}}{n_{830}} - 1) = \frac{3}{47}\mathrm{FSR}'$. Equivalently, we obtain the same detuning on the FFP cavity if we change at the same time the value of Δ_{aux} by an amount $\delta(\Delta_{aux}) = \mathrm{FSR}'(1 - \frac{n_{780}}{n_{830}})$. The resonance condition $\omega_c = \omega_a$ can therefore be only for a finite set of values of Δ_{aux} which allows us to identify to mode number n'_{780}.

$$\Delta_{aux}(k) = \Delta^0_{aux} + k\mathrm{FSR}'(1 - \frac{n_{780}}{n_{830}}) \tag{2.5}$$

where $k \in Z$.

Experimentally, we proceed the following way: the detuning Δ_{830} is set to a reference value which is always the same. The 830 laser is approximately tuned to be obtain a double resonance on the FFP cavity. Then we scan the transfer cavity and tune Δ_{aux} to obtain a double resonance also on the transfer cavity. The value of Δ_{aux} is then compared to the possible values, and then locked to the closest one. Similarly as with the FFP cavity, the position of the double resonance allows to identify on which modes the transfer cavity is locked.

Implementation

Let us now discuss the implementation, which corresponds approximately to the upper half of Fig. 2.7.

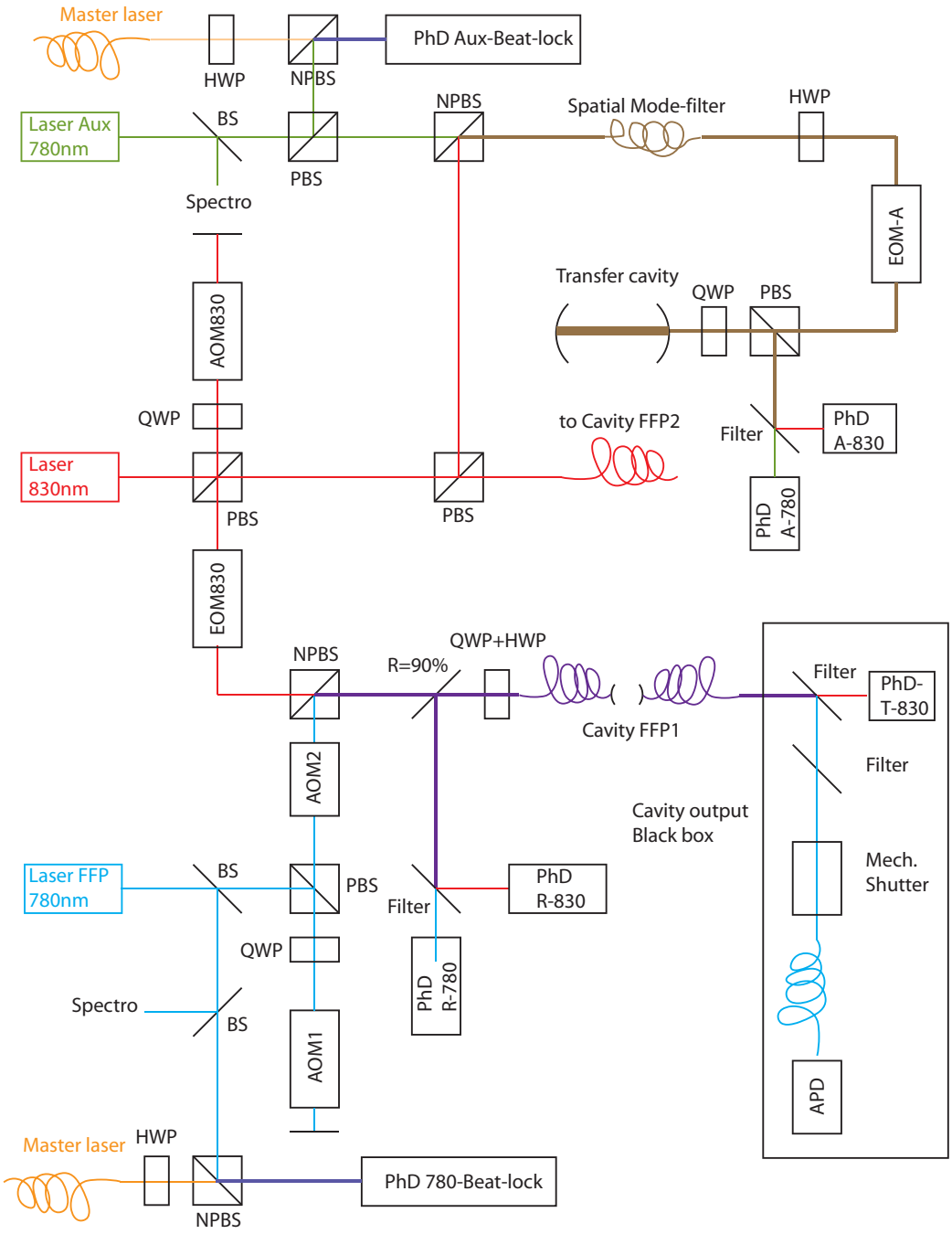

Figure 2.7: Laser system for the cavity. The different beams are depicted with different colours, thicker lines indicate superimposed beams.
Not shown: optical isolators; filters for the AOM zero-order output; lenses for mode-matching at fibre-couplers and transfer cavity input, focusing onto the AOM and photodiodes apertures; HWP in front of PBS.

The transfer cavity is a simple symmetric concave cavity with mirrors of curvature $R = 10$ cm and diameter 0.5". The body of the cavity is a single piece of Aluminium of approximative length 10 cm, which yields a free-spectral-range of $\mathrm{FSR}' = 2\pi \times 1.5$ GHz. The longitudinal positions of the mirrors are adjusted by coarse screws, and one of the mirror is mounted on a piezo stack. The mirrors have an intrinsic measured finesse of 2000, which corresponds to a linewidth of 0.75 MHz (FWHM). When used in the confocal configuration, the linewidth increases to approximately 2 MHz (FWHM) due to non-perfect frequency superimposition of the various transverse modes. The stability of the final lock is however limited by the linewidth of the FFP cavity, which is much larger. The confocal configuration has the strong advantage to realize a stable injection even when the beams are not perfectly mode-matched to the TEM00 mode. In our case, we use two beams with a large wavelength difference, and it is difficult to achieve a satisfactory mode-matching with both wavelengths at the same time. Other experimental works reported similar results [51].

The FSR in the confocal configuration is measured at $\mathrm{FSR}' = 2\pi \times 745(3)$ MHz, corresponding to an effective length $L' = 43$ cm, 4 times the distance between the mirrors. This relatively small FSR allows us to reach a resonance from any initial frequency with a maximum detuning of less than 400 MHz. At the same time, the value of the discrete step between double resonances is not to small: $\delta(\Delta_0) = \mathrm{FSR}'(\frac{n_{780}}{n_{830}} - 1) = 2\pi \times 47.5$ MHz, which permits to identify quite easily the mode number.

The transfer cavity is temperature-stabilised to obtain a stable effective length L'. The goal of the temperature stabilisation is double here: first, we need to be able to lock the cavity for hours on the same line within the piezo range (as usual for a cavity), but also we want to be able to identify from one day to the other on which double resonance set we are tuned, and optimally to lock the cavity always on the same double resonance. The requirement is then that the long term length drift is smaller than a few wavelengths (the piezo range is approximately 3 FSR). The temperature fluctuation leads to a drift of $\Delta L'/\Delta T = 10\mu$m/K [15], which put the requirements on the long-term temperature stability at a level of 0.1 K, while the temperature in the room fluctuates by 1.5K on a 15-min time scale. The temperature stabilisation system is simple. First, the cavity is enclosed in a cardboard box, filled with some foam to block the air flow. Then, a thin copper wire of resistance 4Ω is rolled around the cavity, while the temperature of the cavity mount is measured with a thermistor located between the copper wire and the mount. We apply an active feedback on the current running in the wire with an inte-

[15] Computed from Al thermal expansion coefficient and checked experimentally

gration time constant of approximately 1 minute. The resulting temperature fluctuation is measured at 0.005K on a one hour timescale, which shows that the feedback efficiently suppresses the room temperature fluctuation by a factor >100. One a day timescale, we observe a fluctuation of the cavity length with an amplitude $\sim 0.2\mu$m, not correlated to the room temperature. We attribute it to pressure changes in the room ($\Delta p = 10$ hPa$\rightarrow \Delta L' = 1\mu$m). Therefore we conclude that the temperature stabilisation is good enough for our purpose, and that the use of expensive materials with smaller thermal expansion coefficients (invar, ULE glass) is not necessary here.

The auxiliary beam at frequency ω'_{780} is obtained from an auxiliary laser at 780 nm. To get the condition $\omega'_{780} = \omega_a + \Delta_{aux}$, with a tunable, well controlled Δ_{aux} we implement a beat lock with the master laser, using a fast photodiode[16], a DC - 1GHz amplifier[17], and a 50 - 1100 MHz frequency-to-voltage converter[18]. The value of Δ_{aux} is locked to the desired value by applying a feedback signal to the grating piezo. The long term drift is $\ll 250$ kHz/h. The 830' nm beam is produced from a 830 nm laser diode[19], mounted in the usual external cavity configuration. Approximately 100 μW of this beam is superimposed to the auxiliary beam at 780 nm on a non-polarising beamsplitter cube. The resulting beam is mode filtered before being phase-modulated at $f_{mod} = 17.9$ MHz with an electro-optic phase modulator[20](EOM-A), and finally injected in the transfer cavity. The reflections on the transfer cavity are separated by an interference filter[21] and measured with two 150MHz amplified photodiodes[22] (PhD A-780 and A-830). The intensities are demodulated to obtain two independent Pound-Drever-Hall lock signals [52], one for the 780' beam, one for the 830' beam. The first signal is used to compensate the transfer cavity length fluctuations, the second one acts on the grating piezo to set the frequency of the 830' beam.

The rest of the 830 nm laser beam is frequency shifted by a double pass AOM (AOM830) to obtain the detuning Δ_{830} and set the beam power at the input of the FFP cavity. It is phase-modulated at 1.7 GHz with a fibre-EOM[23], before being injected in the input cavity fibre. The reflection signal is filtered at 830 nm, then measured with a 1-2.8 GHz photodiode[24] and

[16]Hamamatsu MSM G4176-03, with SMA connector
[17]Minicircuits MCL-ZFL-1000LN
[18]Home-built, courtesy of the atomchip clock team of SYRTE.
[19]Sanyo DL 8032-01
[20]Qubig EO-F20L, with a 3 mm aperture.
[21]Semrock BL-786.
[22]Thorlabs PDA-10.
[23]EOSPACE PM-0K5-10-PFA-PFA-800-UL.
[24]Hamamatsu MSM G4176-03, amplified by 2 × Kuhne KU LNA BB 2000 LSF-SMA

demodulated to obtain a Pound-Drever-Hall signal which is fed to the cavity piezo.

Performance

With this setup, we obtain a stable lock of the cavity at any user-defined detuning. We can perform scans of the cavity resonance frequency of amplitude approximately 1GHz. The lock of the cavity has a bandwidth of 5 kHz, mainly limited by the piezo resonance at 12.5 kHz.

Scan of the cavity with the transfer lock scheme

We can perform a scan of the cavity resonance frequency by scanning the frequency of the auxiliary laser Δ_{aux}. The transmission is measured with the APD, when the probe beam is locked to a Rubidium resonance. We obtain a Lorentz-shaped transmission curve with a linewidth $2\kappa = 105$ MHz (see Fig. 2.2.1Top), approximately the same value as if we perform a scan of the probe laser frequency.

Cavity frequency noise

We performed a measurement of the cavity transmission noise, using a probe frequency $\omega_L = \omega_a$ and for two possible settings of the cavity transmission $\omega_c = \omega_a$ and $\omega_c = \omega_a + \kappa$. The noise spectrum is computed from the APD trace with an integration time constant of 40 μs corresponding to 80 counts/bin. The results are shown on Fig. Bottom. Some peaks are present only at $\omega_c = \omega_a + \kappa$ which indicates they correspond to frequency fluctuations, with typical frequencies 2.5 kHz and 12.5 kHz which are the piezo resonance frequencies.

2.2.2 Optical setup for probing the cavity and measuring the transmission

This corresponds to the lower part of Fig. 2.7. The cavity is probed with a 780 nm laser, beat-locked to the master laser. The power of the beam is controlled by two AOMs (AOM1, AOM2) to obtain an extinction ratio of $> 10^6$. It is then superimposed to the 830 nm beam, and injected to the cavity. At the output of the cavity, the 780 nm is separated from the 830 nm with two interference filters, and then the photon flux is measured with an APD[25].

with Bias-T option.

[25] Perkin-Elmer SPCM-AQR-14.

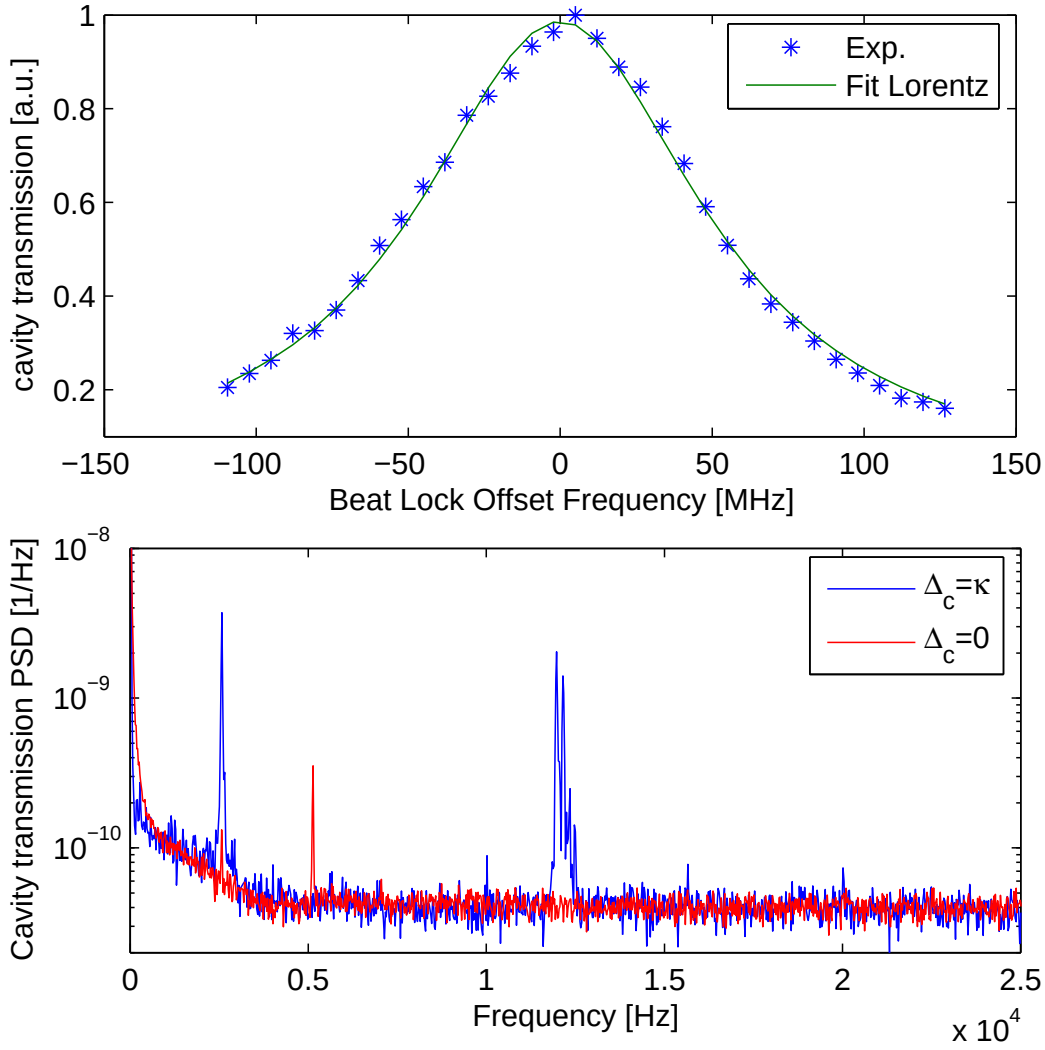

Figure 2.8: Top: Scan of the cavity. The green curve is a Lorentz fit with 105 MHz FWHM. Bottom: Noise spectrum of the cavity. The cavity frequency is set at $\Delta_c = \kappa$ (blue) or $\Delta_c = 0$ (red).

We measured a loss factor of $\eta_F = 0.8$ between the output of the multimode fibre and the input of the APD. Taking into account the losses at the output mirror of the cavity, we can estimate the number of photons in the cavity mode with the measured photon flux Φ with the formula

$$\Phi = n\kappa \frac{T}{T+L} \eta_F \eta_{APD} = n\kappa \times 0.16, \tag{2.6}$$

with the numeric values $T = 31$ ppm, $L = 56$ ppm for the mirror coeffi-

cients[26], $\eta_{APD} = 0.55$ for the APD quantum efficiency[27].

[26]These are the manufacturer values. Only the finesse $F = \frac{\pi}{T+L}$ can be measured experimentally, and is in a good agreement with the specifications.

[27]Manufacturer value. Without a single photon source, only the count rate can be measured for a given beam power, and the ratio in good agreement with the specifications.

2.2.3 Cavity specifications for QED

The cavity has a measured linewidth (FWHM) $2\kappa = 2\pi \times 104$ MHz and a free-spectral-range of $FSR = 2\pi \times 3.85$ THz (~ 8 nm), which corresponds to a cavity "physical" length $d \simeq 39\mu$m. The finesse is therefore $F = \mathrm{FSR}/(2\kappa) \simeq 37000$.

The expression for a TEM00 mode in a spherical-spherical resonator is given by the standard formula for Gaussian beams [53]

$$E = E_0 \frac{w_0}{w(y)} \cos\left[ky + k\frac{r_\perp^2}{2R(y)} - \Psi(y)\right] \exp\left[\frac{-r_\perp^2}{w^2(y)}\right], \tag{2.7}$$

where the parameters are

$$\begin{aligned} w^2(y) &= w_0^2(1 + (y/y_0)^2) && (2.8)\\ R(y) &= y + y_0^2/y && (2.9)\\ \Psi(y) &= \tan^{-1}(y/y_0) && (2.10)\\ y_0 &= \pi w_0^2/\lambda && (2.11) \end{aligned}$$

We find the value of the beam waist w_0 by matching the wave curvature $R(y)$ with the curvature of the mirrors $R(y_2) = R_2$, $R(y_1) = -R_1$, imposing at the same time $y_2 - y_1 = d$, the fixed distance between the mirrors. The solution for the waist reads [54]:

$$w_0 = \left(\frac{\lambda}{\pi}\left[\frac{d(R_1 - d)(R_2 - d)(R_1 + R_2 - d)}{(R_1 + R_2 - 2d)^2}\right]^{\frac{1}{2}}\right)^{\frac{1}{2}}, \tag{2.12}$$

which, computed for our cavity parameters $d = 39\mu$m, $R_1 = 450\mu$m, $R_2 = 150\mu$, yields $w_0 = 3.9\mu$m at $\lambda = 780$ nm. The mode volume can be exactly computed from $V_m E_0^2 = \int d^3 r E(r)^2 = E_0^2 \pi w_0^2 d/4$, therefore we obtain

$$V_m = \frac{\pi w_0^2 d}{4} \tag{2.13}$$

From the mode volume, we compute the maximum coupling g_m of the $|F = 2; m_F = 2\rangle \rightarrow |F' = 3; m'_F = 3\rangle$ σ^+-transition with the formula

$$g_m = \sqrt{\hbar\omega} 2\varepsilon_0 V_m d_{22\rightarrow 33}/\hbar \simeq 2\pi \times 210 \text{ MHz}, \tag{2.14}$$

and the single-atom maximum cooperativy for the same transition

$$C_m = \frac{g_m^2}{2\kappa\gamma} \simeq 150. \tag{2.15}$$

The cavity exhibits birefringence with separated peaks corresponding to two orthogonal input polarisations. The splitting $\delta w_b = 2\pi \times 400 \pm 20$ MHz is very small compared to the FSR and both peaks can be attributed to the same longitudinal and transverse too mode number. The origin of this birefringence is probably related to the deposition process of the HR coating: the surface to coat is strongly curved, and it is slightly asymmetric, which defines two principal axis with different radii of curvature. During the coating process, it is likely that the stress on the coating material is not the same for the two axis, inducing a small birefringence for the resulting mirror. The relative phase shift due to this birefringence is of the order of $2\pi n \delta\omega_b/\omega \sim 10^{-3}$ rad. Therefore, the eigenpolarisations of the cavity are almost linear, provided the birefringence itself is linear. However, because of the fibres, we cannot measure this polarisation precisely. The experience of "macroscopic" cavity QED groups tells us that the birefringence induced by stress on the mirror coatings is linear [55, 56]. Nevertheless, the typical phase shift in their situations seems to be much smaller ($\sim 10^{-6}$, [56]). With the large curvatures of our mirrors, a larger value was anyway to be expected. This birefringence is always an issue since it forbids to drive the cycling transition $|F = 2; m_F = 2\rangle \rightarrow |F' = 3; m'_F = 3\rangle$ which has the strongest coupling rate.

2.2.4 Dipole trap characterisation

The cavity stabilisation light at 830 nm is also used in the experiment to generate a dipole trap. The shape of the dipole trap potential is given by

$$V = -U \cos(k_{830} y)^2 \exp\left(-\frac{2\mathbf{r}_\perp^2}{w_{830}^2}\right) \tag{2.16}$$

The frequencies are computed by expanding the potential near the minimum at $(y = 0; \mathbf{r}_\perp = 0)$:

$$\omega_y = \sqrt{\frac{2U k_{830}^2}{m}} \tag{2.17}$$

$$\omega_\perp = \sqrt{\frac{4U}{m w_{830}^2}} \tag{2.18}$$

The ratio between the trap frequencies is then given by
$\omega_y/\omega_\perp = k_{830} w_{830}/\sqrt{2} \simeq 21$ with $w_{830} = 4.0$ μm. The value of the trap depth U is difficult to estimate from the cavity transmission at 830 nm since the coating specifications at 830 nm are not provided. We therefore need to perform a calibration of U versus the 830 nm power, by measuring directly the trap frequency.

We measure the trap frequency $f_y = \omega_y/2\pi$ with a parametric heating experiment performed on a shallow dipole trap. The 830 nm laser-diode current is modulated at a frequency f_{mod}, which induces fluctuations of the trap depth at frequency f_{mod} (and multiples). A cloud of approximately 100 atoms is loaded in a weak modulated dipole trap, where its stays for 50 ms before it is imaged with the camera. The number of remaining atoms is measured as a function of the modulation frequency (Fig. 2.9 Top.). The losses are maximum for two possible modulation frequencies $f_{mod,1}$ and $f_{mod,2} \simeq f_{mod,1} \times 2$. According to previous experiments [57], we attribute these loss processes to trap shaking ($f_{mod,1} = f_y$) and parametric heating ($f_{mod,2} = 2f_y$). We measure the trap frequency f_y for various dipole laser power and observe the $f_y \sim \sqrt{U}$ scaling law (see Fig. 2.9 Bottom.). This experiment provides a calibration of the dipole trap depth and frequencies, which is valid for any dipole trap power.

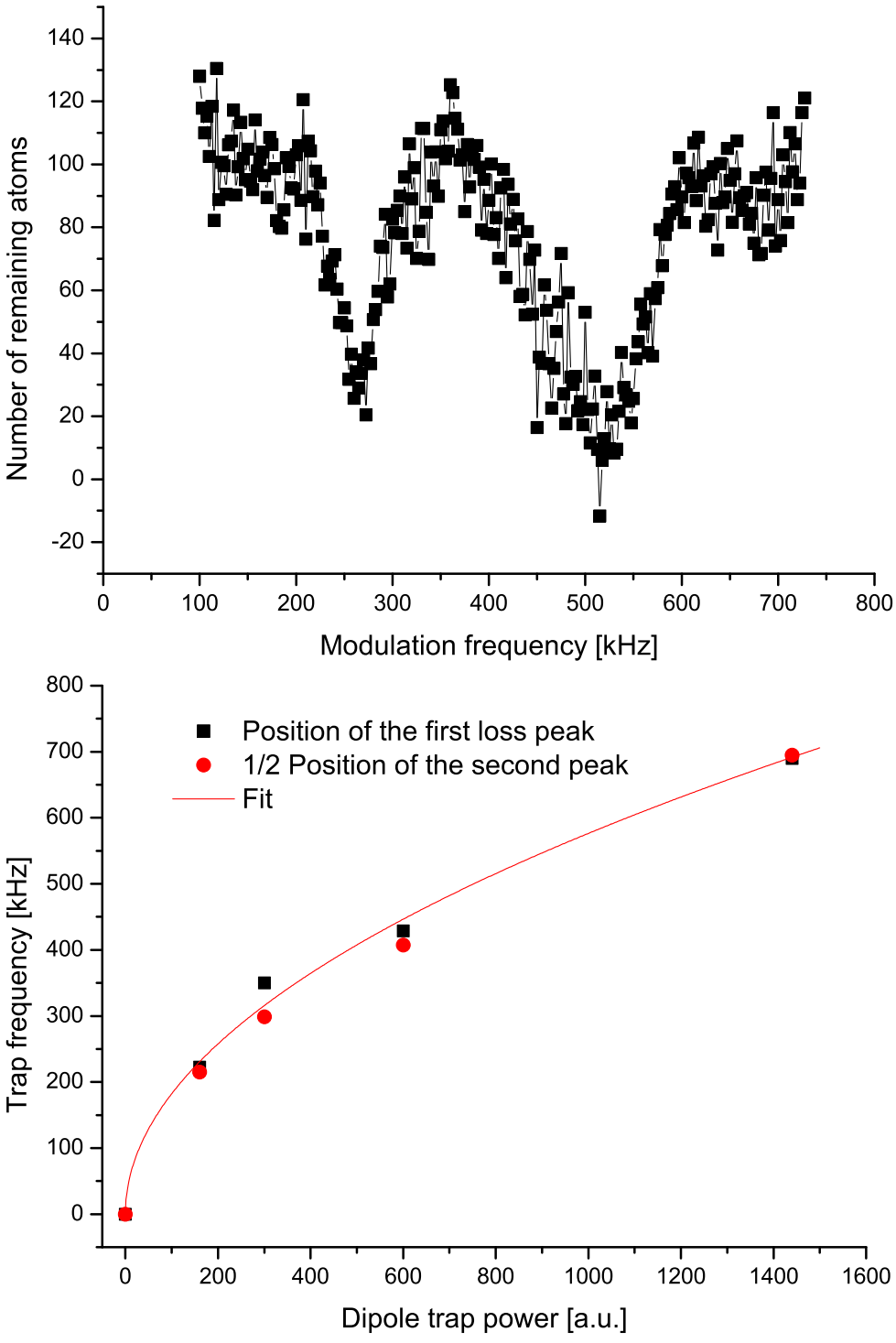

Figure 2.9: Calibration of the dipole trap frequency f_y.
Top: Remaining atoms as a function of trap modulation frequency f_{mod}.
Bottom: Modulation frequency for the two loss peaks, for different dipole trap depths. The frequency of the second peak is divided by two. The full line is a square-root fit.

2.3 Microwave source

In the experiment, we intend to drive Rabi oscillations between ground state levels $|F = 1\rangle$ and $|F = 2\rangle$, which are approximately separated by 6.8 GHz. The hyperfine and Zeeman structure is depicted on Fig. 2.10. These transitions are of the magnetic-dipole type, and must satisfy the selection rules $\Delta m_F = 0, \pm 1$. Due to the great stability of ground state levels (lifetime $\sim$ minutes), the microwave frequency has to be tuned very close to the resonance. The Zeeman sublevels are sensitive to the magnetic field to the first order, excepted for the $m_F = 0$ levels, with a Landé factor $g_{F=1} = -1/2$ and $g_{F=2} = 1/2$. The linear shift is given by

$$\Delta\mathcal{E}_{F;m_F} = \mu_B g_F m_F \simeq \pm(B/1G) \times m_F \times 0.70 \text{ MHz}. \tag{2.19}$$

The resonance frequency of the transition $|F = 1; m_{F_1}\rangle \rightarrow |F = 2; m_{F_2}\rangle$ is therefore given by

$$\begin{aligned} f_{m_{F_1}\rightarrow m_{F_2}}(B) &= f_{0\rightarrow 0} + \mu_B/2h(m_{F_2} - m_{F_1}) && (2.20) \\ &\simeq 6834.682 + (B/1G) \times (m_{F_2} - m_{F_1}) \times 0.70 \text{ MHz} && (2.21) \end{aligned}$$

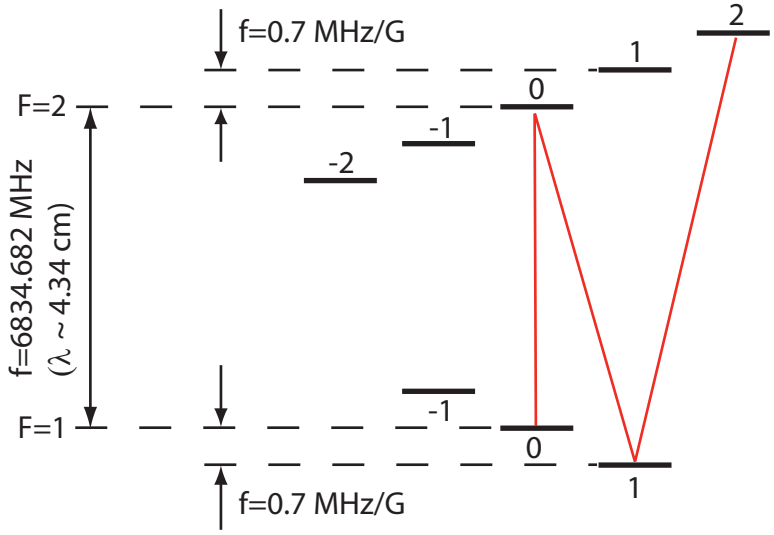

Figure 2.10: Level diagram of the 5S1/2 multiplet. The red lines are the transitions we drive in the experiment.

2.3.1 Design and performance

A single tone, frequency-tunable microwave is generated by the microwave chain described on Fig. 2.11 Top. The microwave signal is obtained by the mixing of a radiofrequency and a microwave of in a single sideband (SSB) mixer[28], which takes for input a microwave and two radiofrequencies of frequency f shifted by 90 °. The microwave component at $f_{mw,0} = 6800$ MHz is generated by a yttrium-iron-garnet oscillator[29]. The radiofrequency is generated by a 4-output direct-digital-synthetiser (DDS)[30], which is interfaced to the computer via a USB connection. Up to 4 different frequencies can programmed, and then switched during the experiment. Both the DDS and the mw oscillator are phase-locked to a common frequency reference at 100 MHz, which is derived from an oven-controlled ultrastable quartz oscillator at 10 MHz[31]. The output of the SSB mixer at $f_{mw} = f_{mw,0} + f$ is fed to an amplification chain[32] of global gain 51dB to obtain a 15W microwave signal. The output of the last amplifier is connected[33] to a coaxial-waveguide adaptor[34] which acts as an antenna, located approximately 50 cm away the vacuum cell, and directed towards it. The amplifier is protected from the reflections on the antenna by a mw circulator[35]. The microwave output is switched on and off by a TTL-controlled mw switch[36], with a specified rise time below 10 ns, which allows to work in the pulsing regime.

The frequency stability of the mw output signal is characterised by a phase noise curve, displayed on Fig. 2.11 Bottom. The phase noise curve is measured with the help of an Agilent N9010A signal analyser, and compared to a reference mw signal generator Agilent E8257D. The custom-made MW chain performs almost as well as the reference generator in terms of phase noise.

[28] Pulsar Microwave IMOH-03-458

[29] Microlambda wireless M2PE-1285

[30] Analog Devices AD9959, with evaluation board. The evaluation board was modified to enable real-time switching of the output frequency and phase reset with TTL signals

[31] 10 MHz oscillator: Oscilloquartz OCX08789
100 MHz phase-locked oscillator: Wenzel Associates 501-10137

[32] 2× Kuhne KUPA682-TR-UM, then Kuhne KUPA682-XH-UM

[33] Cable: C&C connectique CSU528AA

[34] Pasternack PE-9830

[35] Aerotek H16-1FFF

[36] Miteq S136-BDMO, discontinued

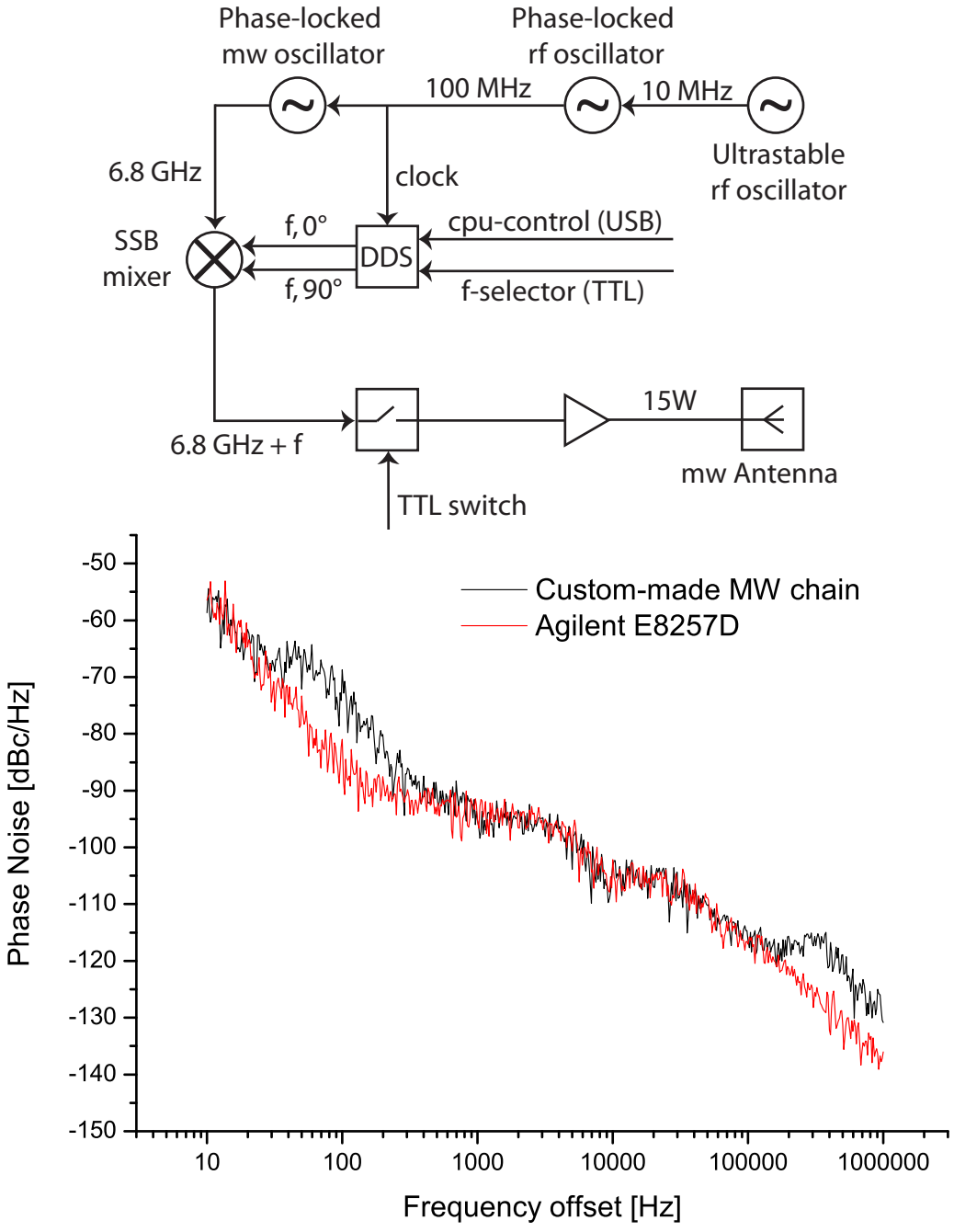

Figure 2.11: MW chain design and performance.
Top: Schematic of the microwave chain.
Bottom: Phase noise of the microwave chain (black curve). The red curve is a reference curve taken with an Agilent E8257D signal generator.

2.3.2 Measurement of Rabi frequencies

As a preliminary work for experiments with single atoms, we measure the resonance frequencies and the Rabi frequencies for the transitions we need for the experiment, which are depicted in red on the level diagram (Fig. 2.10). We start with the transition $|F = 1; m_F = 1\rangle \rightarrow |F = 2; m_F = 2\rangle$. Because of remnant field gradients always present in the experiment and inhomogeneous mw power, we have to measure the characteristics of the transition at the position we want to drive it, i.e. in the intracavity dipole trap. We use the dipole trap depth which maximises the number of atoms we can load inside. It corresponds approximately to the weakest trap we can achieve without losing the cavity length stabilisation. To obtain the transition frequency at any dipole trap depth, we have to correct for the so-called differential light shift: the light shift experienced by $F = 2$ atoms is slightly larger in absolute value than for the $F = 1$ atoms, because of the different detunings. The transition frequency is reduced for stronger dipole traps, by an amount $\delta\omega = 3.5 \times 10^{-4} \times U$, where U is the dipole trap depth.

Starting from a BEC of $|F = 2; m_F = 2\rangle$, we load approximatively 250 atoms in the dipole trap, and then switch off the magnetic trap while keeping a magnetic bias field of about 4G. Then, we apply the mw for a duration t_{mw}, and measure the number of atoms which remained in the $|F = 2\rangle$ state by absorption imaging. If the mw source is tuned close enough to resonance ($f_{mw} \sim f_0 \equiv f_{m_{F_1}=1 \rightarrow m_{F_2}=2}$), the Rabi oscillations are observed (see Fig. 2.12 Top). The "effective" Rabi frequency f and the contrast $\mathcal{C}$ of these oscillations are given by the equations:

$$f = \sqrt{f_R^2 + (f_{mw} - f_0)^2} \tag{2.22}$$

$$\mathcal{C} = \frac{f_R^2}{f_R^2 + (f_{mw} - f_0)^2}, \tag{2.23}$$

where f_R is the resonant Rabi frequency (or Rabi frequency when there is no ambiguity), and is proportional to the microwave field amplitude. From the observed dependence $f(f_{mw})$, we extract accurately the resonant Rabi frequency $f_R = 290(3)$ kHz and the position of the resonance $f_0 = 6842575(5)$ kHz (see Fig. 2.12 Bottom). As expected, the contrast is maximal when the effective Rabi frequency is minimal. The contrast peaks at 0.75, a value limited by the imaging noise. We can observe Rabi oscillations on a duration which is larger than 1 ms, but we did not measure precisely the coherence time.

The measurement of a single transition frequency allows to calibrate the magnetic field magnitude with a relative precision of approximately 10^{-3}. We

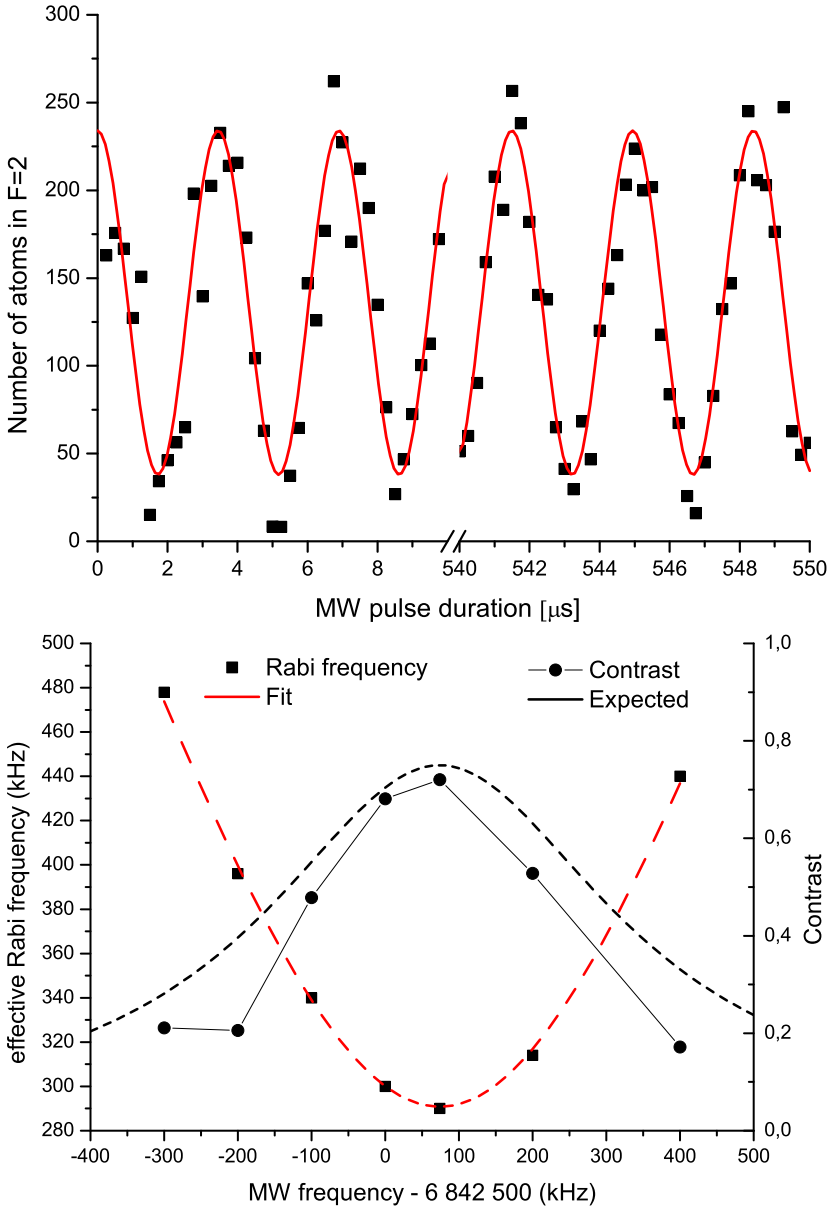

Figure 2.12: Rabi oscillations on the $|F = 2; m_F = 2\rangle \rightarrow |F = 1; m_F = 1\rangle$ transition.
Top: The population in the initial state ($|F = 2\rangle$) is depicted as a function of microwave pulse duration, at resonance ($f_{mw} = f_0$). The red curve is a cosine fit with a contrast of 0.75 and a frequency of 290 kHz.
Bottom: Frequency (left axis) and contrast (right axis) of the Rabi oscillations, for different microwave frequency f_{mw}. The red dashed curve is a fit to the effective Rabi frequency, and yields the resonant Rabi frequency and the position of the resonance f_0 (used for the upper plot). The fit results are used to compute the expected contrast (black dashed curve), which we correct by a factor 0.75 to account for detection noise.

can then compute the frequencies of all the other transitions we are interested in with the help of the formula Eqn. 2.20 [37]. We just need then to measure the Rabi frequencies of the transitions $|F=1;m_F=1\rangle \rightarrow |F=2;m_F=0\rangle$ and $|F=1;m_F=0\rangle \rightarrow |F=2;m_F=0\rangle$. For the first, we transfer the atoms in the $|F=1;m_F=1\rangle$ state by applying a "π"-pulse of duration $t_\pi = 1/(2f_{R,11\rightarrow 22})$, then switch the microwave source frequency to the expected value for the $|F=1;m_F=1\rangle \rightarrow |F=2;m_F=0\rangle$ transition, and we observe the Rabi oscillations as previously. For the last transition (the "clock" transition), we have to apply two π-pulses and change the mw frequency twice. For a magnetic field $\mathbf{B}_{ext} = 3.690\,\mathrm{G}\times(\cos(30\,^\circ)\mathbf{e}_x + \sin(30\,^\circ)\mathbf{e}_z)$, and a microwave power reduced compared to the previous experiment, we found the following values for the resonant Rabi frequencies:

Transition ($m_{F_1} \rightarrow m_{F_2}$)	Rabi frequency [kHz]
$1 \rightarrow 2$	115(1)
$1 \rightarrow 0$	34(1)
$0 \rightarrow 0$	69(1)

The ratio between the Rabi frequencies of the different transitions depend on the microwave polarisation, and was found to be stable for months, even when the experimental setup was "tuned" (not to close to the cell though). This was not obvious from the beginning since the microwave polarisation at the position of the atoms is the result of the superposition of multiple reflected waves due to the presence of metallic surfaces all around the cell.

2.4 Experimental interface

The experiment is controlled by a computer equipped with analog and digital output PCI-cards[38]. The sequence consists in a source file containing a list of events when at least one value of the output cards changes. A program is used to convert this list into a table containing the values of the outputs at each time step. This table is then read by the driver of the analog/digital output cards. A sequence is defined once and for all by the initial source file, and cannot react to events occurring during the experiment. We have therefore slightly modified the system to enable this possibility. For that matter, we

[37] We can also take into account the second order correction using Breit-Rabi formula - this leads to a difference of about 10 kHz here for a 4G magnetic field.

[38] National Instruments

installed a microcontroller[39] which is able to read some input values (mainly digital, but there are also some analog inputs and a digital counter) and react according to their values. The microcontroller performs very well at digital tasks, with a reaction time of approximately 1 μs for the simplest tasks. Because of the small number of outputs available, the microcontroller we use cannot replace the computer cards, and we have to interface it with the computer. This is done in the following way, and summarised on Fig. 2.13:

1. Initially, the microcontroller is in a "copy mode". It reads the values of its inputs, and copy them to its outputs. The existence of the copy mode is mandatory since we want some output to be alternatively controller by the computer and the microcontroller.

2. When the control has to be given to the microcontroller, a signal is sent by the computer cards to one specific input of the microcontroller, called the trigger input. At this point, the microcontroller leaves the "copy mode" for the "autonomous mode".

3. The microcontroller executes its sequence. This sequences involves reading some values coming from the experiment, computing and applying the desired outputs, executing loops. In a single atom preparation scheme, the typical tasks are: changing the mw frequency, applying a mw pulse, applying a detection pulse, reading the number of APD counts.

4. When the sequence is done, the microcontroller returns to the "copy mode", until it is triggered again.

[39] ADWIN LIte, with digital input/output extension card.

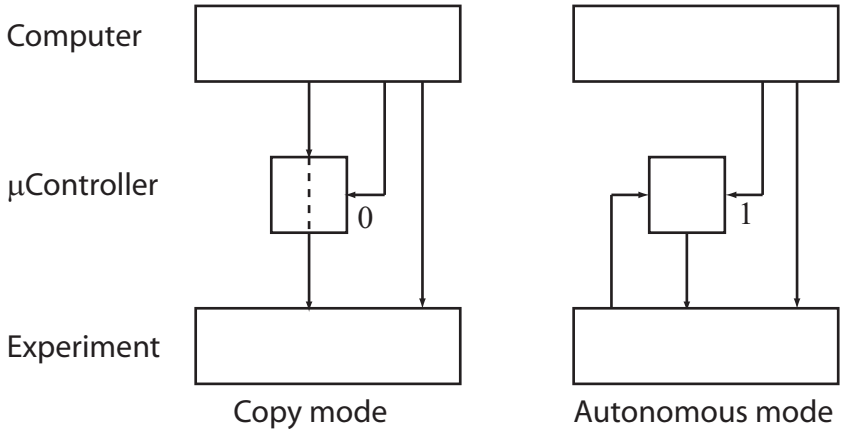

Figure 2.13: Control flow of the experimental interface. On the left is the microcontroller copy mode, on the tight the autonomous mode.

Chapter 3

Detection of single atoms in a waveguide

The calibration of a single atom detector is a difficult task, since it requires to achieve independently a reliable preparation of single atoms. In the first experiment which demonstrated single atom detection with optical cavities, an ultracold atomic cloud is dropped from a MOT located above the cavity [58]. The atoms, freely falling towards the cavity mode, cause a transmission drop when they enter it. The flux of atoms entering and leaving the cavity can be made small enough in order to avoid the presence of multiple atoms in the cavity mode at the same time. Most of the time, the cavity is empty and has a large transmission, and from time to time, a single atom enters the cavity mode, inducing a drop of the cavity transmission before it leaves and the transmission recovers its reference value. The transmission signal has therefore a telegraph-signal shape, with transmission "dips" associated with single atom transits. The observation of single atom transits, by the way of telegraph signals, is a direct proof of single atom detection. Contrary to indirect methods developed in [59, 60], it does not rely on statistical assumptions on atoms and photons statistics and provides a visual evidence that the setup is sensitive enough to see detect single atoms.

In such an experiment, the detection efficiency is usually limited by the spatial overlap between the expanding cloud and the cavity mode. A majority of atoms never reach the centre of the cavity mode where the coupling is maximum, and therefore cause a shallow dip which may not be detected. An efficiency of about 25 % was obtained with an "atom laser" which has a minimum transverse expansion [61]. In our experiment, we add a transverse confinement by the way of a magnetic bidimensional trap (or "waveguide") which guides the expanding cloud towards the cavity mode centre.

This chapter is separated in two sections: first, we describe the experiment which leads to the observation of single atom transits. Then, we analyse the properties of the detection in terms of detection efficiency and bandwidth.

3.1 Observation of single atom transits

The experiment is performed in two steps. The principle is summarised in Fig. 3.1. First, a quasi-pure condensate of about 1,000 or less $|F = 2; m_F = 2\rangle$ atoms is prepared in a 3D trap located 1.25 mm away from the cavity mode. Then, it is transferred to the waveguide trap which enables the propagation of the atoms towards the cavity mode. By monitoring the cavity transmission with the APD, we detect single atoms as they cross the cavity mode.

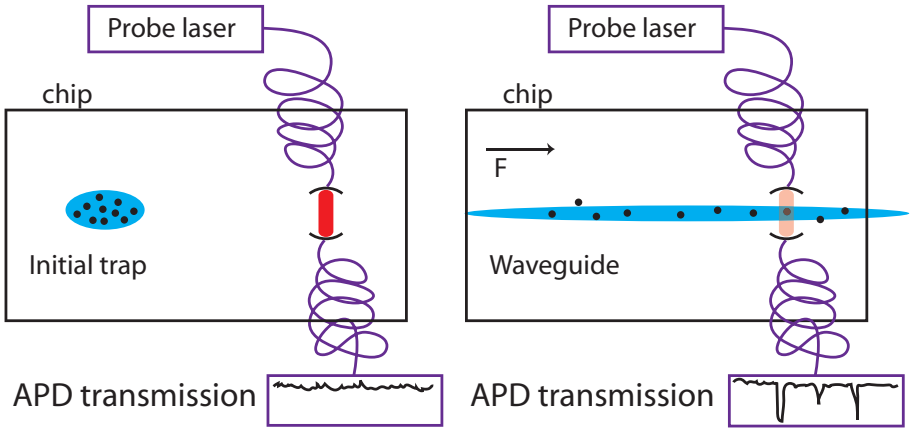

Figure 3.1: waveguide detection sketch with axis Schematic of the detection of waveguided atoms. On the left picture, the atoms are held trapped away from the cavity mode. On the right picture, the longitudinal confinement is release, and the atoms are detected by the cavity as they enter the cavity mode, leading to dips in the transmission signal.

3.1.1 Initial trapping and transfer to the waveguide

Efficient transfer of 3D-trapped atoms to a waveguide trap was demonstrated in [62]. Waveguide traps integrated to atom chips were realized in the first atom chips experiments [63]. Here, we implement a waveguide trap which runs through the cavity mode, and describe how we transfer atoms from a 3D trap to the waveguide.

Requirements

With a large number of wires, and the capability to drive them with independent currents, magnetic traps with almost any geometry can be realized on an atom chip. For this experiment, we need a 3D trap, that can be continuously changed into a 2D trap (waveguide). The geometry of the waveguide is imposed by the position of the cavity: the centre of the cavity is located at the position $x = 0$, $y = 0$, $z = z_0 = 150\mu$m. The waveguide has to be aligned with the x-axis, otherwise the atoms would hit the mirrors while entering the cavity mode. The geometry of the initial trap is constrained by the waveguide: the transverse confinement has to be similar to the waveguide, and the longitudinal confinement has to be tunable so that we are able to continuously decrease it to zero to realize the transfer to the waveguide trap. The position along the x-axis is chosen such as the expansion time is large enough to decrease the cloud density to the single atom regime.

Trap design

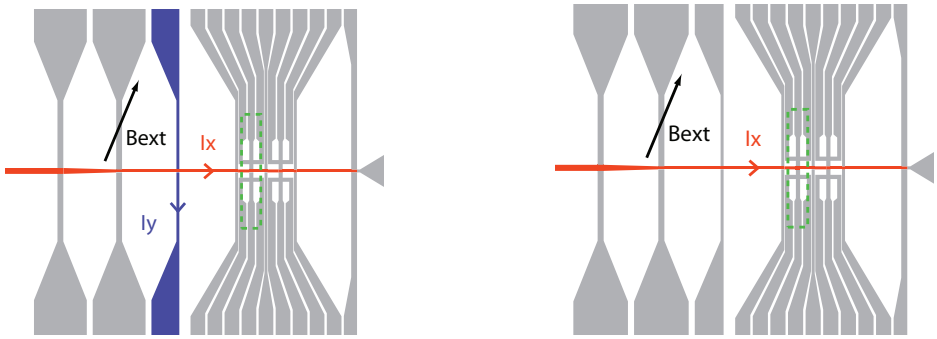

Figure 3.2: Atom chip wires and external bias field orientation for the dimple trap (left) and the waveguide trap (right). The cavity position is marked as a dashed rectangle.

The design of the waveguide trap is fairly straightforward: it requires only one atomchip wire in the x direction (located at $y = 0$) in which we run a DC current I_x, and a magnetic bias field $\mathbf{B}^{ext} = B_x^{ext}\mathbf{e}_x + B_y^{ext}\mathbf{e}_y$ generated by external coils (see Fig. 3.2). The y-component compensates exactly the wire field on the line ($z = z_0; y = 0$), where z_0 is defined by $\mu_0 I_x/2\pi z_0 = B_y^{ext}$. The x-component sets the magnetic field minimum to $|B_x^{ext}|$. With $I_x = 3$A, $B_y^{ext} = 40$G, and B_x^{ext}=1G, we realize a 2D trap at z_0=150 μm. The field curvature $B''_\perp = 7 \times 10^4$ G/mm^2 gives a trap frequency $f_\perp = 3.4$ kHz for atoms in state $|F = 2; m_F = 2\rangle$.

The 2D trap is changed into a 3D trap by adding a x-dependence in the magnetic field. For that matter, we run a small current $I_y = -\alpha I_x$ in a chip wire perpendicular to the waveguide axis, located at $x = x_d = -1.25$mm (see Fig. 3.2 Left). Together with the external field x-component $B_x^{ext} = \beta B_y^{ext}$, it generates a dimple trap with a slow axis along x, symmetric in the yz-plane. The centre of the trap is at $(x = x_d;\, y = 0;\, z = z_0)$. The distance between this trap and the cavity is then 1.25mm. With $B_y^{ext} = 40$ G, $\alpha = 0.02$, $\beta = 0.04$, the resulting trap frequencies are $(f_x; f_\perp) = (100; 3500)$ Hz, and the trap bottom is 0.8 G.

The dimple can be continuously changed into the waveguide by ramping the values of I_y and B_x^{ext}.

Release in the waveguide trap

After BEC preparation in the dimple trap, the axial confinement is abruptly removed by switching off the current in the dimple trap. At the same time, the external magnetic field is adjusted in order to keep constant the magnetic field magnitude at the trap bottom. This is done in a 1ms timescale, chosen to stay adiabatic only for the transverse direction and ensure that the cloud expands quickly in the axial direction. In the waveguide, the condensate propagates but it is extremely sensitive to any parasitic magnetic potential $\Delta B(x)$ of a few mG. Origins and effects of potential corrugation have been extensively studied in the atom chip community. In the simplest trap on a chip, the Z-trap, the parasitic potential is directly linked to wire imperfections ([64]), and leads to BEC fragmentation when the chip-trap distance decreases below typical values of the order of 100μm ([65], [66]). In our experiment, however, we are limited by the existence of wire crossings along the waveguide axis in which the current flow strongly deviates from the straight line. In addition, there might be small remnant currents running in perpendicular wires, since the current sources are not completely floating. As a consequence, the expanding BEC does not cover the 1.25mm distance to the detector position. To overcome the problem, we add a magnetic field gradient in the axial direction to force the BEC to expand and move towards the detector. We use a pair of chip wires perpendicular to the waveguide, located at $x =$ -1mm (push wire) and $x = 3$ mm (pull wire), in which we run a DC current. A magnetic field in the xz plane is generated, and while the z component leads only to a slight displacement of the waveguide axis, the x component generates a valley potential (see Fig. 3.3)

$$B_x(x) = \frac{\mu_0 I_w z_0}{2\pi((x - x_w)^2 + z_0^2)}. \tag{3.1}$$

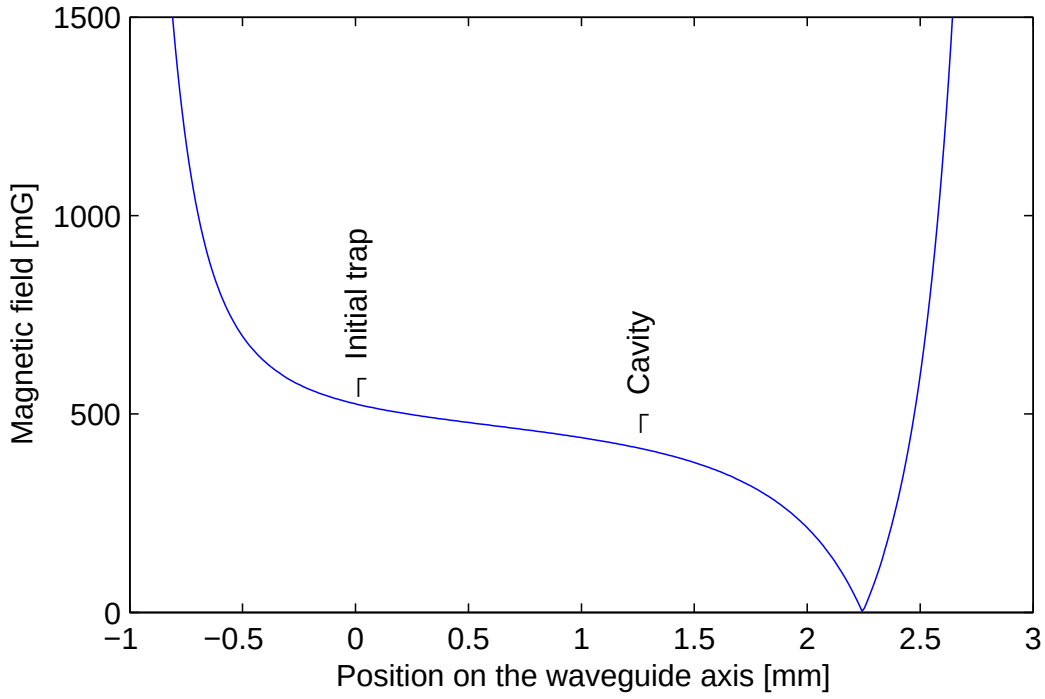

Figure 3.3: Magnetic potential valley generated by the push and pull wires, with $I_{push} = 200$ mA, $I_{pull} = -1000$ mA. Positions of initial dimple trap and cavity detection are marked.

Following this potential, the atoms typically need 100 ms to reach the detector position located 1.25mm away.

3.1.2 Observation of telegraph signals

The waveguide is aligned and optimised to intersect the cavity mode in its centre. For a thermal cloud with a temperature of $T = 1\mu$K, the transverse RMS size is given by $a_\perp \sim 0.5\mu$m, compared to a cavity waist of 4μm. Therefore, for a fairly large range of temperatures, all atoms should enter the cavity mode when they reach the position $x = 0$.

The cavity is kept locked with a weak 830 nm laser, and is continuously probed with the 780 nm laser, on resonance with the cavity and red-detuned from the atomic resonance by an amount $\Delta_a = \omega - \omega_a = -7\gamma$. The probe power is set in order to obtain a reference detected photon flux $\Phi_{ref} = 2$ MCts/s.

With an initial condensate of about 200 atoms, we measure a typical telegraph signal for the transmission shown on Fig. 3.4. The atoms reach the detector after a mean expansion time of about 100ms, which manifests on the detector signal as a maximum density of dips (Fig.3.4 Top). This value is in agreement with what we expect for the classical motion of the cloud centre-of-mass in the tilted waveguide. Moreover, we can estimate the mean velocity of the atoms at the position of the detector to be $v_x \simeq 20$mm/s.

Looking at a time window where the atomic flux is smaller (Fig.3.4 Bottom), we experimentally confirm that we are in the single atom detection regime: the typical transit time ($\lesssim 50\mu$s) is found to be much smaller than the waiting time between two transits (~ 1ms).

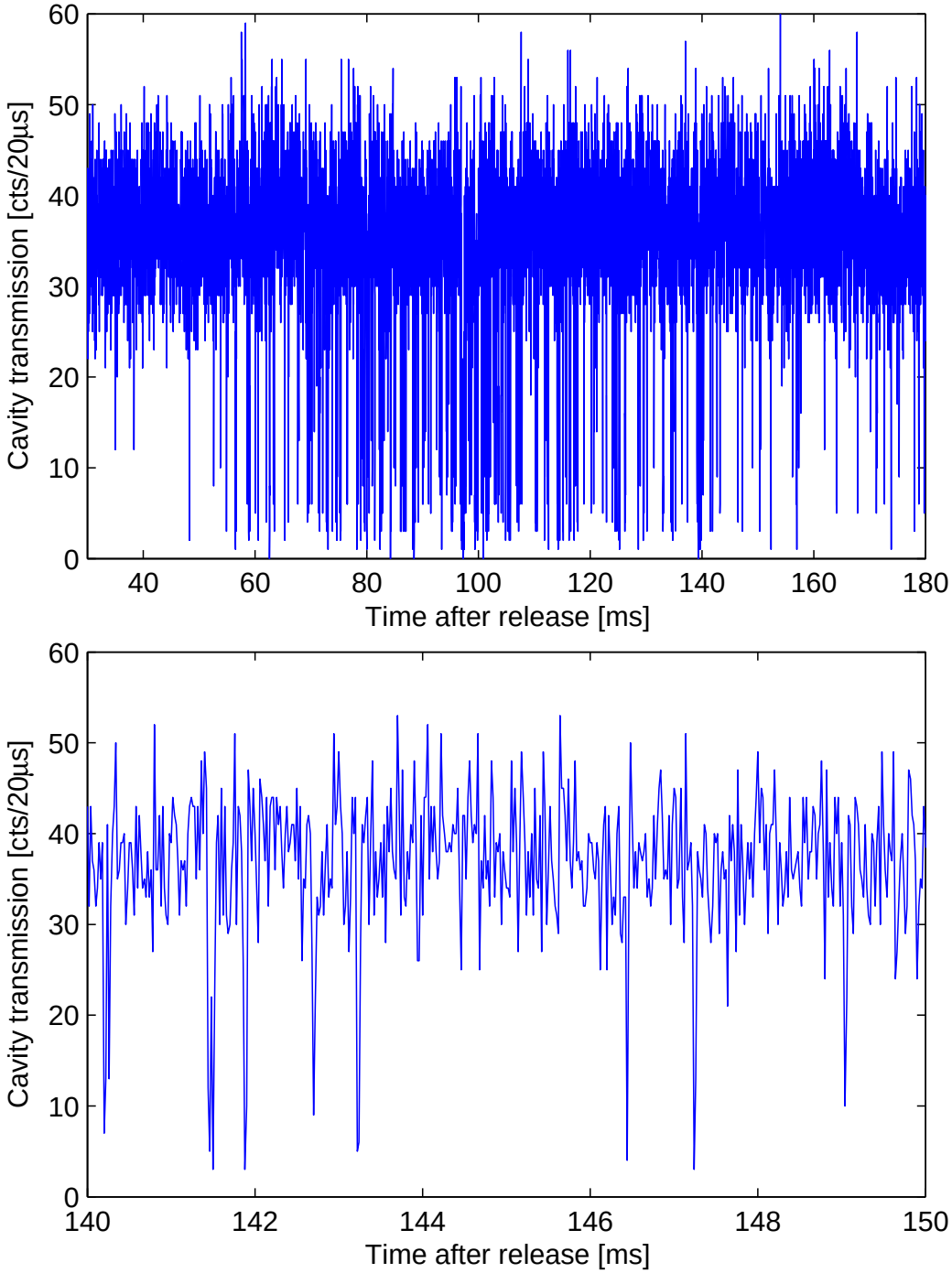

Figure 3.4: Observation of a telegraph signal. The cavity is probed at $\Delta_a = -7\gamma$, $\Delta_c = 0$ and with a reference power $\Phi_{ref} = 2$ MCts/s. The output rate is integrated with a 20 μs time constant and depicted as a function of time after release in the waveguide. The lower plot is a zoom on the low density region.

3.2 Detector performance

The observation of telegraph signals in the regime of small atomic density proves that the cavity has the capability to detect single atoms. Nevertheless, this does not mean that all atoms are detected. Some atoms lead to transmission dips shallower than others, and some might not even be detected at all.

In this section we analyse the performances of the detector, and investigate the processes limiting them.

3.2.1 Signal analysis

To perform a systematic analysis of the telegraph signals, we have to define precisely the notion of detection event. The cavity output flux is continuously monitored by the APD, and counts are grouped into time bins

$$B_i = [i\tau_{bin}; (i+1)\tau_{bin}] \tag{3.2}$$

of duration $\tau_{bin} = 20$ μs. n_i is the number of counts that happen during this time bin. A detection event consists in a set of N_b consecutive time bins for which the number of counts drops below a threshold value n_{thr}. It correspond therefore to a time interval $[t_1; t_2]$, with $t_2 - t_1 = N_b\tau_{bin}$.

For each detection event, we define the signal minimum $m = \min n_i$, where i runs though the bin numbers of the particular detection event. Single atoms entering the cavity mode and approaching the centre see an increasing coupling to the mode g which induces an increasing drop of the cavity transmission. The value of the signal minimum m is then related to the maximum coupling the atom reaches during its transit through the cavity mode. The distribution of values of m, plotted on Fig.3.5 (Left), is peaked at $m = 0$, which indicates that most detected atoms are detected with a large signal to noise. However, the distribution continuously drops to 0 as m approaches n_{thr}, which shows that some atoms are only hardly detected and indicates certainly that some atoms are not detected at all.

We can also define the signal duration $N_b \times \tau_{bin}$ for each detection event. The distribution of signal durations (see Fig.3.5 Right) shows that most atoms stay less than 100μs in the cavity mode, with a mean signal duration of about 40μs. Compared to the expected transit time $w/v_x \simeq 200\mu$s, this value is significantly smaller.

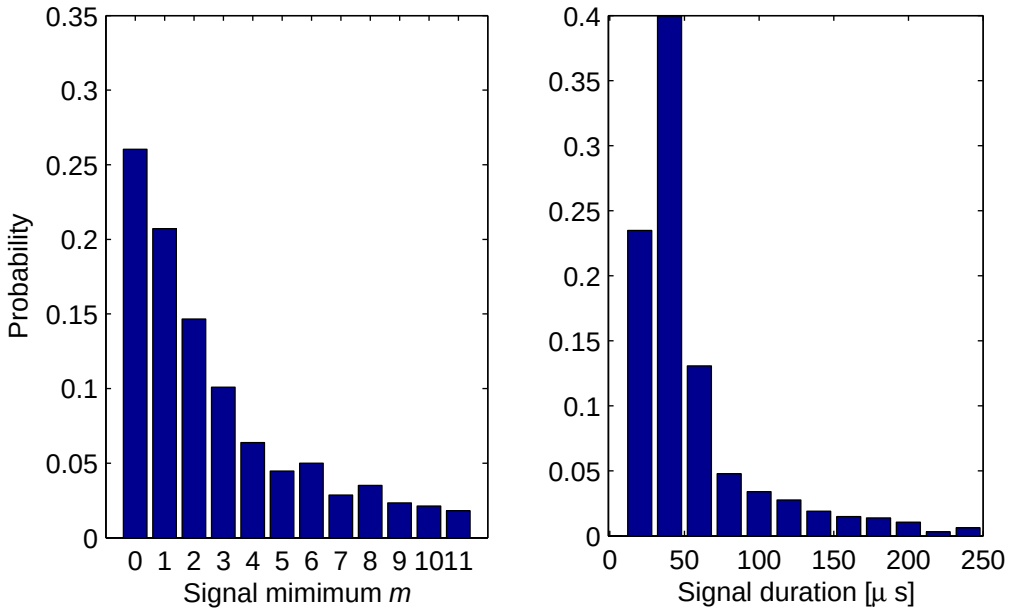

Figure 3.5: Statistics of detection events on a 10ms time window. If the number of detection events in this time window exceeds 40, the experimental run is discarded. Total number of detection events is 1200. The probe power is given by $\Phi_{ref} = 1.5$ MCts/s, and the threshold is set to $n_{thr} = 12$ in a 20μs time bin.
Left: Distribution of the detection signal minima m.
Right: Distribution of the detection signal duration.

3.2.2 Detection efficiency

The detection efficiency (or quantum efficiency) of our cavity-based detection is the probability that a single atom sent into the waveguide induces a transmission dip large enough to be detected. It therefore depends on the detection threshold and integration time we set, which are related to the false detection rate we can accept. To ensure this false detection rate stays negligible, we choose a detection threshold $n_{thr} = 10$ and an integration time such that $n_{ref} = 30$. We can estimate using Poissonian statistics the false detection rate to be about 1 Hz and check it experimentally with a reference experiment without atoms. The detection efficiency also depends on the initial motional state of the atoms: here the atoms enter the cavity with an average velocity of $v_x \simeq 20$mm/s. Their transverse distribution in the waveguide trap is not precisely known, but it is not so critical here given the strong transverse confinement.

The detection efficiency for single atoms is difficult to calibrate since it is not possible to prepare deterministically a single atom running into the cavity mode. A first estimate comes from the comparison between the number of detection events and the number of atoms measured by absorption imaging, which are roughly the same for a given atom preparation. With the large uncertainty attributed to absorption imaging figures, and assuming that atoms are only detected once, this provides a conservative lower bound of about 60 % for the detection efficiency. The main limitation to detection efficiency in a pure magnetic trap comes from transitions from trapped states to un-trapped or anti-trapped Zeeman states. The typical rate of this depumping process is the spontaneous emission rate. This process is quite fast (see Sect. 1.5.1 for theory and Sect.4.5.2 for other experiments) and occurs preferentially in the region of intermediate coupling (for $C \sim 1$). In that case, the atom is rapidly repelled from the waveguide axis before reaching the strong coupling regime, and is consequently not detected. In addition, the atom is also heated up by detection light. This process therefore limits the observed transit time for atoms that are detected (Fig. 3.5 Right).

To investigate these effects, we measure the number of detection events as a function of probe light detuning Δ_a, while keeping the cavity resonant to probe light ($\Delta_c = 0$). The number of atoms measured by absorption imaging is of the order of 200 and fluctuates by about 20% from run to run. The variation of the number of detection events follows then approximately the detection efficiency. Is is measured to be strongly dependent on the choice of the detuning Δ_a, as shown on Fig. 3.6. For blue detuned probe light ($\Delta_a > 0$), the number of detected atoms is extremely small, whereas for

red detuned light, it has a peak-like behaviour near $\Delta_a^{best} = -7\gamma$. This can be interpreted as the effect of the dipole force generated by probe light in the cavity, which attracts the atom towards the strong coupling area for red detunings, independently of m_F value. A similar value ($\Delta_a^{best} = -6\gamma$) was obtained on a very different experimental setup [55].

We can compare the experimental results for the detection efficiency with Monte Carlo simulations of a single atom in a waveguide. All external degrees of freedom are treated classically. Initially, the atom is located outside the cavity mode, at a position $x = -4w$, and moves with a velocity $v_x = 20\text{mm/s}$. Transverse position and velocity are generated randomly from a Gaussian distribution corresponding to a temperature T. We treat the depumping to the Zeeman state the following way: initially, the atom is in the $m_F = 2$ state. At every time step, a random number is generated to determine if the atom is depumped to another Zeeman state according to depumping probabilities, and to which state it is depumped. The atomic motion is then simulated, taking into account the Zeeman state-dependent magnetic force, cavity-light-induced forces and momentum diffusion. Once the trajectory is simulated, the APD output is generated with the knowledge of $g(t)$, and averaged over 20μs time bins like in the experiment. We apply finally the same treatment to the simulated signal to determine the number of detections, which might be 0, 1, or even larger than 1. The comparison with experimental data shows a reasonable agreement on Fig.3.6. Cavity light forces seem to be the most important factor to reach a large detection efficiency, with a broad optimum in the region of red-detunings. With a very abrupt change at $\Delta_a = 0$, any frequency fluctuations of the laser or the cavity in the experiment causes a dramatic decrease of the detection efficiency when Δ_a is chosen near 0. This might explain why the measured optimum is located a bit more red-detuned. The simulated detector response peaks at 0.9 detection events per atom, for the simulation at 1μK. In terms of detection efficiency, the probability to have at least one event is about 75%. An increase of the temperature to 10μK has only a small effect on the detection efficiency.

3.2.3 Double counts

In the experiment, a single atom may enter several times the region of strong coupling, generating a dip of the transmission signal each time. This can happen for example when the atom spends some time in a probe light node near the cavity axis, or when it oscillates with a large amplitude along the vertical axis due to heating. In the simulation, these events are not very frequent as the average number of detection events generated by a single

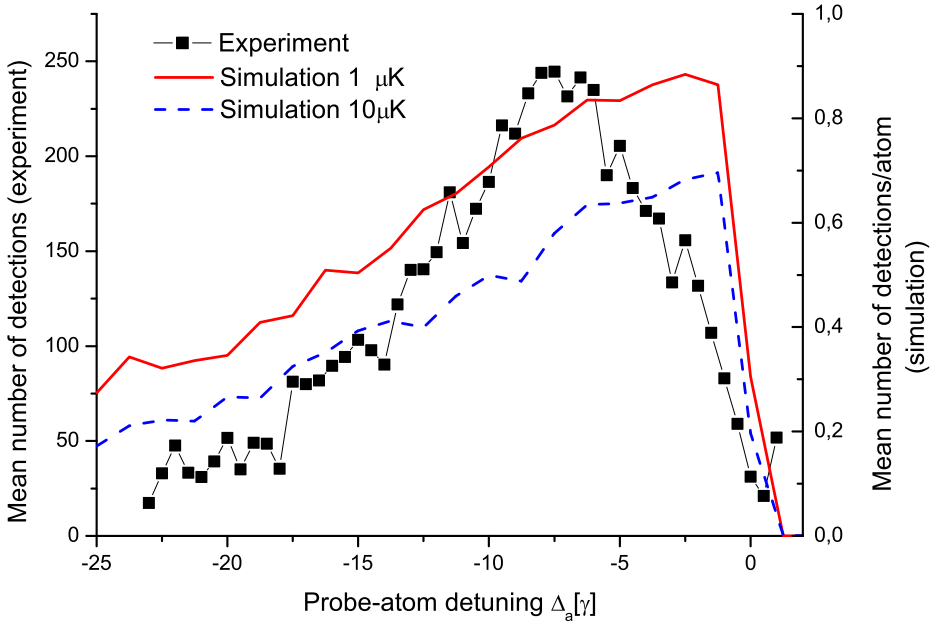

Figure 3.6: Average number of detection events per run, for variable detuning Δ_a. The threshold is set to $n_{thr} = 0.3 n_{ref}$, for $n_{ref} \simeq 30$. In the experiment, n_{ref} fluctuates slightly because of frequency-dependent coupling to optical fibres. The threshold is adjusted to ensure a constant ratio n_{thr}/n_{ref}.
The average atom number according to absorption imaging is about 200. We depict here the number of individual detections events (black curve with markers, left y-axis).
The simulation is performed with a single atom moving in the waveguide with initial velocity $v_x = 20$ mm/s. We plot here the mean number of detection events per atom (right y-axis). For each detuning, the simulation is repeated 1000 times with different initial transverse positions and velocities according to a thermal distribution with temperature $T = 1\mu$K (full red line) or $T = 10\mu$K (dashed blue line).

detected atom is about 1.2. However, these multiple detections are correlated in time, and appear in the transmission traces as successive dips. If the atomic density is low enough, we can distinguish them from other detections by their bunching behaviour. We investigate here the correlation properties of the detection signal. Denoting by t_k the time of the k^{th} detection event (precisely, we choose t_k as the centre of the detection signal $t_k = 1/2(t_{k,1} + t_{k,2})$), we measure the distribution of the waiting times $\delta t = t_{k+1} - t_k$ on a set of 100 runs with a number of detections comprised between 50 and 100.

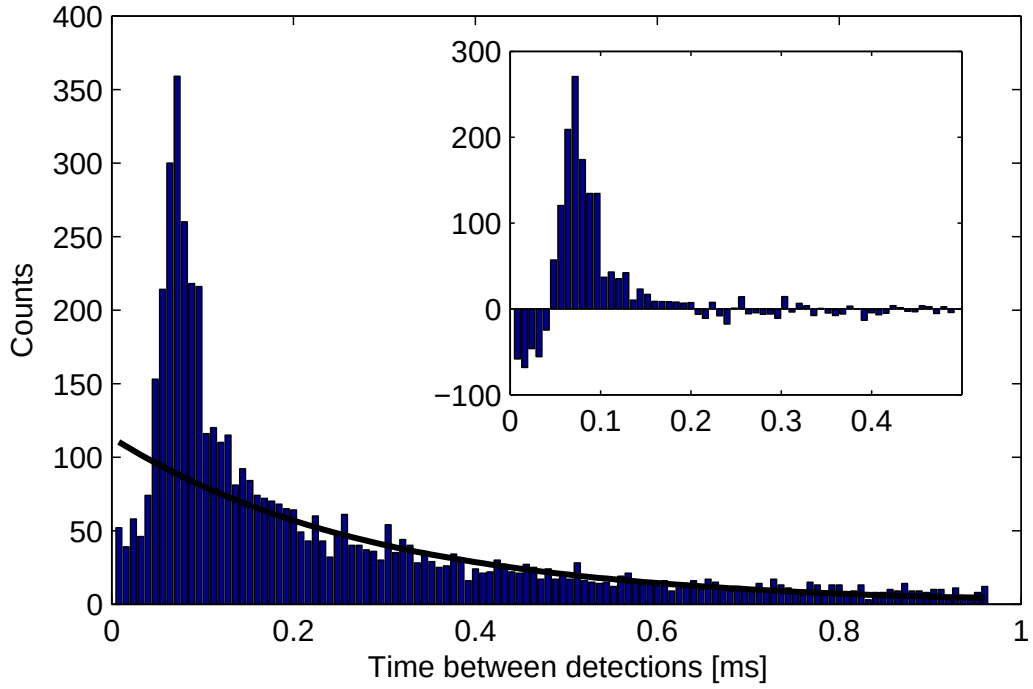

Figure 3.7: Distribution of waiting time δt between successive detections. The average number of detections per run is 70. The solid line is an exponential fit to the distribution for $\delta t > 150\mu$s, with an average waiting time of 300 μs. Inset: fit residuals show missing counts due to atoms transit time, and excess counts due to double detections.

The measured distribution $P(\delta t)$ is compared to the expected exponential distribution for non-correlated atoms detected at a rate Φ:

$$P_{exp}(\delta t) = A \exp(-\Phi \delta t) \tag{3.3}$$

We find a large deviation at short times.

For $\delta t < 50\mu s$, $P \approx 0$ since $50\mu s$ is a typical duration of a detection signal. On the contrary, for $50\mu s < \delta t < 100\mu s$, we have an excess of detections compared to exponential distribution, which we attribute to multiple detections of the same atom. We also find, on this delay timescale, that it is more likely to have $m_2 > m_1$ rather than $m_1 \geq m_2$ (60% vs 40%), where $m_{1,2}$ are the detection signal minima of the two successive events. This is in agreement with some heating which took place during the first detection, or that the atom was for example depumped to the weakly trapped $m_F = 1$ state. The second detection dip is then on average not as deep as the first, and shorter.

In the distribution of the waiting times we can also read the probability of having a double detection: it is simply the probability to observe one of these excess detections for $50\mu s < \delta t < 100\mu s$, instead of seeing the next atom. From the data, we estimated this probability to be about 20%. It is in agreement with the value calculated with the simulation.

From this analysis, we can extract the bandwidth of the detector. The transit duration ($\sim 50\mu$s) and multiple counts define a dead time of the detector of the order of 200μs. Furthermore, we can correct the first estimate of detection efficiency by taking into account multiple detections which artificially increase the number of detections. It decreases the lower bound of the detection efficiency to about 50%.

3.3 Conclusion

The observation of single atom transits reported here provides a direct evidence that our cavity-based detector can detect single atoms. This experiment is the first performed on a atom chip to reach this single atom detection regime. We estimate the detection efficiency to be above 50%. This value is in agreement with numerical simulations. We attribute the missed detections to atoms that are heated up or depumped before reaching the strong coupling regime. The measured optimum detuning $\Delta_a = -7\gamma$ is consistent with this picture, since the light forces generated for red detunings attract the atom to the regions of large coupling.

We can therefore safely claim that atoms located in the strong coupling region are much more likely to be detected with this detector. We expect then a much larger detection efficiency in a configuration where the atoms are independently and tightly trapped in the region of strong coupling. This will be the object of Chap. 4.

Chapter 4

Preparation and detection of trapped single atoms

This chapter contains the most important work of this thesis which is the preparation and detection of single trapped atoms. The introductory section gives the motivations to realize the preparation of trapped single atoms, and reviews the different possible strategies to achieve it, including the one we will pursue. In the second section, we describe the implementation of our strategy to obtain a deterministic preparation of single atoms. In the third section, we characterise our preparation by a lifetime in the dipole trap, and a kinetic energy distribution. In the fourth section, we evaluate with which efficiency we can measure the single atom internal state. Finally the fifth section is devoted to the measurement back-action on the atomic internal state.

4.1 Introduction

4.1.1 A well-controlled system

A single atom inside a high-finesse cavity is the textbook example for an ideal light-matter coupled quantum system [67]. Single atoms of a given chemical species are all identical, with an internal structure fully characterised once and for all. The high-finesse cavity acts as a filter for the electromagnetic field, and in many cases only one mode of the cavity field is coupled to one possible transition of the atom, and the physics of the system is reduced to the ideal Jaynes-Cummings interaction. With such a small number of degrees of freedom, this system can be simulated without any numerical complexity and the results can be precisely compared with the experiment. However,

experimentally, a large uncertainty in the system originates from the positioning of the atom in the cavity mode, since the coupling $g(x)$ changes from its maximum value to zero on a distance $\lambda/2 \sim 0.4\mu$m along the cavity axis, and a few microns (mode radius) transversally. In early CQED experiments, single atoms with a small velocity were randomly sent into the cavity mode, and only those hitting the cavity mode centre were efficiently detected [68]. Using the position-dependence of the coupling to the cavity mode, it was possible to reconstruct the atom trajectory as a trap was switched on upon atom detection [69]. However, most recent CQED experiments intend to bring in single atoms or ultracold clouds using movable traps, in order to achieve deterministic, maximum coupling to the cavity [70, 15, 14]. Moreover, the presence of a trap allows to maintain the atom in the cavity mode for long durations, and use the atom-cavity system as a toolbox for applications.

4.1.2 Different strategies to prepare single atoms

To prepare a single atom in the cavity in an efficient manner, we cannot rely on usual cold-atoms evaporation techniques, both for theoretical reasons (if the atoms do not interact very strongly, the number of atoms at the end of the evaporation ramp fluctuates), and above all for technical reasons (especially noise in the magnetic fields). To overcome this limitation, two possible strategies exist: increasing the interactions between atoms, or applying active feedback on the atom number.

Mott transition

The first strategy requires a lattice, or array of neighbouring traps, and is related to the superfluid-insulator transition (the Mott transition). Increasing the interaction energy between atoms to forbids the presence of two atoms or more in the same trap, and forces them to redistribute equally between all traps. Initial Poissonian fluctuations of the atom number are therefore suppressed. This can be realized in an optical lattice by raising the depth of the lattice, i.e. light intensity. Initially a large number of wells are loaded with a small, but fluctuating atom number, and atoms can easily hop between neighbouring wells. As the lattice depth increases, the atomic wavefunction spread in the trap gets smaller, thereby decreasing the hopping energy J and increasing the two-body interaction energy U. Provided this is done adiabatically and below condensation temperature, the atoms will tend to distribute uniformly over all the lattice wells to stay in the collective lowest energy state. Eventually, all lattice sites are populated with the same atom number, and one can achieve a massive parallel single atom preparation in

thousands of individual traps. This effect was first observed with cold atoms in [71] and subsequently used as a preparation tool for quantum gates in [72]. Let us investigate the feasibility of observing Mott transition in our intracavity 1D dipole trap. Interaction and tunnelling energies U and J can be computed as a function of the trap depth only with a simple band structure calculation, as explained in [73]. The transition occurs for $U/J \sim 12$ in a 1D geometry [74]. For our experimental parameters, the transitions takes place at a trap axial frequency $f_x = 35$kHz and a tunnelling energy $J = h\times 10$ Hz. Whereas this trap frequency lies well inside our experimental range, the main difficulty arises from the low tunnelling energy at the phase transition, which is the typical timescale for the redistribution of the atoms in the different wells. It imposes stringent conditions on the trap stability and noise to ensure adiabatic ramping of the trap on a timescale of 1s. Compared to the 3D case, the interaction energy is smaller due to the weaker transverse confinement (the trap aspect ratio is 1:20), which makes the experiment very challenging with our current experimental setup.

Active feedback on the atom number

A second possibility consists in monitoring the atom population of a small trap during the loading phase, until there is a single atom inside the trap. This was done first in Caltech with a MOT of Cs atoms, using small diameter cooling beams [75]. When optically cooled, each atom typically diffuses ~ 0.1 pW of cooling light, which be can detected efficiently with the help of good collection optics and an avalanche photodetector. When the atom number in the trap changes, the fluorescence signal changes by discrete steps, and one can monitor in real time the actual number of atoms in the trap. This technique was adapted for direct loading of a dipole trap from a MOT [76] or a Zeeman-slowed atomic beam [77]. In the case of a tight, but shallow dipole trap (obtained in this latter experiment by strongly focusing the dipole trap laser beam), the inelastic atomic collisions prevent two atoms to be stored simultaneously in the dipole trap and help to achieve efficient single atom preparation in this experiment.

Our strategy: picking a single atom from a condensate

The strategy pursued in this experiment to prepare single atoms also relies on active feedback on the atom number. The principle is depicted on Fig. 4.1. Initially, a small cloud of atoms in the $|F = 1; m_F = 1\rangle$ hyperfine state (quasi-transparent to the cavity) is placed inside the cavity mode. Weak pulses of resonant microwave are applied to the condensate, randomly transferring

atoms to the $|F = 2; m_F = 0\rangle$ state. The cavity is then used as a detector of $|F = 2\rangle$ atoms, and microwave pulses are repeated until there is a single atom in the $|F = 2\rangle$ state. Compared to other single atom preparations based on atom counting, this experiment is similar in principle but the implementation strongly differs. Instead of being spatially separated, the reservoir and the prepared single atom have different internal states. The reservoir itself is not the background gas in the cell, but an atom cloud with the lowest possible temperature we can achieve, and positioned in the centre of the cavity in a well-defined dipole trap site. The detection process is designed to keep light absorption and emission as low as possible. All these modifications are introduced in order to keep the temperature of prepared single atoms as low as possible.

4.2 Preparation of trapped single atoms

In this section, we describe the experiments we performed to prepare single atoms trapped in the centre of the cavity mode. We will show first how we can prepare the small reservoir of cold atoms in the $|F = 1\rangle$ state required for our preparation strategy. Then we will explain how we can transfer atoms to the $|F = 2\rangle$ state with microwave pulses, and detect them with the cavity. By choosing weak microwave pulses, we prove that we can obtain a reliable and deterministic preparation of single atoms.

4.2.1 Preparation and characterisation of the reservoir

From the condensate to the small reservoir

The preparation of the cold atom reservoir is intended to take place as close as possible to the cavity mode. However, we cannot prepare the condensate right into the cavity mode because of the influence of cavity stabilisation light which generates a dipole trap. Therefore radiofrequency evaporation is performed in a dimple trap generated by currents running in the waveguide wire and in a dimple wire located exactly above the cavity mode, and a magnetic bias field in the xy plane (see Fig. 4.2 Left). The geometry of the trap is similar to the initial trap used in the waveguide experiment, apart from its position. The trap centre lies between the chip surface and the cavity mode, 20 μm above the cavity mode centre (see Fig. 4.2 Right). The trap frequencies are $(f_x; f_\perp) = (270; 4100)$ Hz, with the slow axis parallel to the waveguide and perpendicular to the cavity axis. Radiofrequency evaporation is performed with a 500 ms ramp, and results in a quasi-pure condensate with $N_{at} = 600 - 1000$ atoms in state $|F = 2; m_F = 2\rangle$. Anisotropic expansion

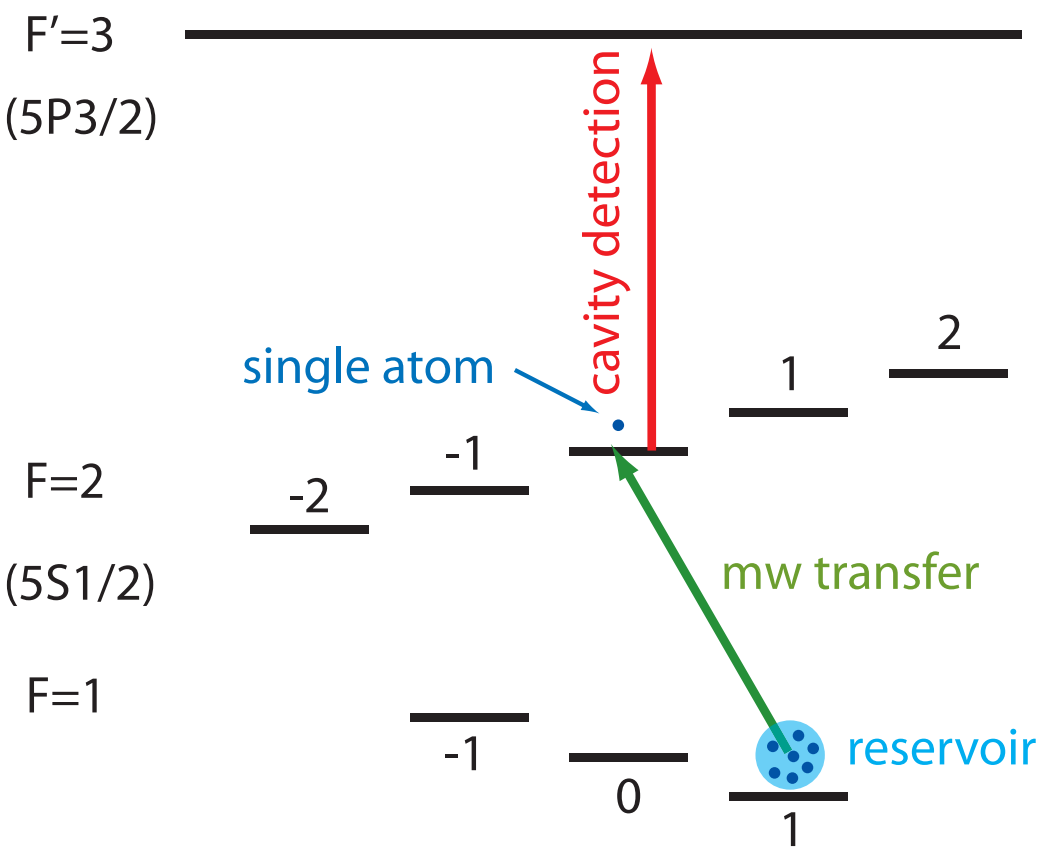

Figure 4.1: Zeeman states involved in the single atom preparation scheme. We start with a reservoir of atoms in the $|F = 1; m_F = 1\rangle$ state. Resonant mw pulses are used to transfer atoms to the state $|F = 2; m_F = 0\rangle$, with a very low efficiency. The cavity, resonant to the $F = 2 \rightarrow F' = 3$ transition, is used to detect if a single atom was transferred to state $|F = 2; m_F = 0\rangle$.

cannot be observed in this configuration, but we can rely on experiments with a rotated trap of similar frequencies to estimate when the condensate appears by measuring its size after time-of-flight expansion.

As we will see later, the ideal atom number for the reservoir is of the order of 10. To reach such a small atom number with a good reproducibility, the best method proved to be surface-evaporation on the fibre tips. Approached to a distance of about 1 μm to the fibre tip, atoms feel a combination of Casimir-Polder and Van der Waals-London forces due to the presence of the dielectric coating and atoms adsorbed on the surface. This leads to an alteration of the trapping potential depicted on Fig. 4.3 Right). Apart from

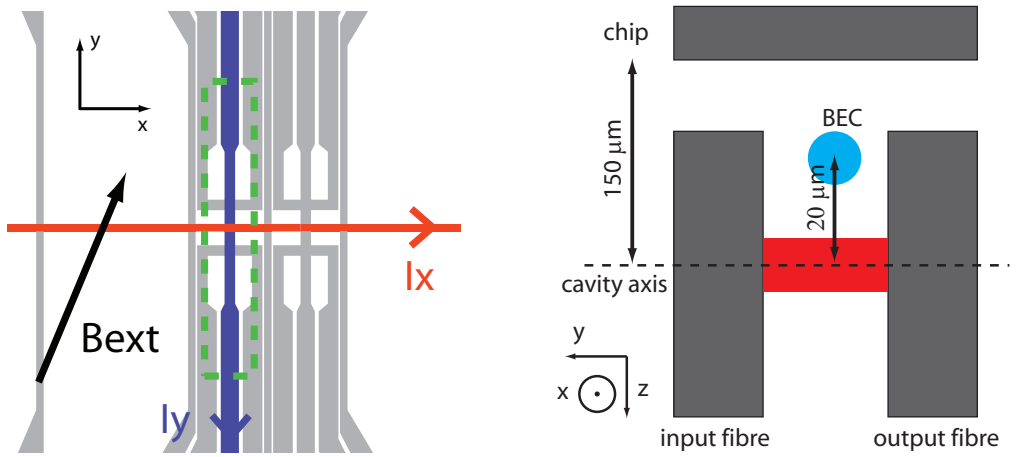

Figure 4.2: Left: Atom chip wires used for the dimple trap. The cavity position is marked.
Right: Initial position of the condensate, 20 μm above the cavity mode.

a slight displacement of the trap centre, and decrease of the trap frequency (measured in [78]), the main effect of the surface interaction is to open up a loss channel on the fibre-side of the magnetic trap, with a tunable energy barrier height depending on the surface-trap separation. Experimentally, the condensate is brought to the desired position for surface-evaporation by ramping the z-component of the magnetic bias field, which translates the trap along the y-direction, see Fig. 4.3 Left. The trap position is kept for 10ms, then the trap is moved back to its initial position. The fraction of remaining atoms changes smoothly from 100% to 0% when the trap-fibre distance changes by 1μm. After surface-evaporation, the cloud size after expansion stays the same and no traces of atoms depumped to other Zeeman states are visible. However, we cannot check experimentally that this still holds for final atom numbers as small as 10, because of imaging limitations at small atom numbers. Compared to decreasing the final evaporation radiofrequency, this technique proved to be more efficient and stable to reach small atom numbers. We obtain routinely atomic clouds of 5-10 atoms with a success rate better than 50%.

Following surface-evaporation, the y-component of the magnetic bias is decreased in a 30ms ramp, which moves the small atom cloud down to the cavity axis. During this ramp, the cavity stabilisation light is switched off. On short timescales, cavity length fluctuations are induced by currents run-

ning in the atomchip wires and are mostly reproducible. By measuring the cavity length variations during that ramp, we can compute the correction voltage we have to apply to the cavity piezo. This procedure allows to keep the cavity resonance frequency within a linewidth during the whole ramp. Once the cloud is positioned in the cavity mode centre, the stabilisation light is switched back on, with a 15ms ramp. It generates a dipole trap for the cloud, with a depth U=2.6 mK and trapping frequencies $(f_y; f_\perp) = (900; 45)$ kHz. The magnetic trap is then disabled on a timescale of 20 ms, and replaced by a constant magnetic bias field of magnitude ∼4G to maintain atom polarisation. In the linearly polarised dipole trap, all states of the ground state $5S_{1/2}$ ground state multiplet feel the same trapping potential, and atoms can be transferred to the $|F = 1; m_F = 1\rangle$ state without losses. This is performed using a resonant microwave π-pulse. We therefore obtain the reservoir of $|F = 1\rangle$ atoms required for our preparation scheme.

Measurement of the reservoir atom number

The preparation of the small atom reservoir cannot be characterised by means of absorption imaging, due to the very low atom number. Since the reservoir is precisely positioned in the cavity mode, we can measure the cavity transmission, tuned to the transition $|F = 2\rangle \rightarrow |F' = 3\rangle$, to estimate the number of non-resonant $|F = 1\rangle$ atoms.

Following the results of Sect. 1.3.2, we know that the effect of $|F = 1\rangle$ atoms on the cavity transmission are equivalent to a shift of the cavity resonance by an amount

$$\delta_c = -N_1 g_1^2/\Delta_{HFS} = -(2\pi)N_1 \times 3.8 \text{ MHz}, \tag{4.1}$$

which gets comparable in magnitude to the linewidth for $N_1 \sim 10$.

If the reservoir population is larger than 15, the transmission level at the position of the initial resonance ($\omega = \omega_c$) drops below 50%, indicating that the reservoir preparation was wrong: either too many atoms in the $|F = 1\rangle$ state, or at least one atom remaining in the $|F = 2\rangle$ state after the microwave pulse. Experimentally, the transmission is measured for every run with a 150μs light pulse, with a reference output rate of 1.5 MCts/s. From the distribution of transmission values (Fig. 4.4 Left), one can extract an estimation of the reservoir atom number distribution (Fig. 4.4 Right). Apart from a peak for $\mathcal{P}(N_1 > 20)$, partly corresponding to remaining $|F = 2\rangle$ atoms, the distribution is similar to a Poissonian distribution with mean value $\langle N_1 \rangle \sim 9 \pm 2$. In particular, in about 50% of the runs, the reservoir atom number lies between 5 and 10, which we consider as a successful reservoir

preparation. Otherwise, we restart the experiment from the beginning and prepare a new reservoir.

4.2.2 Probabilistic transfer of a single atom

Upon successful preparation of the reservoir, we now turn to the preparation of a single atom in the $|F = 2\rangle$ state. To achieve this, we repeatedly try to extract a single atom from the reservoir using a weak mw-pulse to transfer the atom to the $|F = 2; m_F = 0\rangle$ state. Due to the external magnetic bias field, the different Zeeman states are easily resolved (see Fig. 4.1). By tuning the microwave source to the appropriate frequency, one can selectively transfer the atoms to the $|F = 2; m_F = 0\rangle$ state. The key idea for single atom preparation is to transfer inefficiently atoms to this state, using a weak microwave pulse, in order to keep the relative probability for a 2-atom transfer small. The Rabi frequency of this transition is $\Omega_{11\to 20} = 2\pi \times 34 \pm 3$kHz, measured with a large reservoir located at the same position and with the same magnetic bias field (see Sect. 2.3.2). For the weak extraction, we apply a resonant microwave pulse, with a square shape and a duration $t_p = 1.6\mu$s. For each atom in the reservoir, the probability to be transferred is small and given by $p = \sin^2(\Omega t_p/2) \sim 0.03$. After the microwave pulse, we measure if an atom was eventually transferred to the $|F = 2\rangle$ state. For that matter, we switch on the cavity probe light for a duration of $t_{int} = 20\mu$s, with a measured empty cavity transmission count rate Φ_{ref} =1.5 MCts/s, and detunings ($\omega_L = \omega_c = \omega_a + 2\pi\times 100$MHz). This pulse is quasi-resonant to the light-shifted atomic transition. During the detection pulse, photons transmitted through the cavity are detected and counted using the APD, which is connected to a digital counter. The number of detected photons is then compared to a threshold value, which we set to 5 (the reference count number for no atoms in the cavity is 30, with the reservoir this value drops to 15 in the worst case because of the cavity shift). A transmission of 5 photons or less indicates therefore a successful transfer of an atom.

The preparation sequence consists in repeating this pattern "microwave transfer, then atom detection", until the number of detected photons in found to be smaller than the threshold value (see Fig. 4.5). We consider then that the preparation is successful. Since the digital counter is attached to the microcontroller and the cycles involves only digital input/output operations and few calculations, the cycle time is very small, $t_c = 26\mu$s, and can be repeated up to 100 times in a single experimental run.

4.2.3 Analysis of detection pulses

We investigate now the results of the detection pulses in more detail. After each microwave transfer pulse, the number of photons N transmitted through the cavity during the detection pulse of duration $t_{int} = 20\mu$s is recorded with the APD. Collecting the data for 130 experimental runs, and restricting ourselves to the first 15 microwave pulses, we compute the distribution of the number of detected photons N. The histogram shown on Fig. 4.6 has a clearly resolved double-peak structure which are well separated by the threshold value $N_{thr} = 5$.

We perform a fit of the histogram with a bi-Poissonian distribution which separates the contribution of unsuccessful and successful transfers:

$$\mathcal{P}(N) = \eta \mathcal{P}_{\text{Poiss}}(N; \Phi_{ref} t_{int} T) + (1-\eta)\mathcal{P}_{\text{Poiss}}(N; \Phi_{ref} t_{int}), \tag{4.2}$$

where $\eta = N_1 p$ stands for the probability to transfer an atom, and T is the relative transmission corresponding to a successful transfer, compared to the transmission of the cavity with the reservoir inside. The results of the fit give $\eta = 5.6\%$, $T = 1.4\%$ and $\Phi_{ref} = 1.25$ MCts/s.[1]

Compared to the waveguide experiment, we find that single atoms are detected with a much higher efficiency ($>$0.9), since there are no traces in the histograms of badly coupled atoms which lead to shallow dips in the waveguide experiment. The measured relative cavity transmission of 1.4% is in agreement with the theoretical value at this detuning for a single atom with a kinetic energy $\sim 100\mu$K (see Sect. 4.3.2 for the measurement of the temperature, and Sect. 1.4.4 for the expected transmission).

However, the histogram data might be polluted by multiple atoms preparations. Especially, when the atom preparation stops after a small number of microwave pulses, it indicates that the transfer probability was not so small, and that there is a sizeable chance that two atoms were transferred at the same time. To investigate the influence of these events, we compare the histograms of the first 5 mw pulses to those of the last 10 mw pulses. Visually, the histograms are similar. The fits to the bi-Poissonian distribution give the following results:

Pulse index range	Statistics	η	T	Φ_{ref} [MCts/s]
$1 \leq n \leq 5$	570	9.0%	1.4%	1.30
$5 < n \leq 15$	740	3.0%	1.3%	1.20
Alltogether	1310	5.6%	1.4%	1.25

[1] The fitted value for Φ_{ref} differs from the empty cavity value 1.5 MCts/s due to the presence of the reservoir which slightly shifts the cavity resonance.

The transfer efficiency of the first pulses is found to be larger. This is expected, since the existence of the last 10 pulses is conditioned to the failure of the first 5, and indicates that the reservoir atom number is small. In terms of cavity transmission T, the two datasets share approximately the same value $T = 1.4\%$. Since the likelihood of a pair transfer in the first dataset is larger, we can conclude that either single atoms and pairs lead to the same transmission level, or that in both datasets the probability of transferring a pair is smaller than 10%.

4.2.4 Probability of preparing a pair of atoms

The object of this section is to estimate precisely the probability of preparing pairs of atoms when we observe a successful transfer.

Now that we know that single atoms can be detected with a high efficiency, we can analyse the transfer probability of the mw pulses. It is basically characterised by the number n_p of microwave pulses it takes before we detect an atom in $|F = 2\rangle$. Theoretically, after each microwave pulse, atoms from the reservoir are independently transferred to the $|F = 2\rangle$ state with a probability p. The number of transferred atoms N_2 therefore follows a binomial distribution $\mathcal{P}(N_2)$, with a mean value $\langle N_2\rangle = pN_1$, where N_1 is the number of atoms in the reservoir. The measured distribution of n_p can reproduced with a numerical simulation, assuming perfect detection of single atoms (and pairs), a given distribution $\mathcal{P}(N_1)$ for the reservoir atom number and a transfer efficiency p. The results are shown on Fig. 4.7.

The agreement between theory and experiment is good, provided p is set to 0.02 in the simulation (0.03 was expected). This discrepancy can be attributed to an overestimation of the average atom number in the reservoir. Besides, the simulation results only weakly depend on the exact shape of the reservoir distribution.

We can now estimate the probability of preparing pairs instead of single atoms. For a given microwave pulse, the probability of transferring a pair supposing at least one atom is transferred reads:

$$\mathcal{P}_{pair} = \frac{\mathcal{P}(N_2 = 2)}{1 - \mathcal{P}(N_2 = 0)} \sim \frac{N_1 p}{2 + N_1 p} \tag{4.3}$$

An absolute, very conservative upper bound on this probability is obtained by setting $N_1 = 15$ (maximum reservoir atom number) and $p = 0.03$, and gives $\mathcal{P}_{pair}^{max} = 0.18$. A more realistic value can be computed from the results of the simulations, assuming either flat or Poissonian reservoir distribution, and gives $\mathcal{P}_{pair}^{avg} = 0.06$. The probability to obtain three atoms or more can

be estimated in a similar fashion, and is found to be completely negligible ($<$0.5 %).

We can therefore conclude from this section that our preparation scheme allows to prepare trapped single atoms, with a small probability to prepare more than one atom ($<$10%). Furthermore, this error probability could be reduced to a smaller value if we decrease the mw power. This might be relevant for experiments in the future which would require it. Also, we found that the detection efficiency with a 20μs probe pulse was close to unity, with a detection signal allowing to distinguish clearly whether there is one atom or not in the cavity mode.

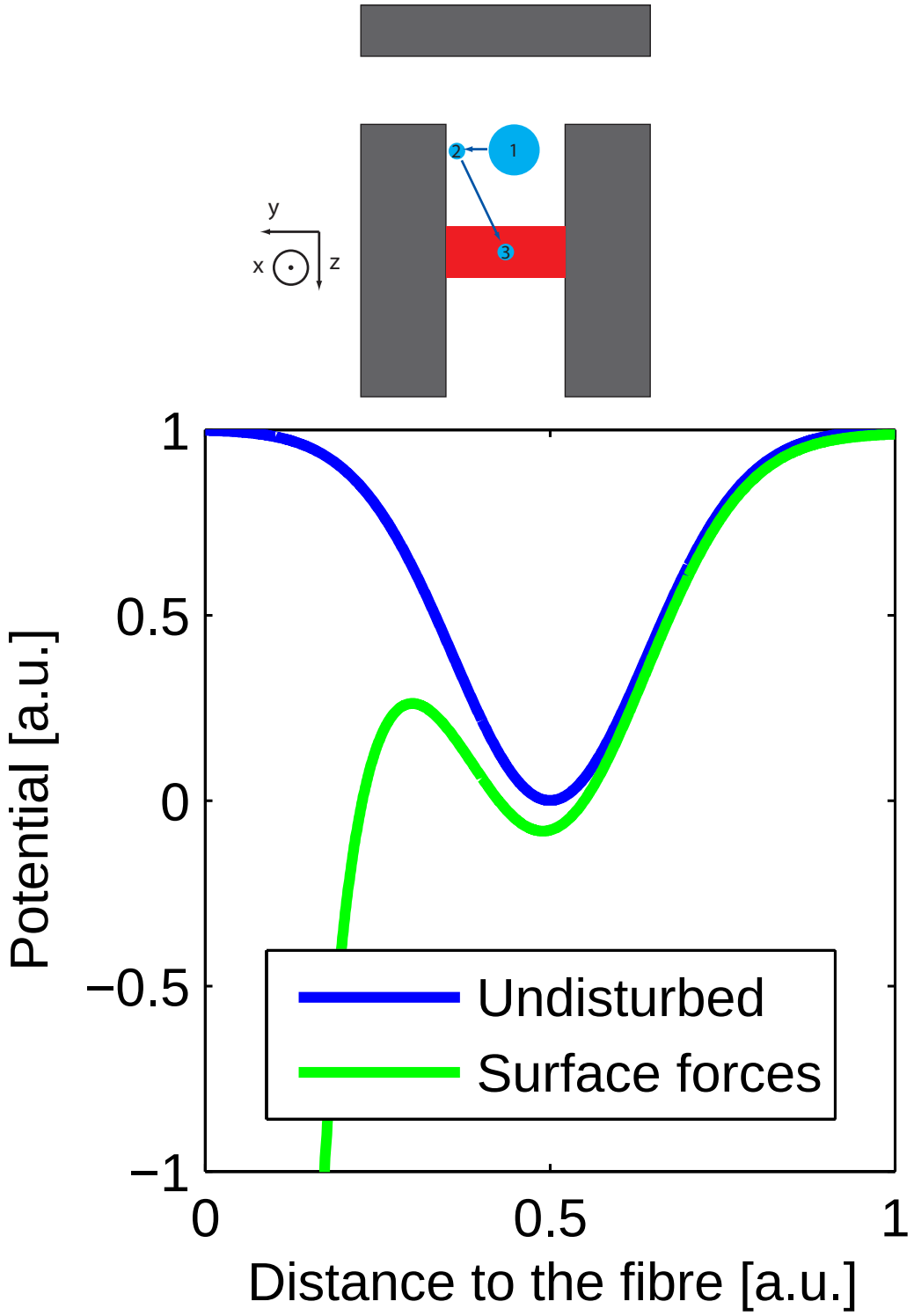

Figure 4.3: Left: Surface evaporation and positioning in the cavity mode. Right: Effect of Van der Waals forces ($V \sim 1/d^3$) on the trapping potential.

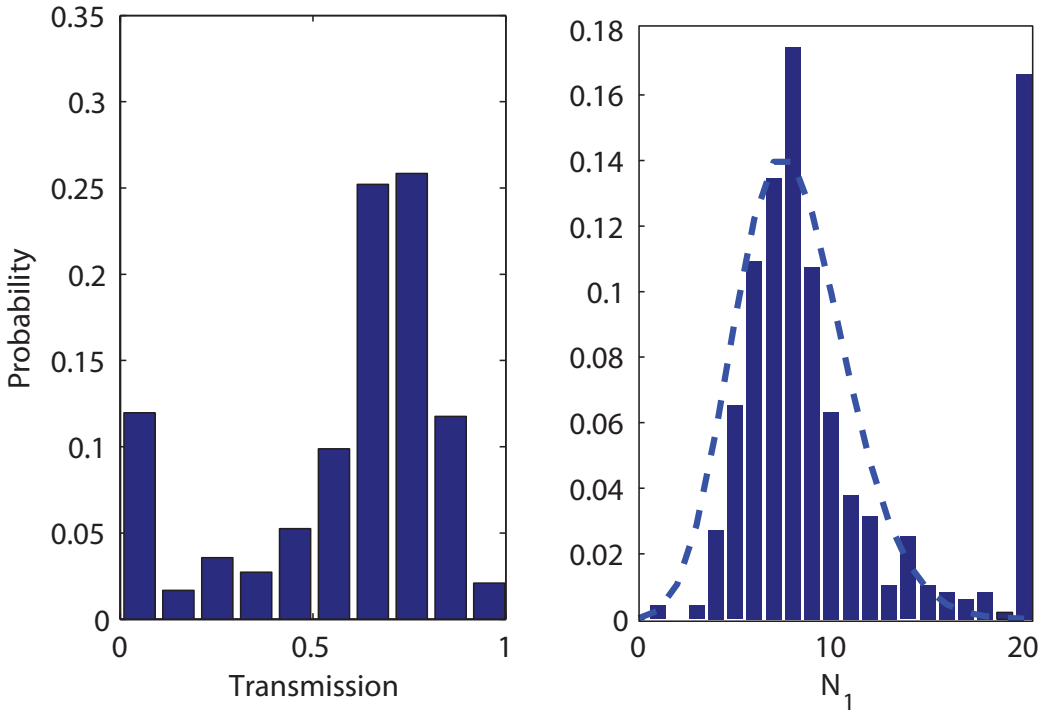

Figure 4.4: Preparation of the $|F = 1\rangle$ reservoir.
Left: Distribution of measured transmission levels following reservoir preparation. The peak at $T_1 = 0$ indicates remaining atoms in $|F = 2\rangle$.
Right: Distribution of reservoir atom number, extracted from the left figure. The dashed line is a Poissonian distribution with $\langle N_1 \rangle$=9.

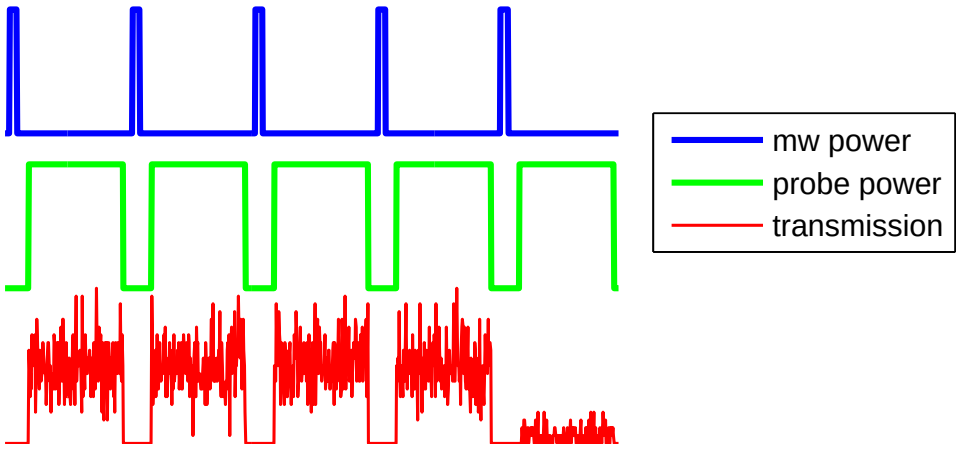

Figure 4.5: Traces of microwave power, cavity probe power, and cavity transmission, used for single atom preparation. In this example, the fifth preparation cycle was successful, and the sequence was therefore stopped.

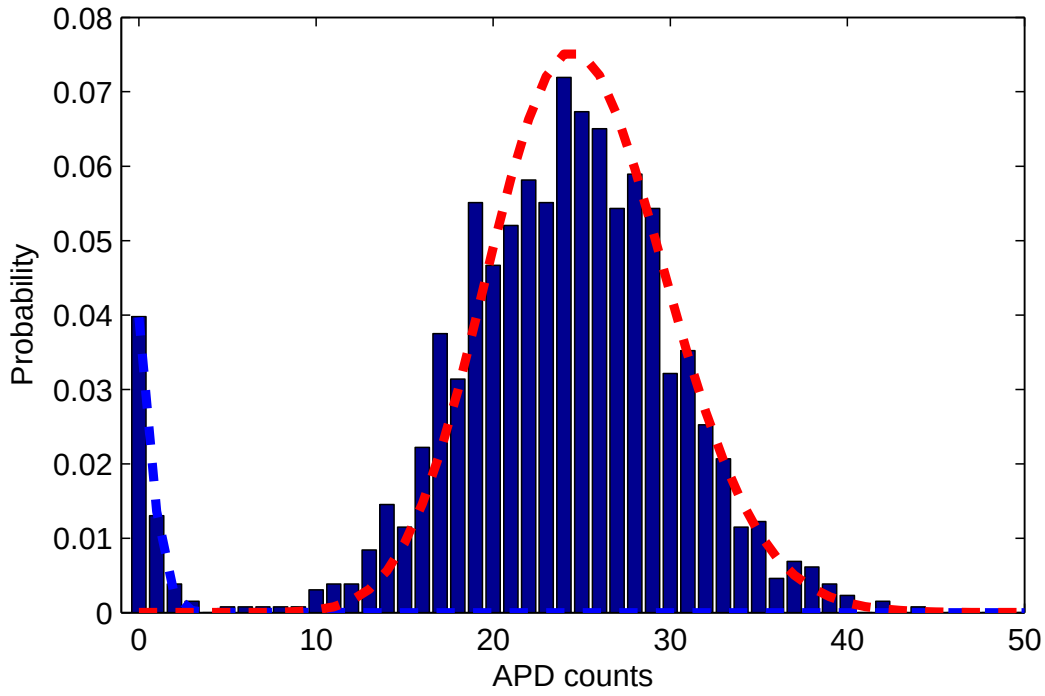

Figure 4.6: Distribution of counts number after each microwave pulse, for the first 15 microwave pulses. Experimental data (bars) is fit to a bi-Poissonian distribution (Eqn.4.2), with the two contributions plotted separately in blue and red dashed lines.

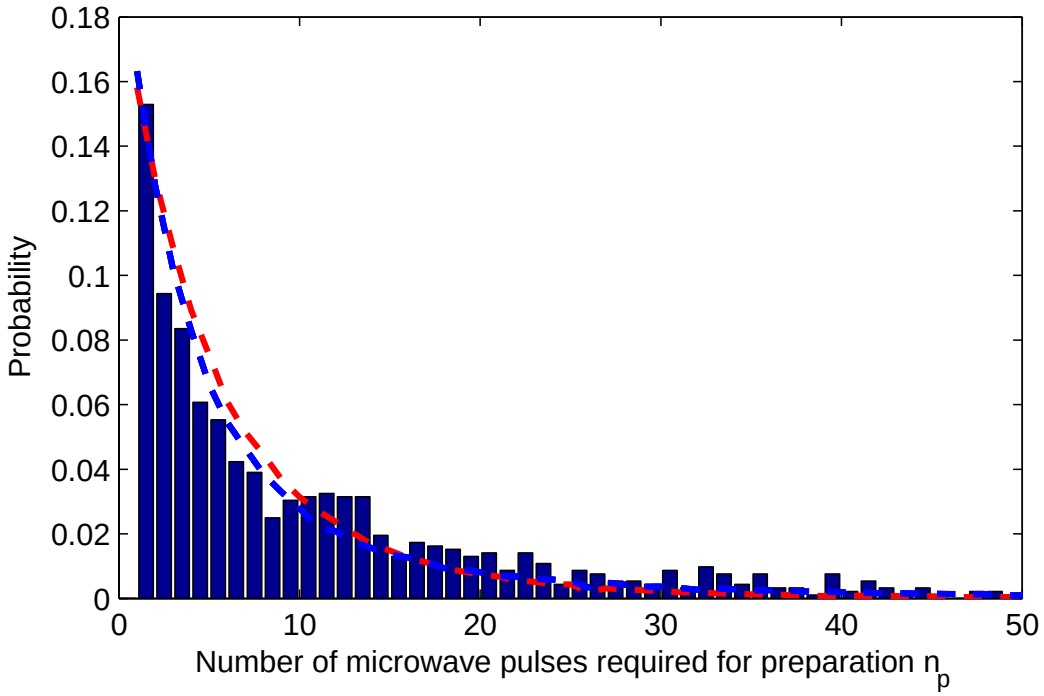

Figure 4.7: Distribution of the number of microwave pulses required to prepare a single atom. The bars are the experimental data for 1.6μs microwave pulses. The lines are the results of the simulation, assuming single atom transfer probability $p = 0.02$. The red line is obtained assuming a Poisson distribution for the reservoir atom number, with $\langle N_1 \rangle = 8$. The blue line assumes a flat atom number distribution between 0 and 15.

4.3 Characterising the atom preparation

Single atoms can be used as a tool for many applications in cavity QED or in other domains. When prepared in the dipole trap, the single atom has a finite lifetime, due to various loss processes. This lifetime limits the complexity of the sequence of manipulations we can perform with a given single atom. The measurement of this lifetime is therefore essential for applications.

We started the preparation with a BEC, aiming for a preparation of single atoms with the lowest possible kinetic energy. A small kinetic energy allows a more precise control on the atom-cavity coupling, which is relevant to applications like single-photon sources, or to the efficiency of cavity detection. Furthermore, some applications such as controlled collisions require a control of the motional state of the atom at the quantum level. We will therefore investigate the energy distribution of trapped single atoms.

4.3.1 Lifetime in the dipole trap

In our experiment, we can attribute losses from the dipole trap without detection light to three possible processes.

The first possible loss process is the collisions with background gas atoms, and is inherent to all cold atoms experiments. In our experiment, the background gas pressure leads to a loss time constant of $\tau_{bg} = 1.4$ s. We measured this time constant with an atomic cloud of about 10,000 atoms in a pure magnetic trap for which collisions with the background gas dominate over 2-body and 3-body collisions between trapped atoms.

A second possible loss channel originates from parametric heating induced by dipole trap fluctuations, and was investigated in earlier cavity QED experiments [79],[80]. Following [81], dipole trap power fluctuations at twice the trap frequency induce an exponential growth of the average atom energy with a time constant

$$\tau_{par} = \left(\pi^2 f_{trap}^2 S[U/\langle U\rangle](2f_{trap})\right)^{-1}, \tag{4.4}$$

where U is the dipole trap depth,f_{trap} its frequency, and $S[.]$ stands for the power spectral density. Due to the quadratic dependance on f_{trap}, parametric heating is probably much stronger in our experiment along the cavity direction, rather than along transverse directions. Unfortunately, we did not try to measure accurately the dipole trap power fluctuations with a MHz-bandwidth.

A last possible heating process is scattering of dipole trap light. Although dipole trap light is far off resonance, the momentum diffusion is enhanced by

the cavity cooperativity factor and lead to a lifetime $\tau_{FORT} = 2$ s (see Sect. 1.4.3).

Experimental determination of the dipole trap lifetime is conceptually simple. Following the single atom preparation, we switch off detection light for a variable duration t_{wait}, then we perform a new atomic detection. The probability to re-detect the atom is simply equal to the survival probability in the dark dipole trap. For each value of the waiting time t_{wait}, we repeat the experiment 40 times. The results, displayed on Fig. 4.8, are consistent with an exponentially distributed lifetime with an average value $\tau_{dark} = 320 \pm 50$ms. This value indicates that the three possible loss processes presented above contribute.

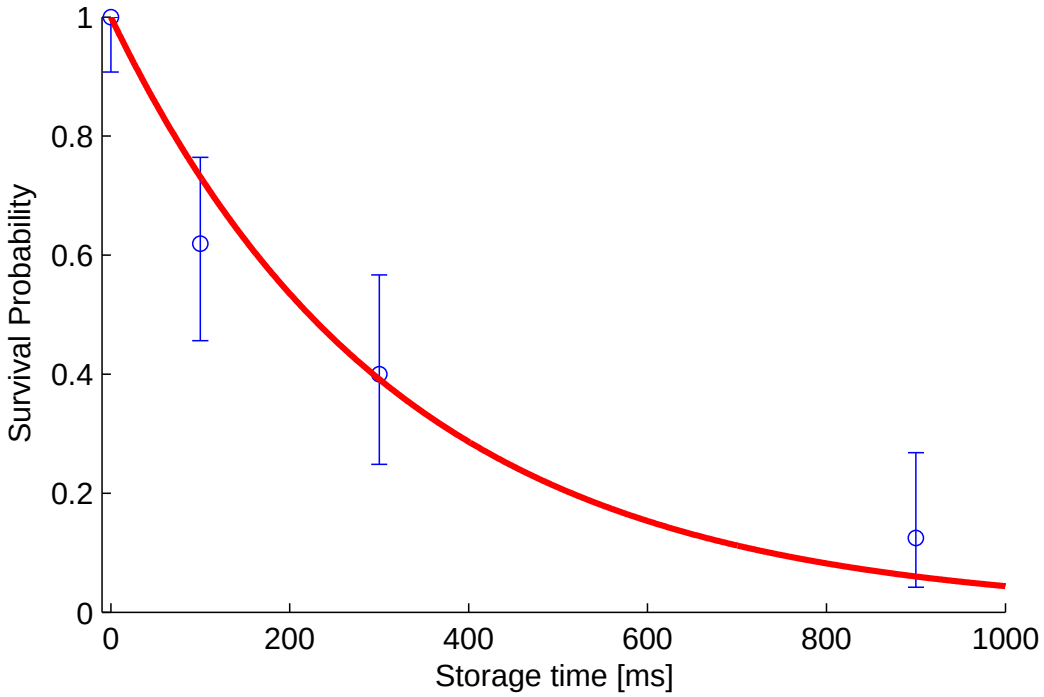

Figure 4.8: Single atom lifetime in the dipole trap. Markers are experimental data, with statistical error bars (70% confidence interval). The full line is an exponential decay fit with $\tau_{dark} = 320$ms.

4.3.2 Single atom energy distribution

As shown in the introduction, the knowledge of the single atom external state is important for many applications. We use a "release and recapture" method

to characterise the energy distribution of a single atom analog to [82] for single atoms trapped in optical tweezers. The principle is the following: after the preparation, we switch off abruptly the dipole trap for a variable duration t_{off}, then switch it back on, and finally perform a new single atom detection after an extra waiting time $t_{wait} = 200\mu$s. During the release phase, the atom moves according to its initial kinetic energy, and when the trap is switched on again, the atom may be retrapped or not depending on its final position. The waiting time before redetection allows to get rid of untrapped atoms before the detection is performed. The probability to recapture in trap decays as the release phase duration increases or the initial energy increases, thereby allowing to reconstruct the initial energy distribution. Results displayed on Fig. 4.9 show that the release-recapture probability decays with two different timescales. On short timescales ($t_{off} \sim 1\mu$s), the atom reaches the potential barrier between neighbouring lattice sites due to its large velocity in the axial direction, and further propagation in the axial direction has no effect on the release-recapture probability. This leads to a plateau at $\mathcal{P}_{RR} \sim 0.85$. For longer timescales ($t_{off} \sim 50\mu$s), the atom leaves the trap in the transverse direction or hits the mirrors, and the recapture probability finally drops to 0. To extract the initial energy distribution from the experimental data, we compare it with a Monte-Carlo simulation based on a classical model for atomic motion. Initial atomic position and velocity are randomly generated according to Boltzmann distribution with temperature T

$$d\mathcal{P}(\mathbf{r},\mathbf{v}) = \mathcal{N}\exp(-\beta U_{dip}(\mathbf{r}))\exp(-\frac{1}{2}\beta m\mathbf{v}^2)d\mathbf{r}d\mathbf{v}, \tag{4.5}$$

where $\mathcal{N}$ is a normalisation constant and $\beta = 1/k_bT$.

During the trap release, the atom position moves at constant velocity $\mathbf{v}$ (we neglect here gravity and possible parasitic forces), and its energy when the trap is switched back on simply reads $E = U_{dip}(\mathbf{r} + \mathbf{v}t_{off}) + \frac{1}{2}m\mathbf{v}^2$. The probability to redetect the atom is given by $\mathcal{P}_{RR} = \mathcal{P}(E < 0)$. Experimental results are in a good agreement with the simulation, and lead to a temperature estimation of $T = 80\pm20\mu$K. We can emit a few comments regarding this observed temperature. First, we can compare it to the BEC transition temperature in the magnetic trap, multiplied by the compression factor between the dipole trap and the magnetic trap. This yields an adiabatic temperature $T_{ad} = T_c \times \overline{\omega_{dip}}/\overline{\omega_{mag}} \sim 0.6\mu\text{K}\times70 \sim 50\mu$K ($\overline{\omega}$ denotes geometric averages of the 3 frequencies). The observed difference can be due to non-adiabatic loading to the dipole trap (adiabatic loading could only be checked for shallower dipole trap due to collision losses), heating during transport or surface evaporation, and heating during detection. We should remark that with this last heating cause, it is certainly not obvious that axial and radial temperature

are equal, since cavity heating is stronger along the cavity axis. The trap is quasi-harmonic and there is no rethermalisation mechanism to redistribute evenly the kinetic energy along all axis. However, experimental data is not accurate enough to perform a two-parameter fit. At last, we notice that the ratio $k_b T/\hbar\omega_x \sim 2$ is too small to neglect external motion quantisation along the cavity axis. The experimental determination of the population of different axial vibrational states would therefore a quantised model, along with more experimental statistics for short timescales. On the contrary, the classical model is certainly valid for the transverse degrees of freedom, and leads to an accurate estimation of the (transverse) temperature.

4.3.3 Summary

We investigated two important properties of our preparation of single atoms: the lifetime in the dipole trap and the temperature. The observed lifetime of 320 ± 50ms is close to the theoretical limit imposed by photon scattering and background gas collisions, and proves that the cavity stabilisation is good enough to ensure a small parametric heating. The measured temperature $T = 80 \pm 20\mu$K is consistent with the measurement of the cavity transmission with a single atom inside. It corresponds to a position uncertainty of $\sigma_y = 15$ nm RMS along the cavity axis, and $\sigma_\perp = 290$ nm RMS in the transverse directions.

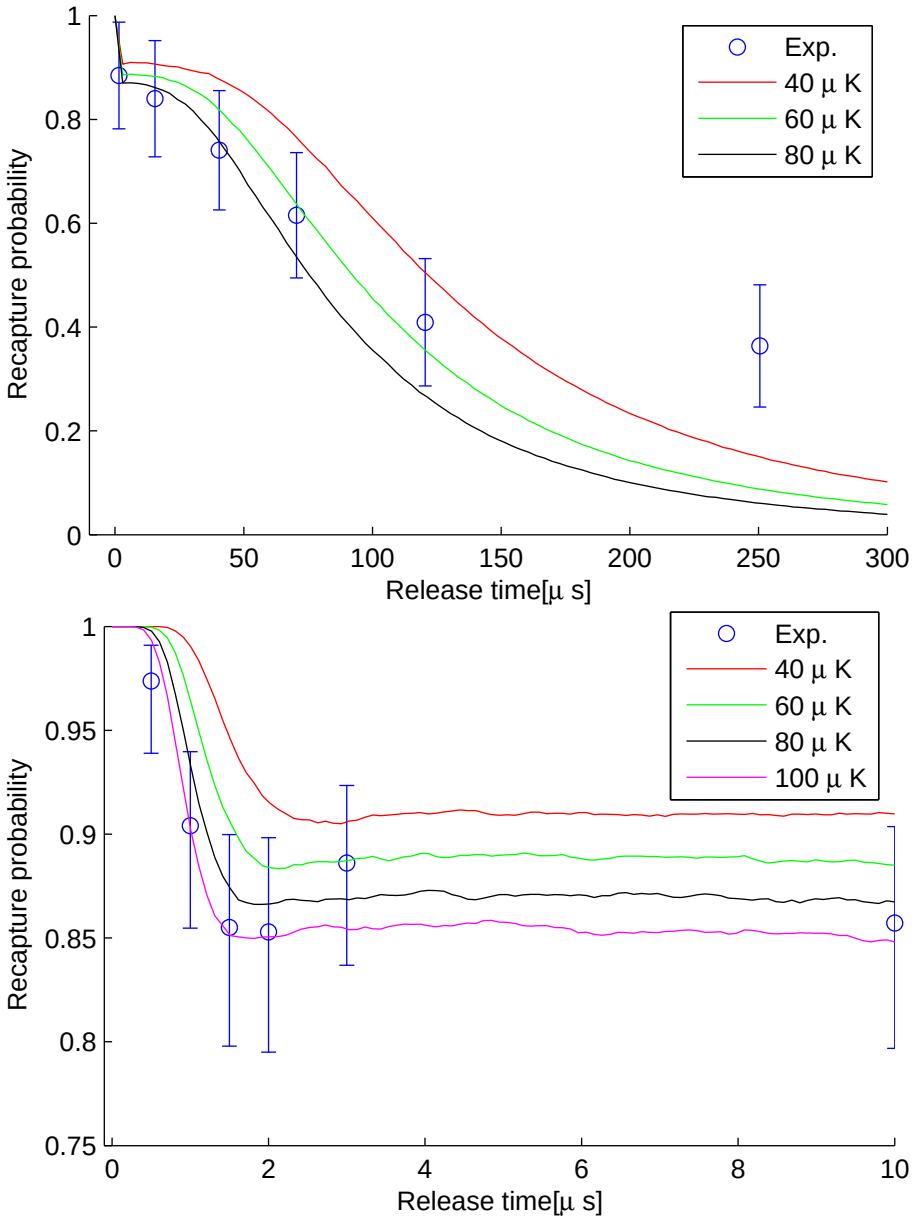

Figure 4.9: Single atom temperature estimation with a release-and-recapture experiment. The release-and-recapture probability is measured for two different timescales, relevant for transverse motion (t_{off} = 0 - 250 μs, upper plot) and axial motion (t_{off} = 0 - 10 μs, lower plot). Error bars are statistical. Experimental data is compared with classical Monte-Carlo simulations, with a set of different temperatures.

4.4 High efficiency single atom detection

We shall describe in this section the detection process. As we have seen in a previous section, a single atom trapped in the cavity mode can be detected with a high efficiency with a short light pulse. In this section, we try to get a precise estimate of the detection efficiency we can reach. The optimum detection efficiency is limited by the amount of time we can switch on detection light without losing the atom. We will start by performing a measurement of this lifetime, which is shortened by the effect of detection light. We will also investigate the exact processes limiting it. From this, we will determine the optimum detection parameters and compute the detection efficiency.

4.4.1 Single atom lifetime during detection

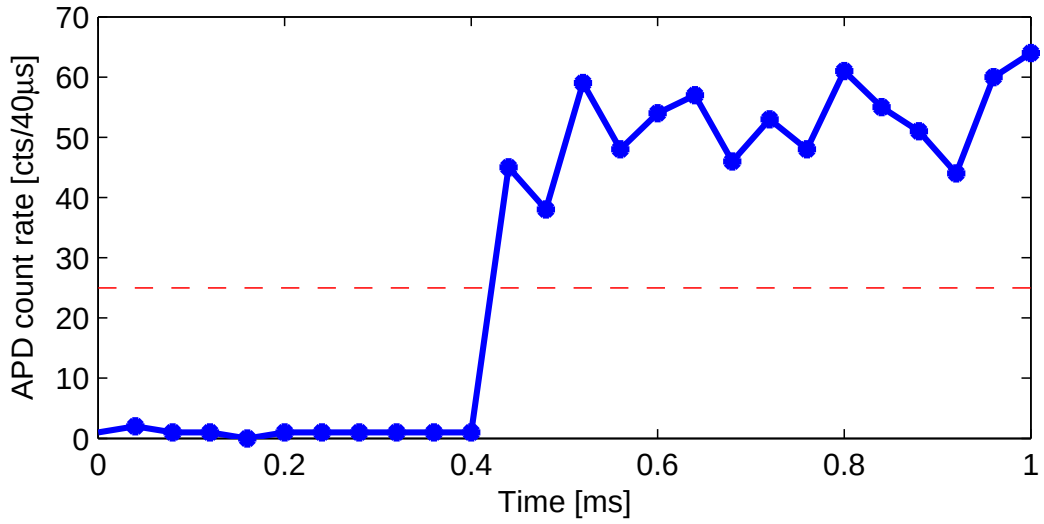

Figure 4.10: Measurement of the detection lifetime for a single experimental run. After the atom preparation, probe light is switched on at $t = 0$ with constant power and detuning. The output photon rate (blue line with circles) is measured with the APD and integrated on 40 μs time bins. The lifetime τ is defined by a transmission threshold (red dashed line) set to 50% of the normal transmission value.

When the atom preparation is successful, the cavity transmission is reduced from its peak value to a small fraction of it (typically a few percent), provided the detuning Δ_a is chosen small enough. If the cavity is continuously probed at constant power right after the atom preparation, the photon

output rate monitored by the photon counter is initially very small and stays at a small level for some time (see Fig. 4.10). Eventually, the output rate returns to its normal, empty-cavity value after a duration τ, which we define as the atom detection lifetime. This finite lifetime is due to absorption and re-emission of probe light photons, and is 2 orders of magnitude shorter than the lifetime in the "dark" dipole trap. A precise definition of the lifetime is given by setting a relative transmission threshold T_{thr} and a signal integration time t_{int}. The atom is said to "leave" the cavity at time τ when the integrated count number $N = \int_{\tau}^{\tau+t_{int}} \Phi dt$ gets larger than the threshold value $N_{thr} = \Phi_{ref} t_{int} T_{thr}$ for the first time. A typical value for the relative transmission threshold is $T_{thr} = 50\%$, and the integration time is set in order to have $\Phi_{ref} t_{int} > 10$ and suppress influence of shot noise on the results. With $\Phi_{ref} \sim 1$ Mcts/s, we can still afford a very good time resolution of about 10 μs. In most experimental runs, the change of transmission is very fast (rise time <10 μs) and the precise values of the threshold and integration time are not critical for the determination of the lifetime.

The distribution of observed lifetimes, measured for $\Phi_{ref} = 1.5$ MCts/s, $\Delta_a = 2\pi \times 160$ MHz, $U_{dip} = k_b \times 2.6$ mK and 110 successful atom preparations, follows approximately an exponential distribution with a mean value $\tau_{det} \equiv \langle \tau \rangle = 1.2$ ms (see Fig. 4.11 Left). During this lifetime, the cavity transmission is reduced on average to about 2.5% of the reference value. It is twice the transmission observed on the first 20 μs, but still very small. We take advantage of this lifetime measurement to confirm that the probability of preparing multiple atoms in the $|F = 2\rangle$ state, instead of single atoms, is small. Although atom ensembles cannot be distinguished optically from single atoms because of the already very low transmission value, their lifetimes are longer since the light intensity in the cavity is smaller and they can scatter more light before being all pumped to the $|F = 1\rangle$ state. As seen before, the likelihood of multiple atoms preparations decreases as the number of required mw pulses increases. In the experiment, the average lifetime shows no visible dependence on the number of mw pulses (See Fig. 4.11 Right). In particular, the average lifetime of the 50 atoms that took at least 10 pulses to be prepared is measured to be 1.4 ms, compared to 1.0 ms for those that took less than 10 pulses. We get therefore a confirmation that the preparation of pairs is unlikely.

4.4.2 Lifetime vs detuning

To get a better understanding of the processes that limit the detection lifetime, we investigate its dependence on the probe-atom detuning Δ_a (see

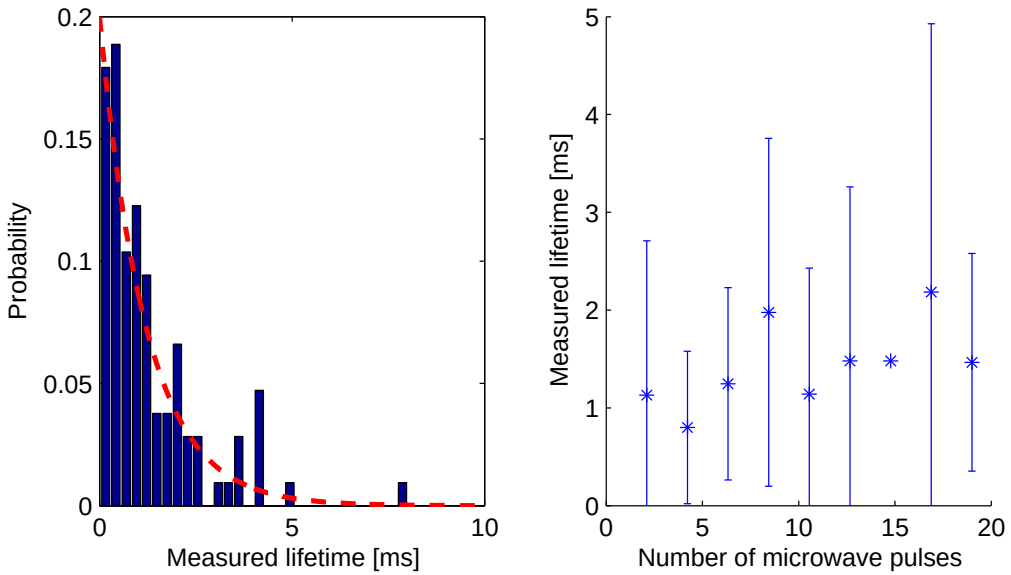

Figure 4.11: Single atom lifetime during detection. Experimental lifetimes are extracted from 110 successful atom preparations, with a cavity light power $\Phi_{ref} = 1.5$ MCts/s and a detuning $\Delta_a = 2\pi \times 160\text{MHz} \simeq 50\gamma$.
Left: Distribution of measured single atom lifetimes (bars). The red, dashed line in an exponential fit with a mean value $\tau_{det} = 1.2$ ms.
Right: Average lifetime dependence on the number of mw pulses cycles required to get the preparation done. The stars represent the mean values, and the error bars two standard deviations. The curve shows no clear increase or decrease.

Fig. 4.12). We find that the average lifetime peaks for a positive detuning $\Delta_a \simeq 50\gamma$, that is, blue-detuned from the estimated maximally light-shifted atomic transition $\Delta_{LS}^{max} \simeq 30\gamma$. A comparison with the calculated depumping time to $|F = 1\rangle$ due to the residual light in the cavity (see Sect. 1.5.2), both in terms of curve shape and order of magnitude, indicates that the lifetime here is limited by this loss process. However, the depumping rate depends on the atom position via the coupling $g(\mathbf{r})$ and the effective detuning $\Delta_{a,eff}(\mathbf{r}) = \Delta_a - \Delta_{LS}(\mathbf{r})$, and the atomic motion has to be taken into account to calculate the instantaneous depumping rate. Therefore, we have performed Monte-Carlo simulations of the atom-cavity system. For each single atom trajectory, the initial atomic position and velocity is randomly generated according to the single atom preparation measured temperature. The atom is initially located in the central antinode of the cavity, corresponding to a maximum coupling to both probe light and dipole trap light. Cavity transmission and depumping rates are calculated once and for all by solving master equation for specific values of g and Δ_a, and interpolated for actual values of $g_{eff}(t)$ and $\Delta_{a,eff}(t)$ encountered on the trajectory. Light forces are calculated using approximate analytical expressions (see Sect. 1.4), taking $g(\mathbf{r}) = g_{eff}(\mathbf{r}) = 0.7 g_m(\mathbf{r})$. The simulation is stopped when either the transmission threshold is reached, or when the atom is depumped to $|F = 1\rangle$. For the detunings we used in the experiment, the depumping is clearly the dominant limiting factor. Results of the experiment and the simulation are in a good qualitative agreement in terms of curve shape and order of magnitude, although the position of the optimum detuning differs by about 20γ. According to the simulation, the optimum detuning should be close to the maximum light shift. This discrepancy is not understood at the moment. However, the depumping to $F = 1$ seems to be the dominant loss term, responsible for the finite lifetime.

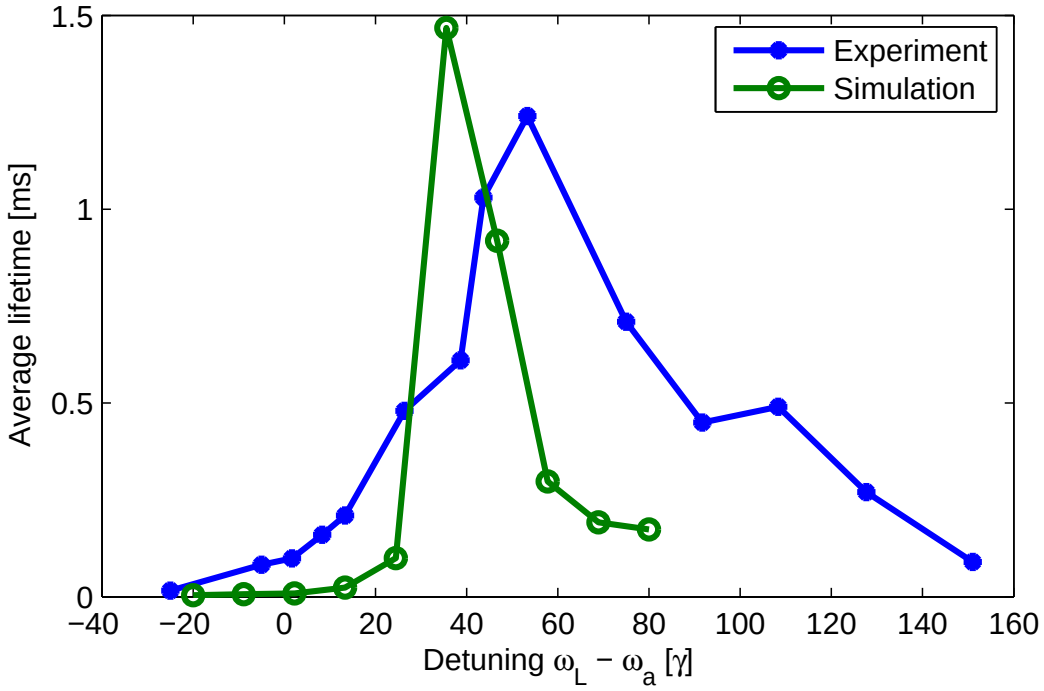

Figure 4.12: Lifetime dependence on probe-atom detuning. Experimental data (blue line with stars) is obtained by repeating successful single atom preparation and lifetime measurement 100 times for each detuning. The probe input power is such that $\Phi_{ref} = 1.5$ MCts/s. The empty cavity is always kept resonant with probe light ($\Delta_c = 0$). Simulation (green line with circles) are performed with matching parameters, except for detunings which are regularly spaced between $\Delta_a = -20\ \gamma$ and $+80\ \gamma$. For each value of the detuning, 100 single atom trajectories are simulated.

4.4.3 Computing detection efficiency

The knowledge of the atom lifetime during detection allows to compute optimum integration time and detection efficiency. In this section we generalise the treatment of Sect. 1.3.3, and find the best integration time to obtain the minimum error probability for the measurement of the atomic hyperfine state.

In this section, we consider the performance of our detection setup operated in a one-shot detection mode. We suppose that a single atom is trapped in the cavity mode, and can be in two possible states[2] $|1\rangle = |F = 2\rangle$ and $|0\rangle = |F = 1\rangle$ with *equal* probability. To determine in which state the system is, we switch on the detection light for a duration t_{int} and detect N photons with the APD. From this measurement, we have to make a guess of the state of the system:$|0\rangle$ or $|1\rangle$? To make the best guess, i.e. to maximise the probability that the guess is true, we have to know the conditional distributions of the output signal N depending on the actual state of the system, denoted by $\mathcal{P}_0(N) \equiv \mathcal{P}(N|0)$ and $P_1(N) \equiv \mathcal{P}(N|1)$. These distributions can be measured by preparing the atom in a well-known state and performing a detection. We assume here that these distributions are well-known.

Suppose we obtain a detection signal N. The probability that the state was $|0\rangle$ is given by Bayes inversion formula

$$\mathcal{P}(0|N) = \frac{\mathcal{P}(0\&N)}{\mathcal{P}(N)} = \frac{\mathcal{P}(N|0)\mathcal{P}(0)}{\mathcal{P}(N|0)\mathcal{P}(0) + \mathcal{P}(N|1)\mathcal{P}(1)} = \frac{\mathcal{P}(N|0)}{\mathcal{P}(N|0) + \mathcal{P}(N|1)}, \tag{4.6}$$

since we have $\mathcal{P}(0) = \mathcal{P}(1)$. Therefore $\mathcal{P}(0|N) > 1/2$ when $\mathcal{P}(N|0) > \mathcal{P}(N|1)$, and we have to make the guess $|0\rangle$ in that case. The probability to make a mistake is then given in general by:

$$\mathcal{P}(\text{error}|N) = \frac{\min(\mathcal{P}(N|0), \mathcal{P}(N|1))}{\mathcal{P}(N|0) + \mathcal{P}(N|1)}. \tag{4.7}$$

Average over all possible measurement outcomes, we obtain the global error probability of the measurement:

$$\mathcal{P}(\text{error}) = \frac{1}{2} \sum_N \min(\mathcal{P}(N|0), \mathcal{P}(N|1)). \tag{4.8}$$

This error probability is then minimised when the conditional distributions have the smallest possible overlap. Detection parameters, such as probe light power, duration t_{int} and the various detunings have to be chosen accordingly.

[2]We use quantum notations for the states, but the theory does not require a quantum system.

In our case, the $|0\rangle$ state is completely equivalent to an empty cavity (a single atom in the $|F=1\rangle$ state detunes the cavity by a tiny fraction of the linewidth, and has nearly no effect on the transmission at $\Delta_c = 0$). The cavity response function is then

$$\mathcal{P}_0(N) = \mathcal{P}_{\text{Poiss}}(N; \Phi_{ref} t_{int}), \tag{4.9}$$

a Poissonian distribution with mean value $\Phi_{ref} t_{int}$.

When the atom is initially in the $|F=2\rangle$ state, the cavity output will differ whether the atom stays in the $|F=2\rangle$ state for a duration longer than the measurement time or not. The cavity output will then be reduced by a factor T for the time the atom spends in the $|F=2\rangle$ state. Assuming an exponential distribution for the lifetime τ, with mean value τ_{det}, we end up with the following expression for $\mathcal{P}_1$:

$$\mathcal{P}_1(N) = \int_0^{t_{int}} \exp\left(-\frac{\tau}{\tau_{det}}\right) \mathcal{P}_1(N|\tau) \frac{d\tau}{\tau_{det}} + \exp\left(-\frac{t_{int}}{\tau_{det}}\right) \mathcal{P}_1(N|\tau > t_{int}), \tag{4.10}$$

where we defined the auxiliary distributions

$$\mathcal{P}_1(N|\tau > t_{int}) = \mathcal{P}_{\text{Poiss}}(N; \Phi_{ref} t_{int} T) \tag{4.11}$$

$$\mathcal{P}_1(N|\tau) = \mathcal{P}_{\text{Poiss}}(N; \Phi_{ref} \tau T + \Phi_{ref}(t_{int} - \tau)) \tag{4.12}$$

With the values measured previously at $\Delta_a = 50\gamma$, we can compute the optimum integration time that leads to a minimum error probability, assuming here that initially the atom has equal probability of being in the $|0\rangle$ or $|1\rangle$ state. The results, displayed on Fig. 4.13 Left, state that the optimum integration time is about 9μs for a detection power of $\Phi_{ref} = 1.5$ MCts/s. The computed error probability is 0.3%. The result is somehow contrary to intuition, since one would expect that taking advantage of a long lifetime would require a longer integration time. In fact, for longer integration times the error probability is dominated by the increasing probability that the atom initially in $|1\rangle$ is depumped during the detection. Should the average lifetime be increased above current value[3], the optimum error probability would decrease approximately as $1/\tau_{det}$.

[3] Or equivalently, the detection rate Φ_{ref} could be increased while keeping the average lifetime constant: in fact, only the product $\Phi_{ref} \times \tau_{det}$ is relevant in the determination of the detector performance. This could be done by decreasing the optical losses at the output mirror of the cavity, using HR coatings with lower losses.

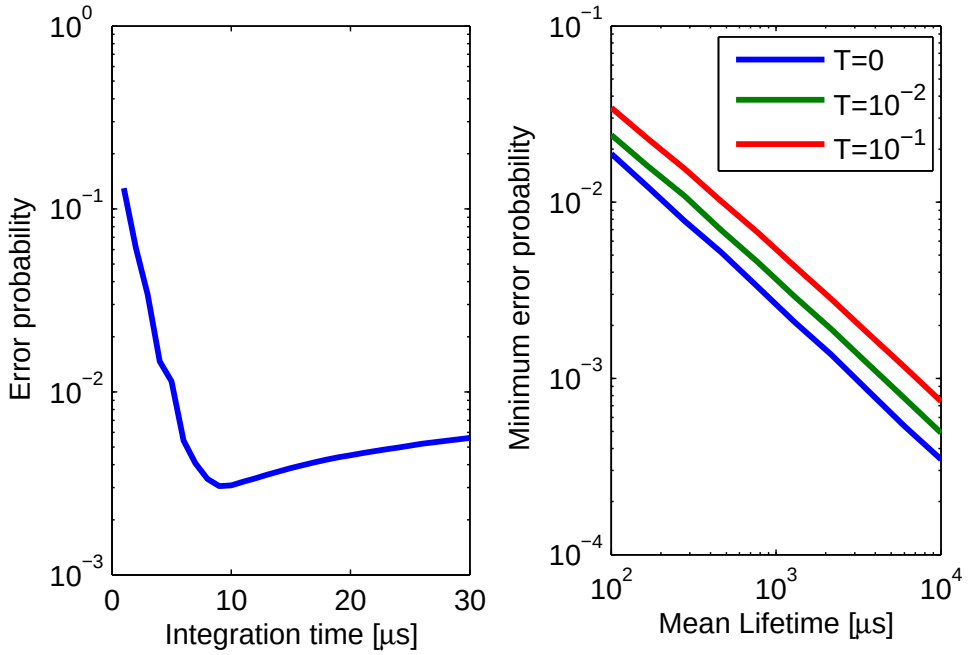

Figure 4.13: Optimisation of the integration time for single atom detection. Left: Detection error probability as a function of integration time. Parameters are those measured for $\Delta_a = 50\gamma$: $\Phi_{ref} = 1.5$ MCts/s, $T = 0.025$, $\tau_{det} = 1.2$ ms.
Right: We plot here the error probability assuming different parameters, after optimisation of the integration time.

We have demonstrated in this section that our detector can reach extremely high detection efficiencies, with an error probability estimated at 0.3% for optimum parameters. We have also seen that the main limitation is the depumping to $|F = 1\rangle$ states.

4.5 Towards a perturbation-free measurement

In the experiment, the use of a cavity for detection purposes is not only intended to achieve a large detection efficiency (free space detectors can reach sensitivity levels that enable single atom counting), but also to minimise the measurement backaction on the atomic properties which we do not measure, namely the Zeeman state and the external state. In this section, we will investigate the measurement back-action on the detected atoms, and to determine to which extent this measurement approaches an ideal measurement.

4.5.1 QND and ideal quantum measurements

The singularity of quantum theory mainly lies behind Heisenberg's uncertainty principle: for each quantum system, there is (at least) a pair of physical properties a and b than cannot be measured simultaneously. For example, if we perform a measurement of a and find the result $a = a_1$, then a measurement of b and find $b = b_1$, a new measurement of a might give a different value $a = a_2 \neq a_1$. However, if we do not perform the measurement of b, a second, immediate measurement of a gives the result $a = a_2 = a_1$ with certainty. In other words, the measurement of b perturbs the system and rules out the prediction we could have made on it. Quantum mechanics theory was developed to account for this peculiarity, and it turned out to be exempt from any failures until now. In its modern formulation, the state of the system is described by a single, normalised vector Ψ in a Hilbert space $\mathcal{H}$, and system variables a,b, ... are described by linear hermitian operators $\hat{a}$, $\hat{b}$, ... For a measurement of the variable a, the probability of getting the outcome a_1 is given by Born's rule $\mathcal{P}(a_1) = |\mathbb{P}(a_1)\Psi|^2$, where $\mathbb{P}(a_1)$ is the projector on the subspace $\ker(\hat{a} - a_1)$. Following this measurement, the state of the system is changed to $\Psi' = \mathbb{P}(a_1)\Psi/|\mathbb{P}(a_1)\Psi|$, which lies in the subspace $\ker(\hat{a} - a_1\hat{1})$. This projection postulate ensures that any repeated measurement of the same variable a will always give the same result.

Experimentally, ideal measurements are difficult to achieve on quantum systems, since it is challenging to couple a microscopic system to a macroscopic system (the *metre*) without disturbing or destroying it. In fact, a measurement process that satisfies the repeatability criterion is already an important achievement in quantum mechanics. It is called a Quantum-Non-Demolition (QND) measurement [83, 84]. The first QND measurements on simple quantum systems were performed on the internal structure of trapped ions with the technique of electron shelving [85, 86, 87]. Later, a lot of experimental work was focused on QND measurement of light fields, aiming to "see

a photon without destroying it" by coupling it dispersively with an atomic sample [88, 89]. In the last two decades, huge progress was made, enabling the possibility to measure a single photon 500 times without losing it [28, 90]. Currently, experiments are focused on QND measurements of new quantum systems for quantum information (quantum dots [91], superconducting circuits [92, 93]). A second important goal is to achieve preparation of pure quantum states by measuring a system initially in a classical mixture of possible quantum states, and projecting it in a particular quantum state. This way, one can achieve the preparation of Fock states [94], or Schroedinger cat states [95]. For atomic ensembles samples, the preparation of spin-squeezed (entangled) states in a major goal since these states have applications in interferometers and clocks [96, 97]. By combining QND measurements and feedback, the preparation can be made deterministic [98, 99].

An ideal measurement is only an example of a possible QND measurement. The difference between an ideal and a QND measurement is the measurement backaction on other variables of the system. Let a and b be two *commuting* variables, and consider the measurement sequence a, b, a. After the first measurement with the outcome $a = a_1$, Ψ is projected to the subspace $\ker(\hat{a} - a_1\hat{1})$. Since $\ker(\hat{a} - a_1\hat{1})$ is stable for $\hat{b}$, it is also stable for the projection mapping $\Psi \rightarrow \Psi' = \mathbb{P}(b_1)\Psi/|\mathbb{P}(b_1)\Psi|$ consequent to the measurement of $b = b_1$. Therefore, $\Psi' \in \ker(\hat{a} - a_1\hat{1})$ and the last measurement of a outputs $a_2 = a_1$. For a QND measurement, the mapping $\Psi \rightarrow \Psi'$ does not necessarily commute with $\hat{a}$, and the last measurement outcome is not predetermined.

In the experiment presented in the previous section, our measurement of the single atom internal structure is QND since the measured observable F can be measured repeatedly about 100 times ($\tau_{det} \sim 100 t_{int}^{best}$) before its value changes. However, the state of the system is described by the knowledge of the *complete set of commuting variables* (F, m_F, n_x^{vib}, n_y^{vib}, n_z^{vib}), all of which commute with the Hamiltonian and can be in principle measured simultaneously. In this section, we will investigate how we can measure the m_F value, and to which extent the backaction perturbs the atomic external state described by the triplet of variables (n_x^{vib}, n_y^{vib}, n_z^{vib}).

4.5.2 Measurement of Zeeman diffusion

When the atom-cavity system is probed with quasi-resonant light, absorption and re-emission of cavity photons induce fast dynamics in the Zeeman level structure. For a cavity probe power corresponding to a reference output rate

of $\Phi_{ref} = 1$ MCts/s, the typical timescale of the Zeeman diffusion is of the order of 5 μs, according to calculations of Sect. 1.5.1. We describe here an experiment which allows to measure this diffusion rate.

Preparation of specific Zeeman states

To measure the diffusion rate, we first need to prepare the atom in a well defined Zeeman state.

Detection pulses used in our preparation and detection scheme, with a duration longer than 10μs, lead to a large redistribution in the different m_F states when the single atom is in the $|F = 2\rangle$ hyperfine state. On the contrary, an atom in the $|F = 1\rangle$ state scatters no light, and its Zeeman state is preserved. We can therefore imagine a preparation scheme which relies on this property:

1. We prepare a single atom in the $|F = 2\rangle$ state as described in Section 4.2.

2. We apply a microwave π pulse resonant to the $|F = 2; m_F = 0\rangle \rightarrow |F = 1; m_F = 0\rangle$ transition. The microwave power is chosen low enough to ensure that atoms in the $|F = 2; m_F \neq 0\rangle$ are not transferred to any $|F = 1\rangle$ state[4]. At that step, the single atom internal state is either $|F = 2; m_F \neq 0\rangle$ or $|F = 1; m_F = 0\rangle$.

3. We perform a new measurement of F. If we find that the atom is in the $|F = 1\rangle$ state, we know for sure that it is the $m_F = 0$ Zeeman state. Otherwise, it can be in any $|F = 2\rangle$ state, and we restart from step 2.

4. The single atom is in the $|F = 1; m_F = 0\rangle$ state. We can transfer it back to $|F = 2; m_F = 0\rangle$ with another π-pulse.

Measurement of specific Zeeman states

With similar ideas in mind, one can design measurement schemes that are sensitive to the Zeeman sublevel by combining two measurements of F (denoted by the symbol F_i) with resonant microwave pulses on the clock transition $|F = 2; m_F = 0\rangle \rightarrow |F = 1; m_F = 0\rangle$ (denoted by the symbol π). In the experiments, we use the schemes $\pi - F_1 - \pi - F_2$ and $F_1 - \pi - F_2$, with the following truth tables:

[4]For a non-resonant Rabi oscillation between ground states, the transfer probability is of the order of $\Omega_{Rabi}^2/\Delta^2 \sim 10^{-2}$, when the detuning $\Delta \sim 1$ MHz is induced by a magnetic field bias of a few Gauss.

Scheme: $\pi - F_1 - \pi - F_2$	Results	
State	F_1	F_2
$\|F=2; m_F=0\rangle$	1	2
$\|F=2; m_F\neq 0\rangle$ or $\|F=1; m_F=0\rangle$	2	any
$\|F=1; m_F\neq 0\rangle$	1	1

Scheme: $F_1 - \pi - F_2$	Results	
State	F_1	F_2
$\|F=1; m_F=0\rangle$	1	2
$\|F=2; m_F\rangle$	2	any
$\|F=1; m_F\neq 0\rangle$	1	1

With the measurement scheme $\pi-F_1-\pi-F_2$, we can therefore distinguish the specific Zeeman state $|F=2; m_F=0\rangle$ from other $|F=2\rangle$ states.

Measurement of Zeeman diffusion

With the preparation and detection scheme described above, we are now able to investigate the depumping effects caused by detection light. Experimentally, we prepare a single atom in the $|F=2; m_F=0\rangle$ state. Then we apply a low power resonant light pulse ($\Phi_{ref}=100$ kCts/s) with a variable duration t_p which induces diffusion in the Zeeman levels of the $|F=2\rangle$ hyperfine state. We measure the effect of this perturbation pulse by performing a $\pi-F_1-\pi-F_2$ detection scheme. If the detection results are $(F_1=1; F_2=2)$, the atom stayed in the $m_F=0$ state. Otherwise, we usually obtain $(F_1=2)$, which indicates that the atom was depumped out of $m_F=0$ during the perturbation pulse. The last possible result $(F_1=1; F_2=1)$, indicating that the atom is either lost or depumped to $|F=1\rangle$, is very unlikely and corresponding events are ignored. In a single experimental shot, the same atom is recycled up to 20 times to increase the statistics. For each value of the duration t_p, we average over 50 successful preparations and detections to obtain the probability $\mathcal{P}_{m_F=0}$. From the experimental results, displayed on Fig. 4.14, it is found to decay as:

$$\mathcal{P}_{m_F=0}(t_p) = \mathcal{P}^{ss}_{m_F=0} + (1-\mathcal{P}^{ss}_{m_F=0})\exp(-t_p\Gamma_Z), \tag{4.13}$$

where $\mathcal{P}^{ss}_{m_F=0}=0.25\pm0.05$ is the steady state value of $\mathcal{P}_{m_F=0}$ (optical pumping Zeeman distribution) and $\Gamma_Z=30\pm5$ kHz is the observed decay rate. The experiment was performed at $\Delta_a=30\gamma$ and $\Delta_a=50\gamma$ and lead to very similar results.

The initial depumping rate $\Gamma^{exp}_{depump}=-d\mathcal{P}_{m_F=0}/dt_p|_{t_p=0}=(1-\mathcal{P}^{ss}_{m_F=0})\Gamma_Z=22\pm5$ kHz and the steady state value $\mathcal{P}^{ss}_{m_F=0}=0.25\pm0.05$ can be compared

with the theoretical values calculated in Sect. 1.5.1. Both depend on the angle θ between the external magnetic field (which is perpendicular to the cavity axis) and the polarisation in the cavity, which we cannot measure independently. For $\theta = 0$ (π polarisation), we expect an initial depumping rate of $\Gamma^{\pi}_{depump} = 3.5$ kHz and a steady state population of 51% in the $|m_F = 0\rangle$ state. For $\theta = \pi/2$, we expect a depumping rate of $\Gamma^{\sigma^+\sigma^-}_{depump}$ =15kHz and a steady steady population of 1%. For intermediate angles, the expected values lie in between. We therefore find that the experimental value for the depumping rate is larger than we expected, by a factor of at least 2. A possible explanation is that the output losses of the cavity are underestimated, and that the intracavity light intensity is larger than what we expect from the coating specifications and the measured finesse.

We investigated the dependence on the cavity polarisation by measuring the steady state value $\mathcal{P}^{ss}_{m_F=0}$ for different angles of the magnetic field, but found no evidence of an increase of $\mathcal{P}^{ss}_{m_F=0}$ for a specific orientation which would correspond to the cavity polarisation. Nevertheless, this experiment provides a direct measurement of the Zeeman diffusion. With a diffusion rate of 22 ± 5 kHz at a reference power of $\Phi_{ref} = 100$ kCts/s, we can perform a measurement with a 10μs light pulse which depumps the atom to $m_F \neq 0$ with a probability of 20%, and has an error probability of about 20%. The error probability could be made smaller by observing both the cavity transmission and reflection.

4.5.3 Estimation of backaction on the external state

Since the depumping rate to the Zeeman states is proportional to spontaneous emission, we can see the Zeeman diffusion as an experimental measurement of the spontaneous emission rate. We are then able to compute the average mechanical energy increase induced by the measurement backaction, with the help of the theory of Sect. 1.4.3. The momentum diffusion coefficients are averaged over a Boltzmann position distribution at $T = 100\mu$K, corresponding to the measured atom temperature, and for $\Delta_a = 50\gamma$. We correct these formulaes by the worst-case factor $\Gamma^{exp}_{depump}/\Gamma^{\pi}_{depump} \sim 5$, where Γ^{exp}_{depump} is the measured Zeeman diffusion rate and Γ^{π}_{depump} the theoretical one. Written in terms of vibrational quantum numbers $n_{x,y,z}$, the estimated heating rates are $dn_y/dt < 250$ quanta/s and $dn_x/dt = dn_z/dt < 1750$ quanta/s, for a probe power of $\Phi_{ref} = 100$ kCts/s. We can therefore perform a very efficient detection of 10 signal-photons (100μs) without a significant change of the external state: $\langle \Delta n_y \rangle < 0.025$ and $\langle \Delta n_x \rangle = \langle \Delta n_z \rangle < 0.175$.

The figure of merit of the detector is then summarised on Fig. 4.15, which

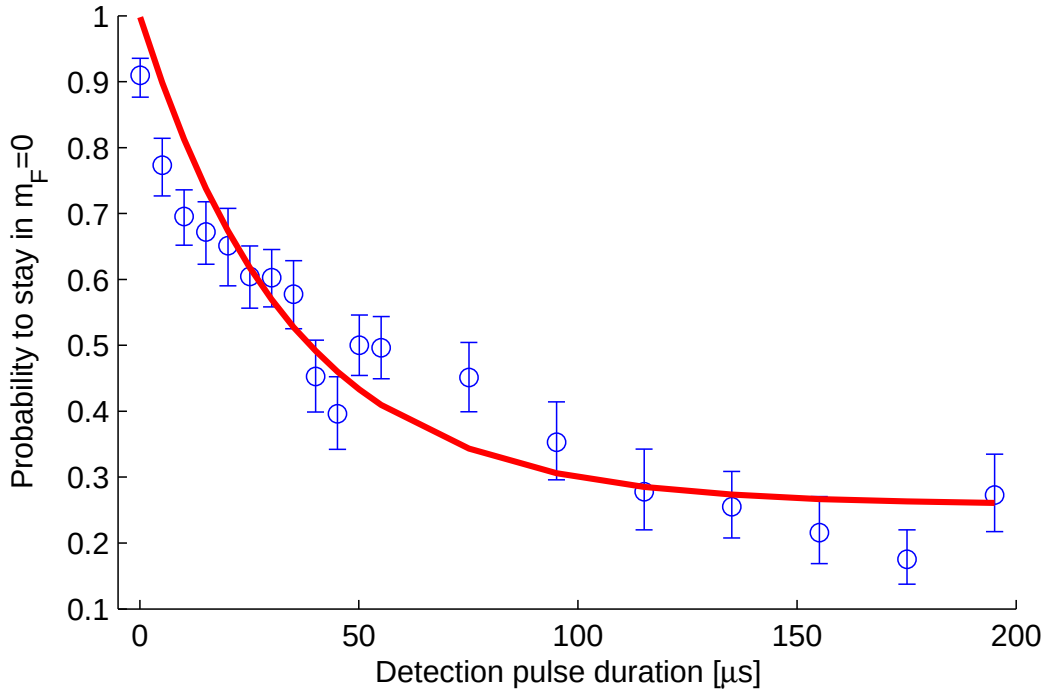

Figure 4.14: Zeeman state diffusion induced by the measurement process. The probability to stay in the initial Zeeman state $|m_F = 0\rangle$ is depicted as a function of the detection pulse duration, for a probe light power of $\Phi_{ref} = 100$ kCts/s and a light-atom detuning $\Delta_a = 30\gamma$. Experimental data is plot in blue, with statistical error bars. The red line is the result from the exponential decay fit.

shows the backaction effects on all atomic variables.

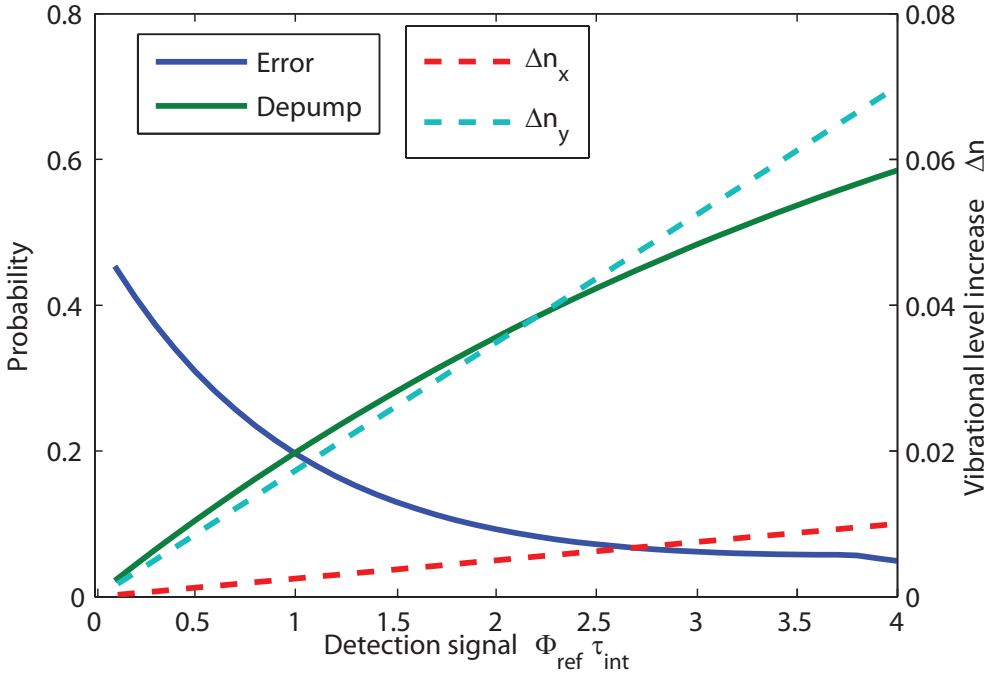

Figure 4.15: Figure of merit of the detection. We depict here all the effects of the measurement, as a function of the integration time, for a cavity light power $\Phi_{ref} = 100$ kCts/s and short integration time. Detection error probability (blue) is computed as explained in Sect. 4.4.3. Depumping probability (green) is computed from the fit of the Zeeman diffusion experiment. Average axial (red) and transverse (light blue) vibrational levels changes Δn are represented in dashed lines.

4.6 Conclusion

Let us summarise here the results obtained in this work concerning single atom detection. With a long detection time (typically 20 signal photons), we achieved a high-fidelity (error probability $\sim 3 \times 10^{-3}$), repeatable measurement of a single atom hyperfine quantum number F. This measurement being non-destructive, it can be applied in a deterministic single atom preparation scheme, and used as a tool for single-atom based experiments. Such an experiment is described in Chap. 5, and other possibilities were mentioned in the introduction.

We have also measured the measurement backaction on the other variables of the system. During the detection of a $|F = 2\rangle$ atom, the Zeeman state was found to be strongly perturbed by detection light. The initial knowledge of the Zeeman state is completely lost after about 50 μs at $\Phi_{ref} = 100$ kCts/s, or 5 signal-photons. This poses a severe restriction on the maximum detection efficiency we can achieve without changing the Zeeman state. The variables describing the motional state of the atom in the trap were found to be weakly disturbed by the measurement. This is mainly due to the large trapping frequencies of the dipole trap, which put the system in the Lamb-Dicke regime.

Chapter 5

Quantum Zeno effect with a single atom

This chapter described a Quantum Zeno Effect experiment which we realize with single atoms prepared with our apparatus. The effect is measured on microwave Rabi oscillations between the hyperfine states of the single atom. The cavity is used as a measurement apparatus of the atomic state, either in a continuous or a pulsed regime. The chapter is divided in four sections. The first section gives an introduction to the Quantum Zeno Effect. The second section explains how the cavity works as a measurement device, and give the expected decay rate of the atomic coherences. The third section describe the experimental results. The fourth section is proposal to extend the effect to multiple atoms and generate entangled states.

5.1 Introduction and basic theory

The Greek philosopher Zeno was famous for his paradoxes, which mainly dealt with the infinite divisibility of time and space into shorter, or point-like, elements. One of them is called the Arrow's paradox, and was formulated the following way by Aristotle in his *Physics* [100]:

> "If everything when it occupies an equal space is at rest, and if that which is in locomotion is always occupying such a space at any moment, the flying arrow is therefore motionless."

In a seminal paper [101], Misra and Sudarshan introduced a "Quantum Zeno Paradox" by considering the decay of an unstable particle under continuous monitoring (or measurement, to use a quantum mechanics vocable), and found that the decay was slowed down and eventually stopped. Denoting

by $|e\rangle$ the initial unstable state of the particle, and by $|i\rangle$ the initial environment state (the environment would be here the quantised radiation field for example), the coupled system state evolves as:

$$|\Psi(t)\rangle = \exp(-i\hat{H}t/\hbar)|\Psi_0\rangle, \tag{5.1}$$

where $\hat{H}$ is the complete Hamiltonian and $|\Psi_0\rangle = |e\rangle|i\rangle$. Setting $\hat{H} = \langle H\rangle_0 + \Delta\hat{H}$. The probability that the particle did not decay at time $t \ll \hbar/\Delta H$ is given by the approximate expression

$$\mathcal{P}_0(t) = |\langle\Psi(t)|\Psi_0\rangle|^2 \simeq |1 - \langle\Delta\hat{H}^2\rangle_0 t^2/2\hbar^2|^2 \simeq \exp(-\langle\Delta\hat{H}^2\rangle_0 t^2/\hbar^2). \tag{5.2}$$

We decompose the system evolution during a duration T into N evolutions of durations $t = T/N$, and assume that the system state is measured after each of these short evolutions at time $t_i = i \cdot t$, for integer i. The probability that the system has not decayed after time T is just the probability that at every measurement i, the system is found not to have decayed is the time interval $[t_{i-1}; t_i]$. It is therefore the product of the individual conditional probabilities

$$\mathcal{P}_i = \mathcal{P}(\text{No decay in } [t_{i-1}; t_i] | \text{No decay before } t_i) = \mathcal{P}_0(t = T/N), \tag{5.3}$$

since the projection postulate implies that the system state is projected the initial state $|\Psi_0\rangle$ if no decay was observed. The global non-decay probability is therefore:

$$\mathcal{P}_{\text{Non-decay}}(T) = \mathcal{P}_0(T/N)^N = \exp(-\langle\Delta\hat{H}^2\rangle_0 T^2/N\hbar^2) \tag{5.4}$$

In the limit $N \to \infty$, T constant, this probability tends to unity. The decay is then suppressed. We can therefore conclude that continuous observation of a quantum system freezes its dynamics. The effect originates mainly from the t^2 behaviour of the decay probability at short times. A physical insight is provided by considering the simple case where the particle can only decay to a single ground state $|g\rangle$ with a well-defined energy. Before the population is effectively transferred to the ground state, a coherence has to build up between states $|g\rangle$ and $|e\rangle$. This can be seen with the help of Bloch equations which describe Rabi oscillations between states $|e\rangle$ and $|g\rangle$:

$$\frac{d\rho_{gg}}{dt} = \Omega_R \text{Im}\rho_{eg} = -\frac{d\rho_{ee}}{dt}, \tag{5.5}$$

$$\frac{d\rho_{eg}}{dt} = i\frac{\Omega_R}{2}(\rho_{ee} - \rho_{gg}). \tag{5.6}$$

When the populations of the two states are measured, for example by the radiated field, the average populations are preserved but coherences are destroyed, thereby restarting the oscillation from scratch. Contrary to the classical Zeno paradox, the quantum Zeno paradox can certainly be accounted by the dynamical effect of the measurements. It was therefore renamed to "Quantum Zeno effect" (QZE) by the community.

The first observation of the QZE was done at NIST [102]. In this experiment, a Rabi oscillation between two stable states of about 5000 trapped Be^+ ions was induced by a resonant radiofrequency wave. By applying regularly spaced pulses of light, resonant with one of the two states, one can design a measurement process although scattered light is not actually monitored by the experimentator. The authors showed that the transfer efficiency of the radiofrequency dropped as the measurement rate increased, in agrement with predictions of the QZE.

The interpretation of the experiment was however subject to some debate [103, 104]. In particular, the very notion of measurement was questioned as the probe light pulses scattering was not recorded and therefore the measurement process did not involve a state change for a macroscopic "meter". It is worth noting here that the QZE does not need in theory a macroscopic measurement, but simply a correlation between the system and the environment states large enough to distinguish the system state by the knowledge of the environment state (even if the latter is not measured, or "amplified"). In mathematical terms, the global state must evolve during the measurement process as

$$(\alpha|e\rangle + \beta|g\rangle)|i\rangle \rightarrow \alpha|e\rangle|f_e\rangle + \beta|g\rangle|f_g\rangle, \tag{5.7}$$

where $|f_e\rangle$ and $|f_g\rangle$ are the two possible final states of the environment. The density matrix describing the state of the atom after the measurement is given by:

$$\rho_{at} = \mathrm{Tr}_{env}\rho = \begin{pmatrix} |\alpha|^2 & \alpha\beta^*\langle f_g|f_e\rangle \\ \alpha^*\beta\langle f_e|f_g\rangle & |\beta|^2 \end{pmatrix} \tag{5.8}$$

Coherences are therefore suppressed as the scalar product $S \equiv \langle f_g|f_e\rangle$ gets to 0, and the final density matrix approaches the ideal measurement result $\rho_{at} = |e\rangle\langle e|\rho_{at}(0)|e\rangle\langle e| + |g\rangle\langle g|\rho_{at}(0)|g\rangle\langle g|$. For non-vanishing S, the measurement only brings partial information about the system state, giving rise to a partial QZE as explained in [105].

In a very similar experiment, a quantum Zeno effect for a single Be^+ ion was demonstrated in [106]. Quantum Zeno effect has been since demonstrated in a variety of systems, such as optically pumped atoms and ions

[107, 108], photons in a microwave cavity [109], Bose-Einstein condensates [110], or on the motional states of optically trapped atoms [111]. This latter experiment stands out as the only one where the initial state is coupled with a continuum of states, and not with a single discrete state. Therefore, the decay is only quadratic in time in a very brief period following the preparation of the state, after which it becomes linear due to the dephasing between the possible final states. Besides these proof-of-principles experiments, applications, especially in quantum computing, are actively searched and some proposals already exist [112, 113, 114, 115, 116]. The main idea behind these schemes is to take advantage of the Zeno effect to forbid the occupation of states subject to decoherence. By monitoring continuously the populations of these decohering states, the dynamics is restricted to decoherence-free-subspaces. A general theory for the dynamics in this subspaces is developed in [117, 118].

5.2 Quantum Zeno effect induced by the cavity

5.2.1 Pulsed mode

As seen in the previous chapter, the knowledge of the cavity transmission on resonance allows to infer in which state $|0\rangle = |F = 1\rangle$ or $|1\rangle = |F = 2\rangle$ the single atom is. We have now to quantify the measurement process in terms of suppression of the coherences between $|0\rangle$ and $|1\rangle$. Using the general framework introduced above, we consider the atom-cavity system in the input-output formalism. The environment state $|f\rangle$ is the product of the final internal state $|m_F\rangle$, the motional state $\prod_{i=x,y,z} |n^i_{vib}\rangle$ and the light field state $|\Phi\rangle$.

We consider the following time-dependent modes for the light field, depicted on Fig. 5.1:

- An input mode $|\text{in}\rangle$, defined as a propagating square pulse in the input fibre, mode-matched with the cavity mode, with a duration $t_p \gg 1/\kappa$.

- An output mode $|\text{out}\rangle$, defined as the mode of the light leaking from the cavity by the output mirror[1].

[1] We shall emphasise here that this mode also include the losses at the cavity output mirror. This light cannot be detected, but still contributes to the collapse of the atomic coherences.

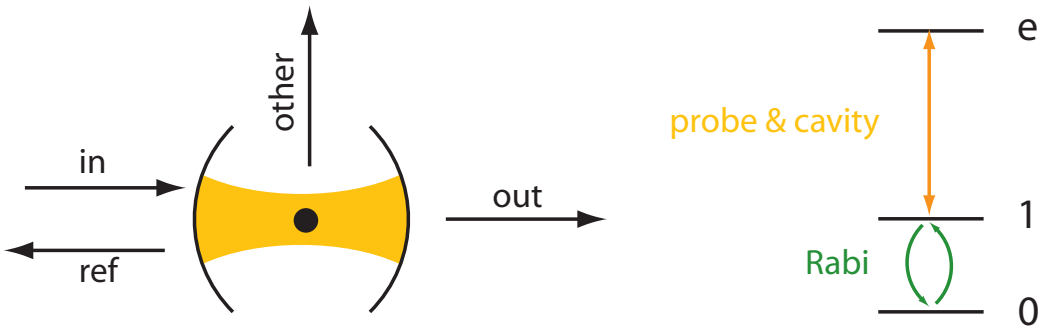

Figure 5.1: Description of atomic and light field modes.

- A reflected mode $|\text{ref}\rangle$, defined similarly as the output mode but with the input mirror[2].
- To ensure photon number conservation, we have to add another mode $|\text{other}\rangle$ which includes contributions of directly reflected light, orthogonal to the mode $|\text{ref}\rangle$, and light possibly scattered by the atom.

In a simple picture, the evolution of a coherent pulse of light initially in the incoming mode in given by

$$|\alpha_{in}\rangle \rightarrow |\alpha_{out}\rangle|\alpha_{ref}\rangle|\text{other}\rangle \tag{5.9}$$

When the atom is in the $|1\rangle$ state, the cavity does not transmit any light and $\alpha^1_{out} \simeq 0$. When the atom is in the $|0\rangle$ state, the cavity is resonant and the photon number in the cavity builds up to n_{ref} during the pulse. The number of leaked photons in the output fibre is then $|\alpha^0_{out}|^2 = n_{ref}\kappa t_p = \eta^2 t_p/\kappa$, with the usual notations of Sect. 1.1.3. The value of the reflected field depends on the cavity transmission-to-losses ratio, but we can see that the reflected fields in the case of states $|0\rangle$ and $|1\rangle$ *differ* by the contribution of light transmitted through the input mirror when the atom is in $|0\rangle$. Therefore we can conclude that $|\alpha^0_{ref} - \alpha^1_{ref}| = |\alpha^0_{out}| = \sqrt{\eta^2 t_p/\kappa}$. In the $|\text{other}\rangle$ modes, the contribution of directly reflected light is the same for the two possible atomic states, and the contribution of scattered light is negligible as we shall see later.

The contribution of the light field $|\Phi\rangle$ to the scalar product $S = \langle f_0|f_1\rangle$ involved in the decay of the atomic coherences is then

$$|\langle\Phi_0|\Phi_1\rangle| = |\langle\alpha^0_{ref}|\alpha^1_{ref}\rangle\langle\alpha^0_{out}|\alpha^1_{out}\rangle| = |\langle 0|\alpha^0_{out}\rangle|^2 = \exp(-\eta^2 t_p/\kappa) \tag{5.10}$$

[2]Because of losses of the input mirror, this mode does not coincide with the geometrical reflection of the input mode.

The coherence decay rate due to the light field η^2/κ has to be compared with the spontaneous emission rate which is the typical rate of processes affecting the Zeeman state and the vibrational states, giving additional contributions to the atomic coherence decay rate. Since we have $\Gamma_{sp} = 2\gamma\eta^2/g^2 = 1/C \times \eta^2/\kappa \ll \eta^2/\kappa$, the effect of these processes on the atomic coherence is negligible compared to the effect of the light field.

5.2.2 Continuous measurement with the cavity

In the original paper, the authors considered the situation of instantaneous measurements. In our experimental setup, this would correspond to infinitely brief and intense pulses of detection light. Due to technical limitations on the probe light power[3], we cannot realize this situation experimentally. Instead, we operate the cavity in a continuous measurement setting, sending a constant light power in the input fibre. For the atom-cavity system, the dynamics is very fast, being determined by the coupling rate $g = 2\pi \times 170$ MHz and the relaxation rate $\kappa = 2\pi \times 50$ MHz. Therefore, the value of the intracavity field quickly adjusts to the equilibrium value (which depends on the state of the atom), on a timescale $1/\kappa$. The decoherence of the system is due to the leakage of the cavity photons, with a typical rate η^2/κ. Since $\eta \ll \kappa$, it is therefore much slower than the relaxation rate κ. More precisely, the decoherence is described in the master equation by the Liouville term

$$\frac{d\rho}{dt} = \mathcal{L}(\rho) = 2\kappa \left(a\rho a^\dagger - \frac{1}{2}\{a^\dagger a, \rho\} \right) \tag{5.11}$$

Replacing the cavity field operator a by its state-dependent value $a = \alpha|0\rangle\langle 0|$, where $\alpha = \eta/\kappa$, and tracing over cavity variables yields the incoherent dynamics induced on the atomic state[4]:

$$\mathcal{L}(\rho^{at}) = 2\frac{\eta^2}{\kappa} \left(|0\rangle\langle 0|\rho^{at}|0\rangle\langle 0| - \frac{1}{2}\{|0\rangle\langle 0|, \rho^{at}\} \right) \tag{5.12}$$

This dynamics is equivalent to a continuous measurement of the system state, with a rate $\Gamma_m = \eta^2/\kappa$. Expanding the master equation in the $(|0\rangle, |1\rangle)$ basis, we find the equations for the diagonal and off-diagonal terms

$$\frac{d\rho^{at}_{00}}{dt} = 0, \tag{5.13}$$

$$\frac{d\rho^{at}_{10}}{dt} = -\frac{\eta^2}{\kappa}\rho_{10}. \tag{5.14}$$

[3] The limitation is due to the maximum photon flux the APD can stand.

[4] A similar treatment is applied in [119]; however, it concerns the bad cavity limit $\kappa \gg g$

This last equation predicts an exponential decay of the atomic coherences, with a rate $\Gamma_m = \eta^2/\kappa$, in agreement with the input-output model of the previous section. We shall nevertheless confirm the rather crude approximation $a = \alpha\mathbb{P}_0$. For that purpose, we perform a full numerical simulation of the master equation, taking into account the two possible ground states $|0\rangle$ and $|1\rangle$, an excited state $|e\rangle$ equally coupled to both ground states with a coupling constant g, and a cavity field with can take the two possible states $|n = 0\rangle$ and $|n = 1\rangle$. The $6^2 \times 6^2$ operator $\mathcal{L}$ is numerically diagonalised. The time evolution of any initial density matrix ρ_0 can be computed as $\rho(t) = \exp(\mathcal{L}t)\rho_0$. We choose the initial condition $\rho_0 = |\Psi_0\rangle\langle\Psi_0|$, where $|\Psi_0\rangle = \sqrt{\frac{1}{2}}(|0\rangle+|1\rangle)|n = 0\rangle$. From the computed solution $\rho(t)$ we can observe the two important phenomena, critical for the analysis done above. First, we can observe the correlation that progressively builds up between the atomic state and the photon state (See Fig. 5.2 Left). It is characterised by the density matrix elements $\langle 0; n = 1|\rho|0; n = 1\rangle$ and $\langle 1; n = 1|\rho|1; n = 1\rangle$ which reach their steady state value on a short timescale $1/\kappa$. Then, on a longer timescale, we can observe the progressive decay of the atomic coherence $|\rho_{01}^{at}|$. The agreement with the exponential decay at a rate η^2/κ is excellent (See Fig. 5.2 Right).

5.3 Frozen Rabi oscillations with a single atom

The two possible atomic states $|0\rangle = |F = 1\rangle$ and $|1\rangle = |F = 2\rangle$ are stable states. Therefore, to observe a Zeno effect with this system, we have to make them "unstable" by adding a resonant microwave field which induces transitions between the two states. The experimental setting is completely similar to the original experiment of Itano et al. Besides the fact that it is the first Zeno experiment to be performed with single neutral atoms, the originality of this experiment lies in the measurement process: here, the measurement is not caused by absorption and re-emission of probe light, but rather by the change of the cavity transmission induced by the presence of the atom in a particular state. Furthermore, the decoherence rate η^2/κ does not depend on the exact value of the atom-cavity coupling, provided the system is in the strong coupling regime $C \gg 1$. It is just equal to the photon flux leaking from the cavity, so that a single photon leaving the cavity provides the bit of information needed to deduce the atomic state.

The effect of continuous measurement on Rabi oscillations can be calculated by adding the contribution of the measurement (Eqns. 5.13) to basic

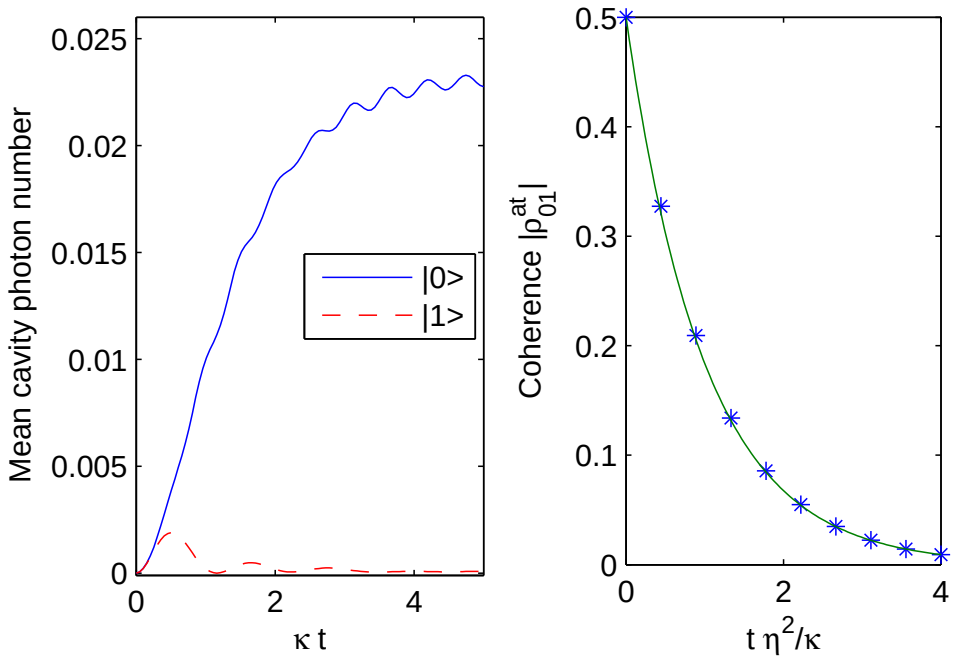

Figure 5.2: Numerical simulation of the cavity master equation, with the atom initially in the superposition state $|\Psi_0\rangle = \sqrt{\frac{1}{2}}(|0\rangle + |1\rangle)$. The cavity probe power is set at $\Phi_{ref} = 1$ MCts/s, with detunings $\Delta_a = \Delta_c = 0$.
Left: From the complete density matrix ρ, we can compute the cavity photon number distribution, conditional to the atomic state. The mean value is plotted here for the two possible atomic states $|0\rangle$ (full blue line) and $|1\rangle$ (red dashed line), shortly after probe light is switched on. We observe the typical timescale to reach the equilibrium.
Right: The reduced atom density matrix is obtained by tracing over the cavity states. The evolution of the off-diagonal terms (blue stars) is compared to an exponential decay $|\rho_{01}^{at}| = 0.5 \exp(-\eta^2 t/\kappa)$ (green line).

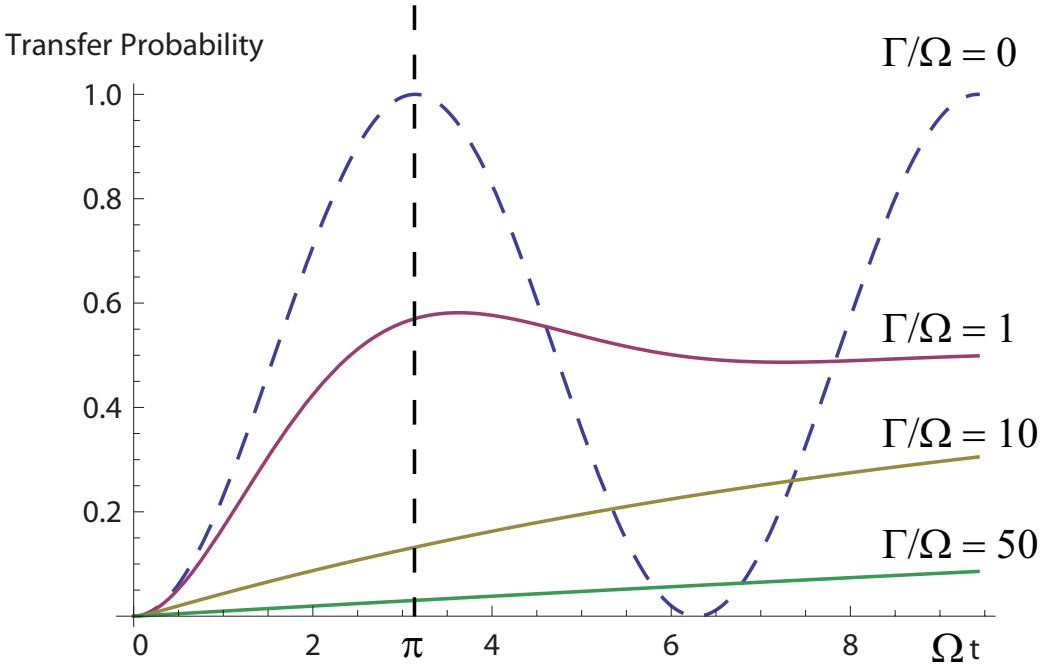

Figure 5.3: Effect of a continuous measurement on Rabi oscillations. The transfer efficiency is depicted as a function of time for various measurement rates $\Gamma_m/\Omega_R = 0$ (blue), 1 (magenta), 10 (yellow), 50 (green).

Bloch equations (Eqns. 5.5). The equation for the population and coherence can be combined in a single 2nd order differential equation for the population:

$$\frac{d^2\rho_{00}^{at}}{dt^2} + \Gamma_m \frac{d\rho_{00}^{at}}{dt} + \Omega_R^2 \rho_{00}^{at} = \frac{1}{2}\Omega_R^2 \tag{5.15}$$

For $\Gamma_m/\Omega_R < 2$, Rabi oscillations are still present but exponentially damped with a rate $\Gamma_m/2$. For $\Gamma_m/\Omega_R > 2$, the oscillations are suppressed. The equation can be solved analytically, and results for various measurement rates Γ_m are displayed on Fig. 5.3. For increasing values of Γ_m, the transfer efficiency of a π-pulse ($\Omega_R t = \pi$) drops from 1 to 0.

5.3.1 Single atom Rabi oscillations

We shall start by the observation of undamped Rabi oscillations with a single atom, when the measurement is switched off during the mw pulse.

Using the techniques described in Chap. 4, we can prepare single atoms in the state $|1\rangle = |F = 2; m_F = 0\rangle$. By switching on the resonant microwave

field, we induce Rabi oscillations between states $|0\rangle = |F = 1; m_F = 0\rangle$ and $|1\rangle$. After a duration t, the system is in the coherent superposition of states:

$$|\Psi(t)\rangle = \cos\frac{\Omega_R t}{2}|1\rangle + \sin\frac{\Omega_R t}{2}|0\rangle, \tag{5.16}$$

where Ω_R is the microwave Rabi frequency. If a state measurement is performed, the transfer probability is given by $\mathcal{P}_t(t) = \sin^2\frac{\Omega_R t}{2}$. To measure the state of the system, we simply shine resonant light with a reference power of $\Phi_{ref} \sim 1$ Mcts/s, and look at the detected counts for 20 μs. We do not need to perform a complete state measurement.

By repeating the experiment, and averaging the results of the measurement, we can measure the transfer probability as a function of the mw pulse duration t. Results displayed on Fig. 5.4 show Rabi oscillations with a contrast of about 80% and a Rabi period $T_R = 2\pi/\Omega_R = 10.7 \pm 0.2\mu$s. The observed reduced contrast is in fact partly due to the limited transfer efficiency of the mw π-pulse already required to prepare the single atom in the $|F = 2\rangle$ state. It is therefore consistent with a maximum transfer efficiency of about 90% for a π-pulse.

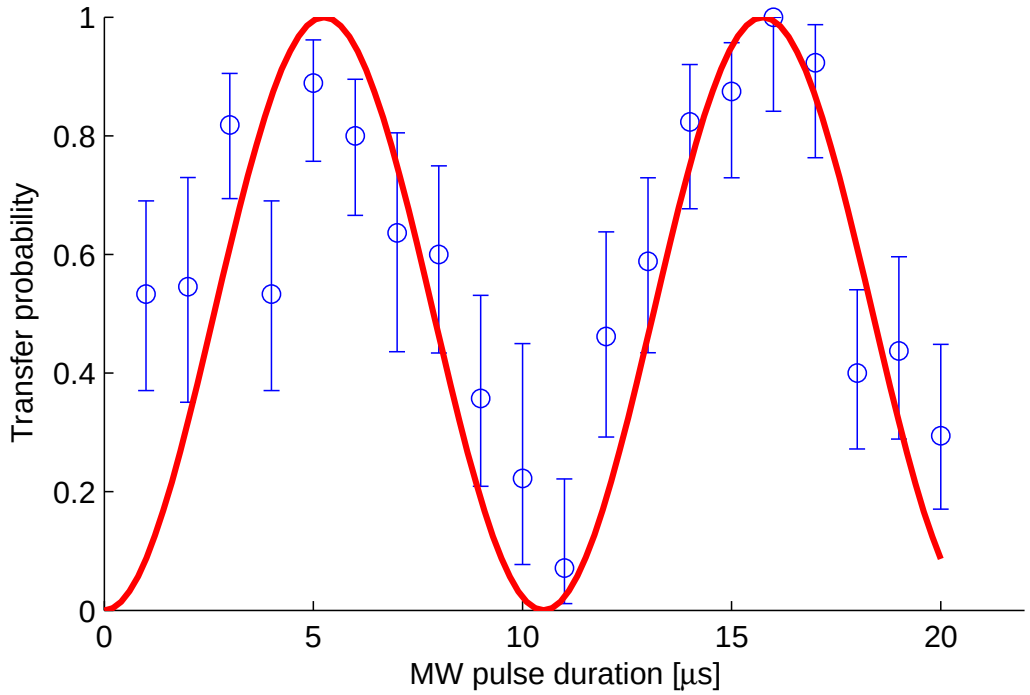

Figure 5.4: Single atom Rabi oscillations on the $|F = 2; m_F = 0\rangle \rightarrow |F = 1; m_F = 0\rangle$ transition. For each MW pulse duration, the transfer probability (blue circles) is inferred from the measurement of the atom final state with 15 successful single atom preparations. The error bars are statistical. The full line is the expected sinusoidal behaviour for $T_R = 10.7\mu$s.

5.3.2 Observation of a Quantum Zeno effect

The section is devoted to the observation of this damping and freezing of the Rabi oscillations, in the regime of continuous measurement and pulsed measurements.

Continuous Quantum Zeno effect

The quantum Zeno effect is best observed with a microwave π-pulse. The transfer probability is then expected to drop from its maximum value $\sim 90\%$ to 0 as the measurement rate is increased. The QZE is expected to occur for $\Gamma_m = \eta^2/\kappa \sim \Omega_R$, which corresponds to a reference output rate $\Phi_{ref} = \sim 100$ kCts/s, easily achievable experimentally. Once the single atom preparation in the state $|F = 2; m_F = 0\rangle$ is done, the probe light power is adjusted with the help of a voltage-controlled RF attenuator which limits

the diffraction efficiency of the acousto-optical modulator AOM2 (See Sect. 2.2.2). The control voltage is provided by the microcontroller. A delay of 100μs is added to allow the microcontroller analog output and the RF power to stabilise, before the probe light ("Zeno light") is eventually switched on. After another short delay of 2μs, the microwave field is switched on for a duration of $\tau_{mw} = 5.5\mu$s, approximately corresponding to a π-pulse. Zeno light is then switched off, and the rf power restored to its original value suitable for state measurement. The final state measurement is performed as usual with a duration of 20μs at a reference power of $\Phi_{ref} = 1$ Mcts/s. We only measure the value of F.

This experiment can be performed equally well with single atoms starting out in state $|0\rangle$ or $|1\rangle$. Although the measurement process seems to be asymmetric, the cavity being resonant only with state $|1\rangle$, it is completely equivalent to measure the final state population or the initial state population. We therefore expect the same results for the two possible prepared states. Experimental results are displayed on Fig. 5.5 (Top). The agreement with theory is noteworthy, since there are no adjustable parameters in theory. The effect of depumping to other Zeeman states should be taken into account for large measurement rates when the initial state is $|1\rangle$. In particular, for $N_{mes} > 30$, the transfer to state $|0\rangle$ is not only prevented by Zeno effect, but also by trivial depumping to other $|F = 2; m_F\rangle$ states which are non-resonant with the microwave field, because of Zeno light. However, this effect only occurs when the Zeno effect is already strong enough to suppress almost completely Rabi oscillations, and it is not the main effect. The experiments performed starting in state $|0\rangle$ confirms it.

Pulsed partial Quantum Zeno effect

The experiment described above can be slightly modified to investigate the pulsed regime of Quantum Zeno effect, closer to the original proposal. Zeno light is sent in short pulses of typical duration t_p, which can be considered as instantaneous measurements when $t_p \ll T_R$. The efficiency of this elementary measurement is characterised by the effect on the density matrix described by Eqn. 5.8. To obtain a significant coherence decay, the brevity of the light pulse has to be compensated by a large peak power to ensure $\eta^2 t_p/\kappa \gtrsim 1$. Experimentally, we have to reach a compromise since the maximum power is limited by the photon counter which we cannot shut down in such a short notice. After the atom preparation, we adjust the probe light power to the maximum allowed value $\Phi_{ref} = 5.5$ MCts/s with the help of the RF attenuator. Light pulses are generated with a pulse generator which controls

the RF switch. Due to the AOM finite response time, the optical response to a square, 130 ns long electric pulse is a quasi-Gaussian optical pulse, with an amplitude of about 70% of base power and a duration of 30 ns FWHM. We precisely calibrate the pulse photon number with the photon counter and find the equivalent photon number $n_p = \int \eta^2/\kappa dt = 1.1$. The effect of such a measurement pulse is characterised by the scalar product $S \equiv \langle \Phi_0 | \Phi_1 \rangle = \exp(-n_p) = 0.3$. The coherences are then reduced by a factor 3 after each measurement pulse.

The experiment is performed with 0 to 20 measurement pulses, with an initial atom preparation in state $|1\rangle$. Experimental results are shown on Fig. 5.5 (Bottom). The theory for a partial Zeno effect in the pulsed regime is given in [105]. The main parameter of the theory is the scalar product $S = \langle \Phi_0 | \Phi_1 \rangle$ which characterises the effect a single pulsed partial measurement on the coherence of the system. Experimental results are in agreement with the theory with a different value of the fitting parameter $S_{fit} = 0.55$, corresponding to a pulse photon number $n_{p,fit} = 0.6$. Discrepancy with the expected value $S = 0.33$ can be at least partly explained by spectral broadening of the measurement pulse, since $1/t_p \sim 30$ MHz, a value comparable to the cavity linewidth and larger than atomic linewidth.

In this section, we have reported the first QZE experiments with single neutral atoms. We have verified that in the cavity QED strong coupling regime, the effective continuous measurement rate of the system was given by the reference photon output rate η^2/κ *excluding losses*. If we compare this rate to spontaneous emission rate measured by the Zeeman diffusion experiment (see Sect. 4.5.2), we find that the measurement rate is approximately 20 times larger than the spontaneous emission rate at a given probe power.

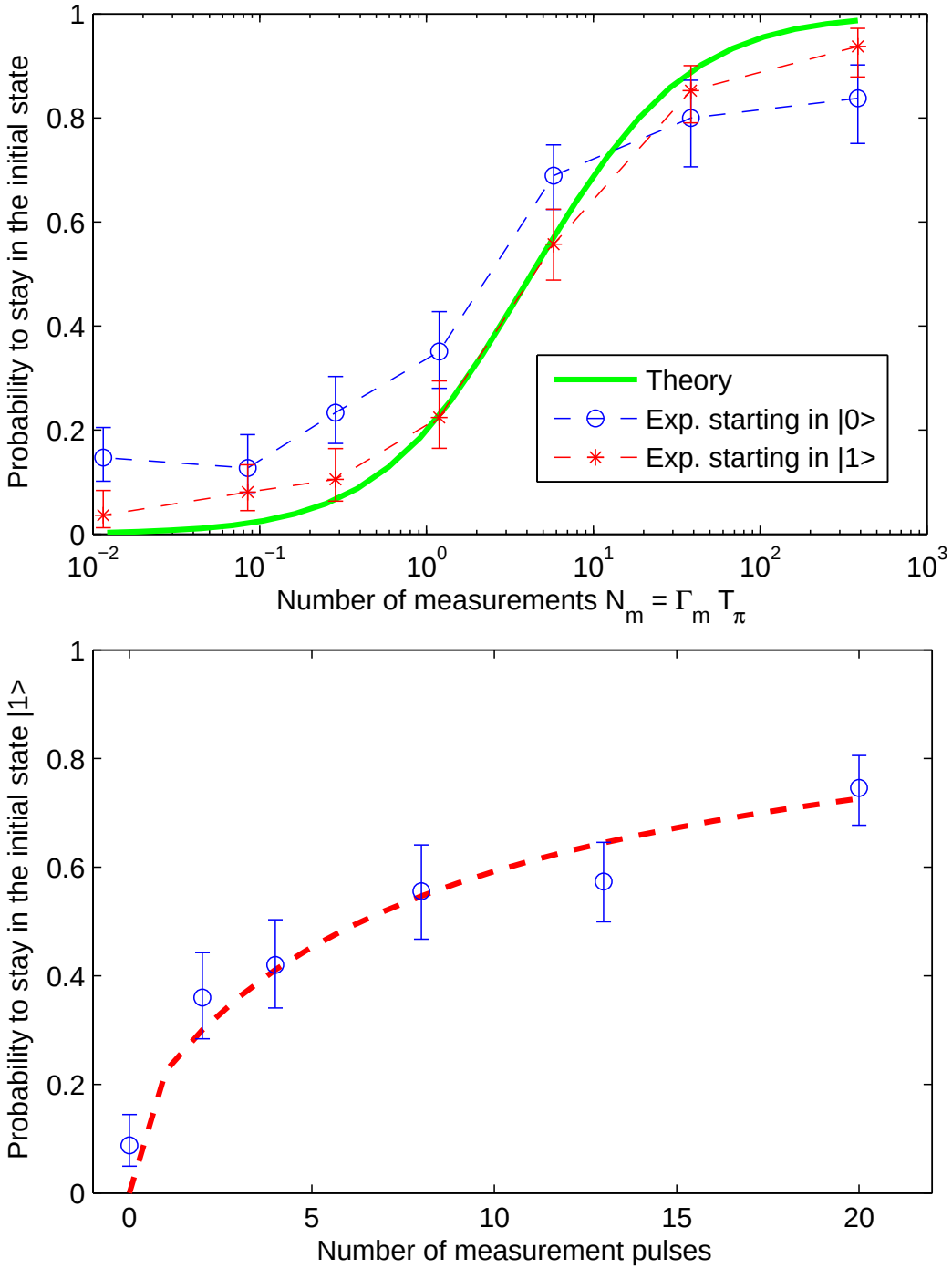

Figure 5.5: Quantum Zeno effect with a single atom. The probability that the atoms stays in its initial state after a mw π-pulse is depicted as a function of the Zeno light power, expressed in terms of number of equivalent measurements N_{mes}.
Top: **Continuous measurement regime**. Here $N_{mes} = \Gamma_m T_\pi$. Experimental data for initial atom preparation in state $|0\rangle$ (resp. $|1\rangle$) is plotted with blue circles (resp. red stars), along with statistical error bars. Theory derived from Eqn. 5.15 is the green line.
Bottom: **Pulsed, partial measurement regime**. Here N_{mes} is the number of measurement pulses. The theory curve (red dashed line) is computed with the fitting parameter $S_{fit} = 0.55$ (see text).

5.4 A proposal for QZE entanglement generation

In the experiments described above, and in other work done previously, the QZE manifests itself as a freezing of the system dynamics. When the measurement outcome allows to identify precisely the quantum state, the system state is projected back to its initial value, and the state does not evolve. The physics of the QZE is then somehow limited.

However, this situation is not general: if several quantum states yield the same measurement outcome, the state is projected to the eigenspace spanned by these quantum states. Therefore, the dynamics in this "Zeno subspace" is not impeded. Theoretical studies of this topic lead to the notion of "Quantum Zeno dynamics" (QZD), and recent proposals of applications for QZE take advantage of that.

In this section, we will give a brief introduction to QZD theory, and discuss an application to the preparation of entangled states, within the reach of our experimental apparatus.

5.4.1 Quantum Zeno dynamics

The theory of QZD is a sizeable mathematical subject and we certainly do not intend to bring here large mathematics developments, but rather take the point of view of the physicist. In fact, the original paper by Misra and Sudarshan already rose the critical question: is the dynamics unitary in the Zeno subspaces? For infinite-dimension Hilbert space, the answer is in general negative, although it is true for some particular cases (see for example [117] for the motion of a free particle under continuous position measurement). In a finite-dimension Hilbert space, the answer is positive, and the dynamics is governed by an effective Hamiltonian in the different Zeno subspaces. A clean mathematical proof is given in [120]. We shall rederive it here, using a physics approach. Let us consider the evolution of a quantum system described by a density matrix ρ, with a general Hamiltonian H, and subject to continuous measurement of a given variable x. We suppose here that the variable x can only take two possible values 1 and 2. The projectors on the eigenspaces E_1 and E_2 of x are denoted by $\mathbb{P}_1$ and $\mathbb{P}_2$. A single measurement projects the density matrix ρ following the mapping $\rho \rightarrow \mathbb{P}_1\rho\mathbb{P}_1 + \mathbb{P}_2\rho\mathbb{P}_2$. If we assume that the system is continuously measured, then we have at any time $\rho = \mathbb{P}_1\rho\mathbb{P}_1 + \mathbb{P}_2\rho\mathbb{P}_2$. As a consequence we can derive

the following properties for the density matrix:

$$\mathbb{P}_1\rho\mathbb{P}_2 = 0 \quad (5.17)$$
$$\mathbb{P}_1\rho\mathbb{P}_1 = \mathbb{P}_1\rho = \rho\mathbb{P}_1 \quad (5.18)$$

The first equation means that the coherence between states lying in different Zeno subspaces all vanish, due to continuous measurement. The evolution of the density matrix during an elementary time step dt is the combination of an Hamiltonian evolution $\rho \to U(dt)\rho U^\dagger(dt)$, where $U(dt) = \exp(-idtH) = 1 - idtH + \mathcal{O}(dt^2)$, and a measurement process $\rho \to \mathbb{P}_1\rho\mathbb{P}_1 + \mathbb{P}_2\rho\mathbb{P}_2$. Therefore we can write at the first order in dt:

$$\begin{aligned}
\rho(t+dt) &= \mathbb{P}_1(1-iHdt)\rho(1+iHdt)\mathbb{P}_1 + \mathbb{P}_2(1-iHdt)\rho(1+iHdt)\mathbb{P}_2 \\
&= \mathbb{P}_1\rho\mathbb{P}_1 + \mathbb{P}_2\rho\mathbb{P}_2 + \mathbb{P}_1(-iHdt)\rho\mathbb{P}_1 + \mathbb{P}_1\rho(iHdt)\mathbb{P}_1 \\
&\quad + \mathbb{P}_2(-iHdt)\rho\mathbb{P}_2 + \mathbb{P}_2\rho(iHdt)\mathbb{P}_2 \\
&= \rho + \mathbb{P}_1(-iHdt)\mathbb{P}_1\rho + \rho\mathbb{P}_1(iHdt)\mathbb{P}_1 \\
&\quad + \mathbb{P}_2(-iHdt)\mathbb{P}_2\rho + \rho\mathbb{P}_2(iHdt)\mathbb{P}_2 \\
&= \rho + [\rho, H_Z]idt, \quad (5.19)
\end{aligned}$$

where the Zeno Hamiltonian is simply defined by $H_Z = \mathbb{P}_1 H\mathbb{P}_1 + \mathbb{P}_2 H\mathbb{P}_2$. For a system initially prepared in a pure state $|\Psi_1\rangle \in E_1$, eigenstate for the measured variable x, the evolution is hamiltonian and $|\Psi(t)\rangle = \exp(-iH_Z t)|\Psi_1\rangle$.

5.4.2 Partial measurement with the cavity

As we have seen with previous experiments, the cavity transmission drops to a small value when there is at least a single atom in the cavity in the state $|1\rangle$[5]. However, the cavity does not distinguish accurately whether there is exactly one atom in state $|1\rangle$, or several. Suppose we prepare two atoms, strongly coupled to the cavity, both of which can be either in state $|0\rangle$ or $|1\rangle$, and perform a measurement of the cavity transmission. In an idealised picture, the measurement has only two possible outcomes "the cavity transmits" or "the cavity does not transmit". The Zeno subspaces for this measurement are:

$$E_1 = \mathrm{Vect}(|0\rangle|0\rangle) \quad (5.20)$$
$$E_2 = \mathrm{Vect}(|1\rangle|0\rangle; |0\rangle|1\rangle; |1\rangle|1\rangle) \quad (5.21)$$
$$= \mathrm{Vect}(|\Psi^-\rangle; |\Psi^+\rangle; |1\rangle|1\rangle), \quad (5.22)$$

[5] We consider here the usual setting, with the cavity and probe light resonant with the $|F=2\rangle \to |F'=3\rangle$ transition.

where we defined the Bell states $|\Psi^{\pm}\rangle = \sqrt{\frac{1}{2}}(|10\rangle \pm |01\rangle)$.

We consider the effect of a Hamiltonian $\hat{H} = g(\hat{\sigma}_{10}^{(1)} + \hat{\sigma}_{01}^{(1)}) + g(\hat{\sigma}_{10}^{(2)} + \hat{\sigma}_{01}^{(2)})$ acting separately on the two atoms via the single particle operators $\hat{\sigma}_{ij}^{(k)}$. If the measurement is switched off, the effect of this interaction is an independent rotation of the two spins. When the measurement is switched on, and the system starts out in the state $|11\rangle$, the QZE prevents the system from reaching the state $|00\rangle$. In particular, when one particle is in the state $|0\rangle$, the second one has to be in state $|1\rangle$. Therefore, the measurement induces a correlation between the atoms. Using the QZD theory, we can study the dynamics in the E_2 subspace. The effective Hamiltonian is conveniently rewritten in the $(|\Psi^-\rangle; |\Psi^+\rangle; |1\rangle|1\rangle)$ basis:

$$H_Z^1 = g\sqrt{2} \begin{pmatrix} 0 & 0 & 0 \\ 0 & 0 & 1 \\ 0 & 1 & 0 \end{pmatrix} \tag{5.23}$$

The evolution of a pair of atoms initially prepared in the state $|11\rangle$ is then a Rabi oscillation between the states $|11\rangle$ and $|\Psi^+\rangle$ with a collective Rabi frequency $\Omega_R' = \sqrt{2}\Omega_R = g/\sqrt{2}$:

$$|11\rangle \rightarrow \cos(g\sqrt{2}t)|11\rangle - i\sin(g\sqrt{2}t)|\Psi^+\rangle \tag{5.24}$$

If the evolution is stopped after a time $t = \pi/(2\sqrt{2}g)$, corresponding to a $\pi/\sqrt{2}$-pulse for a single atom, the system ends up in the entangled state $|\Psi^+\rangle$. In [121, 122], the authors demonstrated a similar preparation scheme to prepare a $|\Psi^+\rangle$ state with a fidelity of 75%. In this experiment, transitions to state $|00\rangle$ are prevented by large dipole-dipole interaction between Rydberg states. Here, the interaction is instead provided by the cavity measurement.

5.4.3 Experimental details and numerical simulations

We shall discuss here to which extent this preparation can be applied to our current cavity experiment. First, we need a pair of single atoms in the state $|1\rangle$ to start with. The atoms do not need to be positioned in the same dipole trap site, since the coupling to the cavity mode changes only slightly from one site to the next. With the help of an external magnetic field gradient oriented along the cavity axis, we can single out specific sites for microwave transitions that are sensitive to magnetic field, such as the transition $|F = 1; m_F = 1\rangle \rightarrow |F = 2; m_F = 0\rangle$ involved in single atom preparation. Running current in a chip wire located 150 μm above, one can reasonably achieve a magnetic field gradient of about 0.1G/μm in the cavity

mode. With dipole trap sites separated by about 0.4 μm ($\lambda/2$), the order of magnitude of the relative detuning between the two sites would be around 50 kHz, which is large enough to prevent almost completely Rabi oscillations in one site when they are resonant for the next site[6].

We start with a reservoir of $|F = 1; m_F = 1\rangle$ atoms delocalised over at least two neighbouring dipole trap sites called 1 and 2. Using the pulse scheme, we prepare a single atom in state $|F = 2; m_F = 0\rangle$ in site 1, which we hide in state $|F = 1; m_F = -1\rangle$ by using again a field-dependent microwave transition. This single atom has a small effect on the cavity transmission, just as if it were in the reservoir state. We can then prepare a single $|F = 2; m_F = 0\rangle$ atom in site 2. The preparation is then completed by performing a last microwave π-pulse on transition $|F = 1; m_F = -1\rangle \rightarrow |F = 2; m_F = 0\rangle$ on site 1. Although it requires careful control over all these microwave pulses, this preparation scheme should be within experimental reach.

We now turn to cavity detection issues. In the idealised picture presented above, the cavity measurement has only two possible outcomes, whereas in reality has at least three possible transmission values $T_{0,1,2}$ for the three possible number of atoms in state $|1\rangle$. However, the transmission is very low for both $N_1 = 1$ and $N_1 = 2$, which means that we have to send many photons to detect whether we have 1 or 2 atoms in state $|1\rangle$, whereas we need only a few photons to know whether $N_1 = 0$ or not. We can therefore consider that the system undergoes two different types of continuous measurements: the first is very fast (rate Γ_m) and crude in the sense it can only distinguish state $|00\rangle$ from other states; the second is slower (rate Γ'_m) and finer as it distinguishes $|00\rangle$, $|11\rangle$ from other states. For $\Gamma'_m > \Omega_R$, the entanglement scheme described in previous section collapses, as the dynamics of the initial state $|11\rangle$ is also frozen. For $\Omega_R > \Gamma_m$, the effect of the measurement is to small to prevent the normal dynamics, and the system state is always separable for any interaction time. The regime $\Gamma'_m < \Omega_R < \Gamma_m$ is the interesting one: the dynamics in the E_2 subspace in still possible, while the crude measurement is efficient enough to forbid transfers to state $|00\rangle$.

This qualitative analysis needs to be confirmed by a numerical simulation. The single atoms are described by a three level structure ($|0\rangle, |1\rangle, |e\rangle$) and are independently coupled to the cavity field $\hat{a}$ by $\hat{H}^{(i)}_{int} = g^{(i)}\hat{\sigma}^{(i)}_{1e}\hat{a}^\dagger + g^{*(i)}\hat{\sigma}^{(i)}_{e1}\hat{a}$, and to the microwave field by $\hat{H}^{(i)}_{mw} = \Omega_R(t)/2(\hat{\sigma}^{(i)}_{10} + \hat{\sigma}^{(i)}_{01})$. We assume here

[6] This would also require to decrease the Rabi frequency down to 5 kHz or so, which is of course possible by decreasing the mw power. Measured coherence times for Rabi oscillations (see Sect. 2.3.2) are compatible with high efficiency Rabi pulses with frequencies in the kHz range

that the microwave field is resonant to both atoms (since the clock transition is field-insensitive) and that the amplitude and phase are the same (since $d_{12} \ll \lambda_{mw}$). The effect of spontaneous emission can be modelised in different ways:

- **Independent** By two independent collapse operators $C^{(i)} = \sqrt{2\gamma}\hat{\sigma}_{1e}^{(i)}$. Doing this, we assume that the environment (or electromagnetic field) distinguishes spontaneously emitted light from the two atoms. This corresponds to the limit $d_{12} \gg \lambda$.
- **Super-radiant** With a single collapse operator $C = \sqrt{2\gamma}(\hat{\sigma}_{1e}^{(1)} + \hat{\sigma}_{1e}^{(2)})$. This corresponds to the opposite limit $d_{12} \ll \lambda$ [123].
- **General case** With collective collapse operators $C(\mathbf{k}) = \sqrt{2\gamma A(\mathbf{k})}(\exp(i\mathbf{k}.\mathbf{r}_1)\hat{\sigma}_{1e}^{(1)} + \exp(i\mathbf{k}.\mathbf{r}_2)\hat{\sigma}_{1e}^{(2)})$, where $A(\mathbf{k})$ is the dipole far-field emission pattern [124]. This approach covers both the super-radiant and the independent limits, but is computationally more intensive, so we discarded it.

Spontaneous emission has to be taken care of seriously since it induces transitions to other m_F states. The cavity field pump and decay is treated as usual, although we use a pulsed pump to end in the $|n = 0\rangle$ cavity state. The evolution of $\rho(t)$ is obtained by solving numerically the master equation. The fidelity of the preparation is defined by the scalar product $F = \langle\Psi^+|\rho_{final}^{at}|\Psi^+\rangle$. The evolution of F is displayed on Fig. 5.6 Top. As expected, the maximum fidelity is obtained with a microwave pulse duration of $T_\pi/\sqrt{2}$. We optimise the measurement rate $\Gamma_m = \eta^2/\kappa$ by maximising the figure of merit $M = F - N_{spont}$, where $N_{spont} = \int \Gamma_{sp} dt$ is the mean cumulated number of spontaneous emissions. The optimum measurement rate for $g^{(1)} = g^{(2)} = 2\pi \times 140$ MHz and $\Omega_R = 2\pi \times 50$ kHz is approximately $\Gamma_m = 5\Omega_R$, and leads to the following results:

Model	F	N_{sp}	M
Super-radiant	.83	.19	.64
Independent	.79	.14	.65

We can deduce from these figures that the fidelity of the preparation is severely impacted by spontaneous emission. In the super-radiant model, the fidelity can be increased to 0.90 for $\Gamma_m = 10\Omega_R$, but at the cost of a larger spontaneous emission. It is worth noticing that the scheme is robust to variations of the amplitude and phase of the coupling constants $g^{(1)}$ and $g^{(2)}$, and therefore does not require perfect atom localisation, nor preparation

of pairs of atoms in the same site (which would require a more complicated protocol than the one presented above).

To measure the final state, we can perform independent measurements of the two atomic states, using hiding pulses similar to the ones necessary for the pair preparation. Combining these measurements with global microwave pulses is in principle sufficient to perform the complete tomography of the system [125, 122]. Given the figure of merit of the scheme, and unavoidable technical problems such as initial state preparation, measurement errors, pulse shape inaccuracy, it is not clear whether the final measured fidelity will exceed 1/2, the minimum value to characterise quantum entanglement. However, by simply measuring the states of the atom as a function of Rabi pulse duration, it should be possible to observe the collective Rabi oscillations for $\langle N_1 \rangle$, with a frequency $\Omega_R \times \sqrt{2}$ characteristic of Quantum Zeno dynamics (see Fig. 5.6 (Bottom)).

5.5 Conclusion

The Quantum Zeno effect is a dramatic manifestation of the fundamental feature of quantum mechanics theory: measuring a system perturbs it. Therefore, it is always very instructive to measure it with a new system, and it is an excellent application to the single atom preparation scheme described in the previous chapter. Moreover, the QZE experiments reported here show that in the setting of cavity QED, the measurement rate is enhanced by the strong coupling with the cavity mode, and that the environment measures the state of the atom without inducing a spontaneous emission 95% of the time. Hence, this experiment is an example of a quasi perturbation-free measurement realized with a cavity.

In a second part, we have presented an introduction to QZD theory which aims to bring promising applications of the QZE to quantum information science. We have also proposed a QZD-based protocol to generate entangled states of two atoms trapped in the cavity mode at two different sites. We discussed the feasibility of an experimental realization with our current setup.

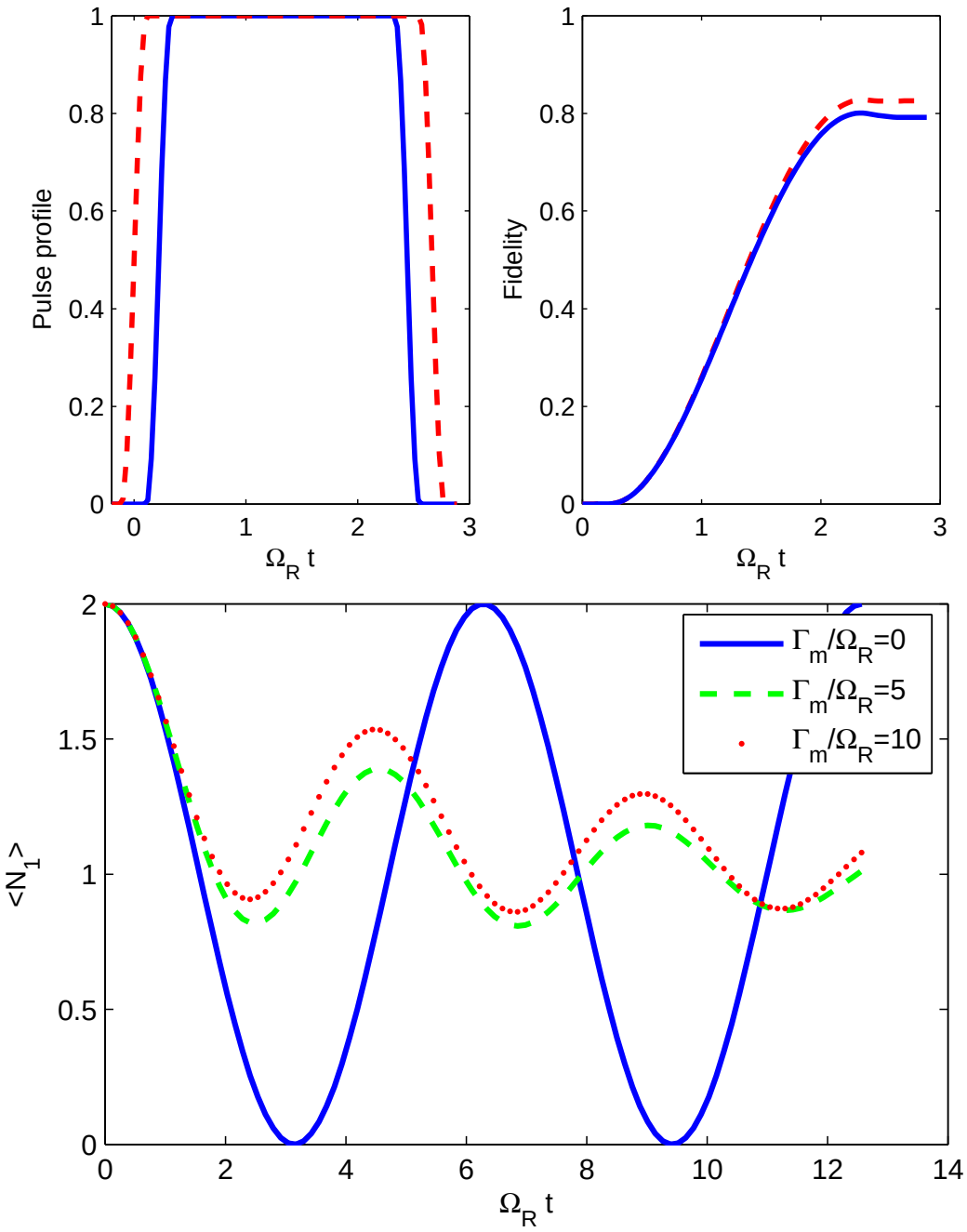

Figure 5.6: Numerical simulation of entanglement generation by QZD. Simulation parameters are $g^{(1)} = g^{(2)} = 2\pi\times140$ MHz, $\Delta_a = \Delta_c = 0$, $\Omega_R = 2\pi\times50$ kHz.
Top: Microwave and measurement are pulsed, with $T_{mw} = T_\pi/\sqrt{2}$. The measurement rate is set to the optimum value $\Gamma_m = 5\Omega_R$.
Left: Pulses profiles, normalised to their maximum value, for measurement light amplitude η (dashed red line) and Rabi frequency Ω_R (full blue line).
Right: Fidelity of the state preparation, for independent collapse model (full blue line) and super-radiant model (red dashed line).
Bottom: Effect of measurement light on Rabi oscillations, in the continuous regime and with independant spontaneous emission from the two atoms. Rabi oscillations are depicted for different values of the measurement rate Γ_m.

Appendix A

Derivation of the rate equations

First, we group the equations 1.55 in the global form

$$\frac{d\rho}{dt} = \mathcal{L}(\rho) = \tilde{\mathcal{L}}(\rho) + S(\rho), \tag{A.1}$$

emphasising the operator form of $\tilde{\mathcal{L}}$ and S. The density matrix ρ can be seen as a vector in a Hilbert space defined by the scalar product $(\rho_1, \rho_2) = \mathrm{Tr}(\rho_1^\dagger \rho_2)$. The Liouvillian and the source term can be seen as self-adjoint operators. We can therefore apply the usual perturbation theory.
We write $\rho = \sum_{m_F} \mathcal{P}^{m_F} \tilde{\rho}_{ss}^{m_F} |m_F\rangle\langle m_F| + \delta\rho = \sum_{m_F} \mathcal{P}^{m_F} e_{m_F} + \delta\rho$, where $\delta\rho$ is perpendicular to $E = \mathrm{Vect}\,(e_{m_F}, m_F = -2 \ldots 2)$. $\delta\rho$ and $d/dt\mathcal{P}_{m_F}$ are first order terms in the small parameter γ/κ. The rate equations can be computed as

$$\frac{d\mathcal{P}^{m_F}}{dt} = \left(e_{m_F}, \mathcal{L}\rho\right) = \left(e_{m_F}, S(\sum_{m_F} \mathcal{P}^{m_F} e_{m_F})\right) \tag{A.2}$$

which yields Eqn. 1.59. The time evolution of $\delta\rho$ is given by

$$\frac{d\delta\rho}{dt} = \tilde{\mathcal{L}}(\delta\rho) + \sum_{m_F} \mathcal{P}^{m_F} S(e_{m_F}) - \frac{d\mathcal{P}^{m_F}}{dt} e_{m_F} \tag{A.3}$$

$$= \tilde{\mathcal{L}}(\delta\rho) + K(t) \tag{A.4}$$

$\delta\rho$ is confined to the subspace $E^\perp$, where $\tilde{\mathcal{L}}$ is upper-bounded by $-\kappa$. The order of magnitude of $K(t)$ is $\Gamma = \gamma \max_{m_F} \mathrm{Tr}(P_e e_{m_F})$. Solving for $\delta\rho$ we find

$$\delta\rho(t) = \exp(\tilde{\mathcal{L}}t)\delta\rho(0) + \int_0^t du \exp\left(\tilde{\mathcal{L}}(t-u)\right) K(u), \tag{A.5}$$

which shows that the order of magnitude of $\delta\rho(t)$ is $\Gamma/\kappa \ll \gamma/\kappa$.

Bibliography

[1] E. M. Purcell. Spontaneous emission probabilities at radio frequencies. *Phys. Rev.*, 69,:681–, 1946.

[2] D. Meschede, H. Walther, and G. Mueller. One-atom maser. *Physical review letters*, 54(6):551–554, 1985.

[3] G. Rempe, H. Walther, and N. Klein. Observation of quantum collapse and revival in a one-atom maser. *Physical review letters*, 58(4):353–356, 1987.

[4] M. Brune, J. Raimond, P. Goy, L. Davidovich, and S. Haroche. Realization of a two-photon maser oscillator. *Physical review letters*, 59(17):1899–1902, 1987.

[5] R. J. Thompson, G. Rempe, and H. J. Kimble. Observation of normal-mode splitting for an atom in an optical cavity. *Phys. Rev. Lett.*, 68:1132–1135, 1992.

[6] M. G. Raizen, R. J. Thompson, R. J. Brecha, H. J. Kimble, and H. J. Carmichael. Normal-mode splitting and linewidth averaging for two-state atoms in an optical cavity. *Phys. Rev. Lett.*, 63:240–243, 1989.

[7] A. D. Boozer, A. Boca, R. Miller, T. E. Northup, and H. J. Kimble. Reversible state transfer between light and a single trapped atom. *Physical Review Letters*, 98(19):193601, 2007.

[8] A. Kuhn, M. Hennrich, and G. Rempe. Deterministic single-photon source for distributed quantum networking. *Phys. Rev. Lett.*, 89:067901–067901, 2002.

[9] J. McKeever, A. Boca, A. Boozer, R. Miller, J. Buck, A. Kuzmich, and H. Kimble. Deterministic generation of single photons from one atom trapped in a cavity. *Science*, 303(5666):1992–1994, 2004.

[10] T. Wilk, S. C. Webster, A. Kuhn, and G. Rempe. Single-atom single-photon quantum interface. *Science*, 317(5837):488–490, 2007.

[11] L. You, X. Yi, and X. Su. Quantum logic between atoms inside a high-Q optical cavity. *Physical Review A*, 67(3):32308, 2003.

[12] J. Pachos and H. Walther. Quantum computation with trapped ions in an optical cavity. *Physical review letters*, 89(18):187903, 2002.

[13] B. Tregenna, A. Beige, and P. Knight. Quantum computing in a macroscopic dark period. *Physical Review A*, 65(3):32305, 2002.

[14] M. Khudaverdyan, W. Alt, I. Dotsenko, T. Kampschulte, K. Lenhard, A. Rauschenbeutel, S. Reick, K. Schörner, A. Widera, and D. Meschede. Controlled insertion and retrieval of atoms coupled to a high-finesse optical resonator. *New Journal of Physics*, 10(7):073023 (16pp), 2008.

[15] Y. Colombe, T. Steinmetz, G. Dubois, F. Linke, D. Hunger, and J. Reichel. Strong atom-field coupling for Bose-Einstein condensates in an optical cavity on a chip. *Nature*, 450(7167):272–276, Nov. 2007.

[16] S. Nuszmann, K. Murr, M. Hijlkema, B. Weber, A. Kuhn, and G. Rempe. Vacuum-stimulated cooling of single atoms in three dimensions. *Nat Phys*, 1(2):122–125, Nov. 2005.

[17] A. D. Boozer, A. Boca, R. Miller, T. E. Northup, and H. J. Kimble. Cooling to the ground state of axial motion for one atom strongly coupled to an optical cavity. *Physical Review Letters*, 97(8):083602, Aug. 2006.

[18] W. Hansel, P. Hommelhoff, T. W. Hansch, and J. Reichel. Bose-einstein condensation on a microelectronic chip. *Nature*, 413:498–501, 2001.

[19] H. Ott, J. Fortagh, G. Schlotterbeck, A. Grossmann, and C. Zimmermann. Bose-Einstein condensation in a surface microtrap. *Physical Review Letters*, 87(23):230401, 2001.

[20] T. Schumm. Matter wave interferometry in a double well on an atom chip. *Nature Phys.*, 1:57–62, 2005.

[21] Y. Wang, D. Anderson, V. Bright, E. Cornell, Q. Diot, T. Kishimoto, M. Prentiss, R. Saravanan, S. Segal, and S. Wu. Atom Michelson interferometer on a chip using a Bose-Einstein condensate. *Physical review letters*, 94(9):90405, 2005.

[22] P. Treutlein, P. Hommelhoff, T. Steinmetz, T. W. Hänsch, and J. Reichel. Coherence in microchip traps. *Phys. Rev. Lett.*, 92(20):203005–, May 2004.

[23] P. Treutlein, D. Hunger, S. Camerer, T. W. Hänsch, and J. Reichel. Bose-einstein condensate coupled to a nanomechanical resonator on an atom chip. *Physical Review Letters*, 99(14):140403, 2007.

[24] E. Jaynes and F. Cummings. Comparison of quantum and semiclassical radiation theories with application to the beam maser. *Proc. IEEE*, 51:89–109, 1963.

[25] M. Brune, F. Schmidt-Kaler, A. Maali, J. Dreyer, E. Hagley, J. M. Raimond, and S. Haroche. Quantum rabi oscillation: A direct test of field quantization in a cavity. *Phys. Rev. Lett.*, 76(11):1800–, Mar. 1996.

[26] K. M. Birnbaum, A. Boca, R. Miller, A. D. Boozer, T. E. Northup, and H. J. Kimble. Photon blockade in an optical cavity with one trapped atom. *Nature*, 436(7047):87–90, July 2005.

[27] A. Kubanek, A. Ourjoumtsev, I. Schuster, M. Koch, P. W. H. Pinkse, K. Murr, and G. Rempe. Two-photon gateway in one-atom cavity quantum electrodynamics. *Phys. Rev. Lett.*, 101(20):203602–4, Nov. 2008.

[28] G. Nogues, A. Rauschenbeutel, S. Osnaghi, M. Brune, J. Raimond, and S. Haroche. Seeing a single photon without destroying it. *Nature*, 400(6741):239–242, 1999.

[29] H. Carmichael. *An Open Systems Approach to Quantum Optics*. Springer-Verlag, 1992.

[30] M. J. Collett and C. W. Gardiner. Squeezing of intracavity and traveling-wave light fields produced in parametric amplification. *Phys. Rev. A*, 30(3):1386–1391, Sep 1984.

[31] S. M. Dutra and G. Nienhuis. Derivation of a hamiltonian for photon decay in a cavity. *Journal of Optics B: Quantum and Semiclassical Optics*, 2(5):584–588, 2000.

[32] S. M. Dutra. *Cavity Quantum Electrodynamics: The Strange Theory of Light in a Box*. Wiley, Dec. 2004.

[33] G. Hechenblaikner, M. Gangl, P. Horak, and H. Ritsch. Cooling an atom in a weakly driven high-q cavity. *Phys. Rev. A*, 58(4):3030–, Oct. 1998.

[34] L. Lugiato. Theory of optical bistability. *Progress in optics*, 21:69–216, 1984.

[35] D. A. Steck. Rubidium 87 d line data (rev. 2008).

[36] R. Grimm, M. Weidemuller, and Y. B. Ovchinnikov. Optical dipole traps for neutral atoms. *Adv. At. Mol. Opt. Phys.*, 42:95–170, 2000.

[37] B. Darquié. *Manipulation d' atomes dans des pièges dipolaires microscopiques et émission contrôlée de photons par un atome unique.* PhD thesis, Univ Paris Sud, 2005.

[38] P. Maunz. *Cavity cooling and spectroscopy of a bound atom-cavity system.* PhD thesis, Max Plack Institut fur Quanten Optik, 2005.

[39] J. Dalibard and C. Cohen-Tannoudji. Atomic motion in laser light: connection between semiclassical and quantum descriptions. *J. Phys. B*, 18:1661, 1985.

[40] A. C. Doherty, T. W. Lynn, C. J. Hood, and H. J. Kimble. Trapping of single atoms with single photons in cavity qed. *Phys. Rev. A*, 63(1):013401–, Nov. 2000.

[41] J. P. Gordon and A. Ashkin. Motion of atoms in a radiation trap. *Phys. Rev. A*, 21(5):1606–, May 1980.

[42] A. Boca, R. Miller, K. Birnbaum, A. Boozer, J. McKeever, and H. Kimble. Observation of the vacuum Rabi spectrum for one trapped atom. *Physical review letters*, 93(23):233603, 2004.

[43] K. M. Birnbaum. *Cavity QED with Multilevel Atoms.* PhD thesis, California Institute of Technology, 2005.

[44] T. Steinmetz. *Resonator-Quantenelektrodynamik auf einem Mikrofallenchip.* PhD thesis, Ludwig-Maximilians-Universitat München, 2008.

[45] P. Treutlein, T. W. Hansch, J. Reichel, A. Negretti, M. A. Cirone, and T. Calarco. Microwave potentials and optimal control for robust quantum gates on an atom chip. *Phys. Rev. A*, 74(2):022312–13, Aug. 2006.

[46] P. Treutlein. *Coherent manipulation of ultracold atoms on atom chips.* PhD thesis, LMU, 2008.

[47] J. Reichel, W. HÃd'nsel, P. Hommelhoff, and T. HÃd'nsch. Applications of integrated magnetic microtraps. *Applied Physics B: Lasers and Optics*, 72(1):81–89, Jan. 2001.

[48] J. Reichel. Microchip traps and bose-einstein condensation. *Appl. Phys. B*, 74:469–487, 2002.

[49] D. Hunger. Herstellung und charakterisierung von faserresonatoren hoher finesse. Master's thesis, Ludwig-Maximilians-Universitat Muenchen, 2005.

[50] C. Deutsch. High finesse fibre fabry-perot resonators. Master's thesis, Ludwig-Maximilians Universität München, 2008.

[51] A. Rossi, V. Biancalana, B. Mai, and L. Tomassetti. Long-term drift laser frequency stabilization using purely optical reference. *Review of Scientific Instruments*, 73:2544, 2002.

[52] R. Drever, J. Hall, F. Kowalski, J. Hough, G. Ford, A. Munley, and H. Ward. Laser phase and frequency stabilization using an optical resonator. *Applied Physics B: Lasers and Optics*, 31(2):97–105, 1983.

[53] A. Siegman. *Lasers.* University Science Books, Mill Valley, California, 1986.

[54] E. Saleh and M. Teich. *Fundamentals of Photonics.* Wiley, 1991.

[55] A. Ottl, S. Ritter, M. Kohl, and T. Esslinger. Hybrid apparatus for bose-einstein condensation and cavity quantum electrodynamics: Single atom detection in quantum degenerate gases. *Rev. Sci. Instrum.*, 77:063118–, 2006.

[56] T. W. Lynn. *Measurment and Control of individual Quantia in Cavity QED.* PhD thesis, California Institute of Technology, 2003.

[57] M. A. N. Razvi, X. Z. Chu, R. Alheit, G. Werth, and R. Blümel. Fractional frequency collective parametric resonances of an ion cloud in a paul trap. *Phys. Rev. A*, 58(1):R34–, July 1998.

[58] H. Mabuchi, Q. A. Turchette, M. S. Chapman, and H. J. Kimble. Real-time detection of individual atoms falling through a high-finesse optical cavity. *Opt. Lett.*, 21:1393–1395, 1996.

[59] D. Heine, M. Wilzbach, T. Raub, B. Hessmo, and J. Schmiedmayer. Integrated atom detector: Single atoms and photon statistics. *Phys. Rev. A*, 79(2):021804–4, Feb. 2009.

[60] I. Teper, Y.-J. Lin, and V. Vuletic. Resonator-aided single-atom detection on a microfabricated chip. *Phys. Rev. Lett.*, 97(2):023002–4, July 2006.

[61] A. Ottl, S. Ritter, M. Kohl, and T. Esslinger. Correlations and counting statistics of an atom laser. *Phys. Rev. Lett.*, 95:090404–, 2005.

[62] J. Fortagh, A. Grossmann, C. Zimmermann, and T. H
"ansch. Miniaturized wire trap for neutral atoms. *Physical Review Letters*, 81(24):5310–5313, 1998.

[63] J. Reichel, W. Hansel, and T. W. Hansch. Atomic micromanipulation with magnetic surface traps. *Phys. Rev. Lett.*, 83:3398–3401, 1999.

[64] J. Esteve, C. Aussibal, T. Schumm, C. Figl, D. Mailly, I. Bouchoule, C. Westbrook, and A. Aspect. Role of wire imperfections in micromagnetic traps for atoms. *Physical Review A*, 70(4):43629, 2004.

[65] A. Leanhardt, Y. Shin, A. Chikkatur, D. Kielpinski, W. Ketterle, and D. Pritchard. Bose-Einstein condensates near a microfabricated surface. *Physical review letters*, 90(10):100404, 2003.

[66] J. Fortagh, H. Ott, S. Kraft, A. Günther, and C. Zimmermann. Surface effects in magnetic microtraps. *Physical Review A*, 66(4):41604, 2002.

[67] S. Haroche and J.-M. Raimond. Exploring the quantum: Atoms, cavities and photons, 2006.

[68] J. Ye, D. W. Vernooy, and H. J. Kimble. Trapping of single atoms in cavity qed. *Phys. Rev. Lett.*, 83:4987–4990, 1999.

[69] C. J. Hood, T. W. Lynn, A. C. Doherty, A. S. Parkins, and H. J. Kimble. The atom-cavity microscope: single atoms bound in orbit by single photons. *Science*, 287:1447–1453, 2000.

[70] F. Brennecke, T. Donner, S. Ritter, T. Bourdel, M. Kohl, and T. Esslinger. Cavity qed with a bose-einstein condensate. *Nature*, 450(7167):268–271, Nov. 2007.

[71] M. Greiner, O. Mandel, T. Esslinger, T. W. Hansch, and I. Bloch. Quantum phase transition from a superfluid to a mott insulator in a gas of ultracold atoms. *Nature*, 415(6867):39–44, Jan. 2002.

[72] O. Mandel, M. Greiner, A. Widera, T. Rom, T. W. Hansch, and I. Bloch. Controlled collisions for multi-particle entanglement of optically trapped atoms. *Nature*, 425(6961):937–940, Oct. 2003.

[73] M. Greiner. *Ultracold quantum gases in three-dimensional optical lattice potentials*. PhD thesis, Ludwig-Maximilians-Universität München, 2003.

[74] D. Jaksch, C. Bruder, J. I. Cirac, C. W. Gardiner, and P. Zoller. Cold bosonic atoms in optical lattices. *Phys. Rev. Lett.*, 81:3108–3111, 1998.

[75] Z. Hu and H. J. Kimble. Observation of a single atom in a magneto-optical trap. *Opt. Letters.*, 19:1888, 1994.

[76] D. Frese, B. Ueberholz, S. Kuhr, W. Alt, D. Schrader, V. Gomer, and D. Meschede. Single atoms in an optical dipole trap: towards a deterministic source of cold atoms. *Physical Review Letters*, 85(18):3777–3780, 2000.

[77] N. Schlosser, G. Reymond, I. Protsenko, and P. Grangier. Sub-poissonian loading of single atoms in a microscopic dipole trap. *Nature*, 411(6841):1024–1027, 2001.

[78] D. Harber, J. Obrecht, J. McGuirk, and E. Cornell. Measurement of the Casimir-Polder force through center-of-mass oscillations of a Bose-Einstein condensate. *Physical Review A*, 72(3):33610, 2005.

[79] C. W. Gardiner, J. Ye, H. C. Nagerl, and H. J. Kimble. Evaluation of heating effects on atoms trapped in an optical trap. *Phys. Rev. A*, 61(4):045801–, Mar. 2000.

[80] J. McKeever, J. R. Buck, A. D. Boozer, A. Kuzmich, H.-C. Nägerl, D. M. Stamper-Kurn, and H. J. Kimble. State-insensitive cooling and trapping of single atoms in an optical cavity. *Phys. Rev. Lett.*, 90(13):133602–, Apr. 2003.

[81] T. A. Savard, K. M. O'Hara, and J. E. Thomas. Laser-noise-induced heating in far-off resonance optical traps. *Phys. Rev. A*, 56:R1095–R1098, 1997.

[82] C. Tuchendler, A. M. Lance, A. Browaeys, Y. R. P. Sortais, and P. Grangier. Energy distribution and cooling of a single atom in an optical tweezer. *Phys. Rev. A*, 78(3):033425–9, Sept. 2008.

[83] P. Grangier, J. Levenson, and J. Poizat. Quantum non-demolition measurements in optics. *Nature*, 396(6711):537–542, 1998.

[84] M. Holland, M. Collett, D. Walls, and M. Levenson. Nonideal quantum nondemolition measurements. *Physical Review A*, 42(5):2995–3005, 1990.

[85] W. Nagourney, J. Sandberg, and H. Dehmelt. Shelved optical electron amplifier-Observation of quantum jumps. *Physical Review Letters (ISSN 0031-9007)*, 56, 1986.

[86] T. Sauter, W. Neuhauser, R. Blatt, and P. Toschek. Observation of quantum jumps. *Physical review letters*, 57(14):1696–1698, 1986.

[87] J. Bergquist, R. Hulet, W. Itano, and D. Wineland. Observation of quantum jumps in a single atom. *Physical review letters*, 57(14):1699–1702, 1986.

[88] P. Grangier, J. Roch, and G. Roger. Observation of backaction-evading measurement of an optical intensity in a three-level atomic nonlinear system. *Physical review letters*, 66(11):1418–1421, 1991.

[89] J. Roch, K. Vigneron, P. Grelu, A. Sinatra, J. Poizat, and P. Grangier. Quantum nondemolition measurements using cold trapped atoms. *Physical Review Letters*, 78(4):634–637, 1997.

[90] S. Gleyzes, S. Kuhr, C. Guerlin, J. Bernu, S. Deleglise, U. Busk Hoff, M. Brune, J.-M. Raimond, and S. Haroche. Quantum jumps of light recording the birth and death of a photon in a cavity. *Nature*, 446(7133):297–300, Mar. 2007.

[91] J. Berezovsky, M. Mikkelsen, O. Gywat, N. Stoltz, L. Coldren, and D. Awschalom. Nondestructive optical measurements of a single electron spin in a quantum dot. *Science*, 314(5807):1916, 2006.

[92] A. Lupaşcu, C. Verwijs, R. Schouten, C. Harmans, and J. Mooij. Nondestructive readout for a superconducting flux qubit. *Physical review letters*, 93(17):177006, 2004.

[93] A. Lupaşcu, E. Driessen, L. Roschier, C. Harmans, and J. Mooij. High-contrast dispersive readout of a superconducting flux qubit using a nonlinear resonator. *Physical review letters*, 96(12):127003, 2006.

[94] C. Guerlin, J. Bernu, S. Deleglise, C. Sayrin, S. Gleyzes, S. Kuhr, M. Brune, J.-M. Raimond, and S. Haroche. Progressive field-state collapse and quantum non-demolition photon counting. *Nature*, 448(7156):889–893, Aug. 2007.

[95] S. Deleglise, I. Dotsenko, C. Sayrin, J. Bernu, M. Brune, J.-M. Raimond, and S. Haroche. Reconstruction of non-classical cavity field states with snapshots of their decoherence. *Nature*, 455(7212):510–514, Sept. 2008.

[96] A. Kuzmich, L. Mandel, and N. P. Bigelow. Generation of spin squeezing via continuous quantum nondemolition measurement. *Phys. Rev. Lett.*, 85:1594–1597, 2000.

[97] A. Dantan, J. Cviklinski, E. Giacobino, and M. Pinard. Spin squeezing and light entanglement in coherent population trapping. *Physical review letters*, 97(2):23605, 2006.

[98] J. Geremia, J. K. Stockton, and H. Mabuchi. Real-time quantum feedback control of atomic spin-squeezing. *Science*, 304(5668):270–273, Apr. 2004.

[99] I. Dotsenko, M. Mirrahimi, M. Brune, S. Haroche, J. Raimond, and P. Rouchon. Quantum feedback by discrete quantum non-demolition measurements: towards on-demand generation of photon-number states. Arxiv preprint arXiv:0905.0114, 2009.

[100] Aristotle. *Physics*. Available online at http://classics.mit.edu/Aristotle/physics.html (Translated by R. P. Hardie and R. K. Gaye).

[101] B. Misra and E. C. G. Sudarshan. The zeno's paradox in quantum theory. *Journal of Mathematical Physics*, 18(4):756–763, 1977.

[102] W. M. Itano, D. J. Heinzen, J. J. Bollinger, and D. J. Wineland. Quantum zeno effect. *Phys. Rev. A*, 41(5):2295–, Mar. 1990.

[103] W. M. Itano, D. J. Heinzen, J. J. Bollinger, and D. J. Wineland. Reply to "comment on 'quantum zeno effect"'. *Phys. Rev. A*, 43(9):5168–, May 1991.

[104] L. E. Ballentine. Comment on "quantum zeno effect". *Phys. Rev. A*, 43(9):5165–, May 1991.

[105] A. Peres and A. Ron. Incomplete "collapse" and partial quantum zeno effect. *Phys. Rev. A*, 42(9):5720–, Nov. 1990.

[106] C. Balzer, R. Huesmann, W. Neuhauser, and P. E. Toschek. The quantum zeno effect - evolution of an atom impeded by measurement. *Optics Communications*, 180:115, 2000.

[107] K. Mølhave and M. Drewsen. Demonstration of the continuous quantum zeno effect in optical pumping. *Physics Letters A*, 268(1-2):45–49, Apr. 2000.

[108] T. Nakanishi, K. Yamane, and M. Kitano. Absorption-free optical control of spin systems: The quantum zeno effect in optical pumping. *Phys. Rev. A*, 65(1):013404–, Dec. 2001.

[109] J. Bernu, S. Deléglise, C. Sayrin, S. Kuhr, I. Dotsenko, M. Brune, J. M. Raimond, and S. Haroche. Freezing coherent field growth in a cavity by the quantum zeno effect. *Phys. Rev. Lett.*, 101:180402, 2008.

[110] E. W. Streed, J. Mun, M. Boyd, G. K. Campbell, P. Medley, W. Ketterle, and D. E. Pritchard. Continuous and pulsed quantum zeno effect. *Phys. Rev. Lett.*, 97:260402, 2006.

[111] M. C. Fischer, B. Gutiérrez-Medina, and M. G. Raizen. Observation of the quantum zeno and anti-zeno effects in an unstable system. *Phys. Rev. Lett.*, 87(4):040402–, July 2001.

[112] A. Beige, D. Braun, B. Tregenna, and P. Knight. Quantum computing using dissipation to remain in a decoherence-free subspace. *Physical Review Letters*, 85(8):1762–1765, 2000.

[113] P. G. Kwiat, A. G. White, J. R. Mitchell, O. Nairz, G. Weihs, H. Weinfurter, and A. Zeilinger. High-efficiency quantum interrogation measurements via the quantum zeno effect. *Phys. Rev. Lett.*, 83:4725–4728, 1999.

[114] O. Hosten, M. T. Rakher, J. T. Barreiro, N. A. Peters, and P. G. Kwiat. Counterfactual quantum computation through quantum interrogation. *Nature*, 439:949–952, 2006.

[115] P. Facchi, S. Tasaki, S. Pascazio, H. Nakazato, A. Tokuse, and D. Lidar. Control of decoherence: Analysis and comparison of three different strategies. *Physical Review A*, 71(2):22302, 2005.

[116] S. Maniscalco, F. Francica, R. L. Zaffino, N. L. Gullo, and F. Plastina. Protecting entanglement via the quantum zeno effect. *Physical Review Letters*, 100(9):090503, 2008.

[117] P. Facchi, V. Gorini, G. Marmo, S. Pascazio, and E. C. G. Sudarshan. Quantum zeno dynamics. *Physics Letters A*, 275:12–19, Oct. 2000.

[118] P. Facchi and S. Pascazio. Quantum zeno subspaces. *Phys. Rev. Lett.*, 89(8):080401, Aug 2002.

[119] J. Cirac. Interaction of a two-level atom with a cavity mode in the bad-cavity limit. *Physical Review A*, 46(7):4354–4362, 1992.

[120] P. Facchi and S. Pascazio. Quantum zeno dynamics: mathematical and physical aspects. *Journal of Physics A: Mathematical and Theoretical*, 41(49):493001 (45pp), 2008.

[121] A. Gaetan, Y. Miroshnychenko, T. Wilk, A. Chotia, M. Viteau, D. Comparat, P. Pillet, A. Browaeys, and P. Grangier. Observation of collective excitation of two individual atoms in the rydberg blockade regime. *Nat Phys*, 5(2):115–118, Feb. 2009.

[122] T. Wilk, A. Gaetan, C. Evellin, J. Wolters, Y. Miroshnychenko, P. Grangier, and A. Browaeys. Entanglement of two individual neutral atoms using rydberg blockade. arXiv:0908.0454v1, 2009.

[123] R. H. Dicke. Coherence in spontaneous radiation processes. *Phys. Rev.*, 93:99–110, 1954.

[124] H. Carmichael and K. Kim. A quantum trajectory unraveling of the superradiance master equation. *Optics Communications*, 179(1-6):417–427, 2000.

[125] C. F. Roos, G. P. T. Lancaster, M. Riebe, H. Häffner, W. Hänsel, S. Gulde, C. Becher, J. Eschner, F. Schmidt-Kaler, and R. Blatt. Bell states of atoms with ultralong lifetimes and their tomographic state analysis. *Phys. Rev. Lett.*, 92(22):220402, Jun 2004.